

# **For Reference**

---

**NOT TO BE TAKEN FROM THIS ROOM**



Ex LIBRIS  
UNIVERSITATIS  
ALBERTAENSIS





Digitized by the Internet Archive  
in 2023 with funding from  
University of Alberta Library

<https://archive.org/details/Beltaos1972>







THE UNIVERSITY OF ALBERTA

NORMAL IMPINGEMENT OF PLANE TURBULENT JETS ON SMOOTH WALLS

by



SPYRIDON BELTAOS

A THESIS

SUBMITTED TO THE FACULTY OF GRADUATE STUDIES AND RESEARCH  
IN PARTIAL FULFILMENT OF THE REQUIREMENTS FOR THE DEGREE  
OF MASTER OF SCIENCE

DEPARTMENT OF CIVIL ENGINEERING

EDMONTON, ALBERTA

SPRING, 1972







UNIVERSITY OF ALBERTA  
FACULTY OF GRADUATE STUDIES

The undersigned certify that they have read, and recommend to the Faculty of Graduate Studies for acceptance, a thesis entitled NORMAL IMPINGEMENT OF PLANE TURBULENT JETS ON SMOOTH WALLS submitted by SPYRIDON BELTAOS in partial fulfilment of the requirements for the degree of Master of Science.



## ABSTRACT

The normal impingement of plane turbulent jets on smooth walls is studied experimentally and analytically. Three distinct flow regions exist in this phenomenon; the free jet region, the impingement region and the wall jet region. The free jet region exhibits properties almost identical to those of a free jet. Its extent is shown to be a fixed portion of the impingement height. The impingement region is characterized by increased static pressure and continuous deflection of the velocity vector. The velocity and pressure fields in this region are studied by means of a Pitot cylinder. A measuring technique, not involving rotation and separate pressure measurement, is developed. Analytical expressions are developed for the variation of axial velocity and pressure as well as for the maximum velocity along the wall and the wall shear stress. The flow in the wall jet region approximates that of the classical wall jet. The length scale varies linearly with distance. The local skin friction coefficient is shown to be a constant, whereas the velocity scale is shown to vary as a power of distance, the exponent being less than  $-0.5$ . Generally, the dimensionless height of impingement has little significance, while the nozzle Reynolds number is a relevant parameter.





## ACKNOWLEDGEMENTS

The author is grateful to:

- Dr. N. Rajaratnam for his valuable guidance and supervision of this thesis.
- The staff of the Hydraulics Laboratory for their help in various phases of the work.
- The National Research Council of Canada for the support of this work through a grant to Dr. N. Rajaratnam (A-3365).





# TABLE OF CONTENTS

	<u>Page</u>
CHAPTER I INTRODUCTION	1
CHAPTER II EXPERIMENTS	4
2.1 Experimental Set-Up	4
2.2 Experimental Techniques	5
2.2.1 Nozzle Velocity	5
2.2.2 Velocity and Pressure Measurements in Impingement Region. Pitot Cylinder	6
2.2.3 Wall Shear Measurements	12
2.3 Experimental Results	14
2.3.1 Free Jet and Impingement Regions	16
2.3.2 Wall Jet Region	21
CHAPTER III ANALYSIS	53
3.1 Physical Considerations	53
3.2 Dimensional Analysis	55
3.2.1 Free Jet and Impingement Regions	55
3.2.2 Wall Jet Region	63
3.3 Theoretical Development	66
3.3.1 Free Jet Region	66
3.3.2 Impingement Region	67
3.3.3 Wall Jet Region	79
CHAPTER IV SUMMARY AND CONCLUSIONS	106
REFERENCES	111
APPENDIX A DATA TABLES	A-1



## LIST OF TABLES

<u>Table</u>		<u>Page</u>
I	Range of Experiments	15
II	Exponent $a$	86
A-I	Length Scales - Run No. 1	A-1
A-II	Axial Velocity and Pressure	A-2
A-III	Wall Pressure Distribution	A-3
A-IV	Shear Stress and Maximum Velocity in Impingement Region	A-6
A-V	Maximum Velocity, Length Scale and Shear Stress in Wall Jet Region	A-7





## LIST OF FIGURES

<u>Figure</u>		<u>Page</u>
1.1	Sketch of Flow Regions	2
2.1	Experimental Set-Up	25
2.2	Nozzle and Chamber Details	25
2.3	Application of Bernoulli Theorem	5
2.4	The Pitot Cylinder	7
2.5	Pitot Cylinder Calibration Factors	26
2.6	Calibration Factor $K$	27
2.7	Calibration Factors $K_1$ - $K_2$ and $K_3$ - $K_2$	28
2.8	Generalized Factors $K_1$ , $K_2$ , $K_3$	29
2.9	Generalized Factor $K$	30
2.10	Generalized Factors $K_1$ - $K_2$ and $K_3$ - $K_2$	31
2.11	Slot Details	32
2.12	Static Tap Spacing	32
2.13	Patel Equations for Smooth Walls	33
2.14	Chart to Correct Flattened Tube Readings	34
2.15	Definition Sketch	35
2.16	Velocity Profiles in Free Jet and Impingement Regions	36
2.17	Dimensionless Velocity Distribution in Free Jet and Impingement Regions	37
2.18	Distribution of $v$ Component in Impingement Region	38
2.19	Typical $u_{m1}$ Variation in Impingement Region	39
2.20	Distribution of the Product $uv$ in Impingement Region	40
2.21	Excess Static Pressure in Impingement Region	41
2.22	Dimensionless Pressure Distribution in Impingement Region	42
2.23	Typical Wall Pressure Distribution	43





## LIST OF FIGURES (Cont'd)

<u>Figure</u>		<u>Page</u>
2.24	Decay of Axial Velocity in Free Jet and Impingement Regions	44
2.25	Axial Pressure in Free Jet and Impingement Regions	45
2.26	Length Scale for Velocity in Free Jet and Impingement Regions	46
2.27	Length Scale for Pressure in Impingement Region	47
2.28	Shear Velocity Distribution in Impingement Region	48
2.29	Typical Velocity Profiles in Wall Jet	49
2.30	Dimensionless Velocity Distribution in Wall Jet	50
2.31	Sketch of "True" Velocity Profile	22
2.32	Maximum Velocity Decay in Wall Jet	51
2.33	Length Scale Variation in Wall Jet	52
3.1	Sketch of Function $h(\frac{x}{H})$	57
3.2	Axial Velocity in Free Jet and Impingement Regions	89
3.3	Axial Pressure in Free Jet and Impingement Regions	90
3.4	Universal Wall Pressure Distribution	91
3.5	Length Scale for Velocity in Free Jet and Impingement Regions	92
3.6	Length Scale for Pressure in Impingement Region	93
3.7	Maximum Horizontal Velocity in Impingement Region	94
3.8	Shear Velocity in Impingement Region	95
3.9	Sketch of Momentum Balance	63
3.10	Comparison of Eqn 3.21 With Experimental Results	96
3.11	Evaluation of Constants in Eqn 3.26	97
3.12	Total Axial Pressure in Impingement Region	98
3.13	Generalized Outline of Impinging Jet	99
3.14	Variation of $\frac{u}{u_{m1}}$ in Wall Jet	100
3.15	Variation of $C_f$ With $R_o$	101
3.16	Evaluation of C in Eqn 3.53	102
3.17	Evaluation of C in Eqn 3.53	103



## LIST OF FIGURES (Cont'd)

<u>Figure</u>		<u>Page</u>
3.18	Evaluation of C in Eqn 3.53	104
3.19	Variation of C With $\frac{H}{2b_o}$	105





## LIST OF SYMBOLS

SYMBOL	QUANTITY
$a$	exponent
$b_o$	half width of nozzle
$b_p$	length scale for pressure
$b_{pw}$	value of $b_p$ at the wall
$b_u$	length scale for velocity
$b_l$	length scale in wall jet
$\bar{b}_u$	value of $y$ at which $u=0$
$\bar{b}_l$	value of $y_l$ at which $u_l=0$
$C$	constant
$C_f$	local skin friction coefficient
$d$	tube diameter, tube height
$e$	basis of natural logarithms
$f$	function
$F$	function, constant
$g$	function
$G$	function
$h$	function
$H$	impingement height
$I_p$	probability integral
$k$	constant
$K$	constant, calibration factor
$K_1, K_2, K_3$	calibration factors
$M$	momentum
$n$	contour value



## LIST OF SYMBOLS (Cont'd)

SYMBOL	QUANTITY
$p$	pressure, excess static pressure
$p_m$	axial pressure
$p_s$	stagnation pressure
$p_T$	total axial pressure
$p_w$	wall pressure
$\Delta p$	pressure difference
$R$	Reynolds number
$u$	time average of velocity in $x$ direction
$u_1$	time average of velocity in $x_1$ direction
$u_m$	cross sectional maximum of $u$
$u_{m1}$	cross sectional maximum of $u_1$
$u'_1$	fluctuating component of velocity in $x_1$ direction
$u_*$	shear velocity
$U_o$	velocity at nozzle exit
$v$	time average of velocity in $y$ direction
$v_1$	time average of velocity in $y_1$ direction
$v'_1$	fluctuating component of velocity in $y_1$ direction
$v_e$	entrainment velocity
$V$	total velocity
$x$	longitudinal distance from nozzle
$x_1$	distance along the wall from stagnation point
$y$	distance from axis of jet
$y_1$	distance from wall
$z$	dummy variable of integration





## LIST OF SYMBOLS (Cont'd)

SYMBOL	QUANTITY
--------	----------

## GREEK LETTERS

$\alpha$	denotes proportionality
$\beta$	angle
$\delta$	boundary layer thickness
$\Delta$	difference, pressure gradient parameter
$\eta$	similarity variable
$\nu$	kinematic viscosity
$\xi$	similarity variable
$\pi$	the constant pi
$\rho$	mass density
$\tau$	shear stress
$\tau_0$	wall shear stress
$\phi$	angle
$\psi$	function

Other symbols are defined where they appear.



## CHAPTER I

### INTRODUCTION

The impingement of a turbulent jet on a solid surface finds application in a number of engineering problems. Jets issuing from hydraulic outlet works, weirs, vertical take-off aircraft and various spraying devices are examples of such problems.

The very general case of the impingement problem is a jet issuing from an outlet of any shape and impinging on a solid surface of any shape and texture. However, plane and circular jets impinging on plane surfaces may be recognized to be, by far, of more practical importance. Furthermore, since the plane jet impingement constitutes the simplest case of this problem, it is obvious that its study should be of importance in understanding more complicated situations.

This thesis is an attempt to study both experimentally and analytically, the case of a plane turbulent submerged jet impinging normally on a smooth and flat boundary. In this case, the flow issuing from a two-dimensional nozzle strikes a flat, smooth surface as shown in Fig. 1.1. After impingement, the jet changes direction and flows along the boundary.

In general, we may recognize three distinct regions of flow with reference to its pattern [1], [2], [3]. In region I, the flow characteristics are, for all practical purposes, identical to those of



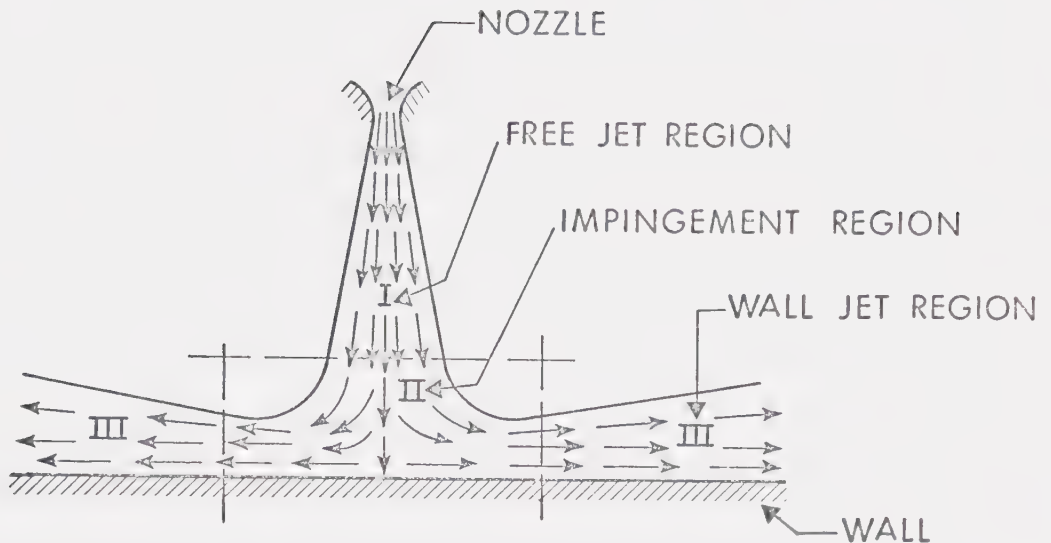


FIG. I.1 SKETCH OF FLOW REGIONS

a free jet [1], [2], [3], [4]. This region therefore is referred to as the "free jet region". In region II, the flow undergoes deflection and at the end of the region becomes parallel to the wall (region III), assuming a pattern very similar to what is known as the wall jet. It is appropriate therefore to refer to region II as the "impingement region" and to region III as the "wall jet region". It is logical to expect transitions between these regions. This aspect will be discussed in later chapters.

The main objective for region I was to determine its extent. In region II, where the static pressure is generally higher than the hydrostatic value and the velocity vector assumes a relatively large angle with the initial jet direction, the main objective was to study





the velocity and pressure fields. The wall shear stress was also studied. In the wall jet region the objectives were to investigate the velocity field, the jet thickness and the distribution of the wall shear stress.

A number of investigations regarding impinging jets have been carried out already and some experimental results as well as analytical procedures are available, [1], [2], [3], [4], [5]. These are mostly connected with circular jets and include extended studies of the free jet and wall jet regions as well as some measurements of the axial velocity in the impingement region [2]. For the plane case, Mathieu [5] reported measurements for impingement at small angles. His work is mainly concerned with the wall jet forming after impingement. Also for the plane case, Schauer and Eustis [1] reported results for different angles of impingement including the case of normal impingement. Their work is also concerned mainly with the wall jet region. The wall pressure and the maximum velocity, in the impingement region, along the wall were measured.

The present investigation purports to provide detailed results for the impingement region where very little is known and to enlarge the scope of results already available in the wall jet and free jet regions.



## CHAPTER II

### EXPERIMENTS

#### 2.1 Experimental Set-Up

The experiments were conducted in the arrangement shown in Figs. 2.1 and 2.2 using air as the flow medium.

The air was supplied by a compressor connected to a rectangular plenum chamber which terminated in a nozzle smoothly tapered to an exit width of 0.088 in. (Fig. 2.2). The aspect ratio was about 65 so that a plane jet could be produced.

In the chamber, a series of circular tubes was placed near the entrance and a sequence of five screens was placed further downstream, as shown in Fig. 2.2. The tubes served the purpose of "straightening" the flow streamlines which tended to become curvilinear because of the sudden expansion at the entrance. The screens were placed in order to produce complete mixing of the flow before it entered the nozzle section of the chamber. The intensity of the flow was adjusted with the aid of a pressure regulatory valve. The velocity at the nozzle exit was varied between 115 and 207 fps. In this range, compressibility effects are known to be negligible.

To produce impingement, a 1/4 in. thick plexiglass plate, 6 in. wide and 5.75 ft. long was placed normal to the axial plane of the jet. One foot high sidewalls were used to avoid spilling. The





sidewalls were also made of 1/4 in. thick plexiglass and were of the same length as the plate (Fig. 2.1). The impingement height, i.e. the distance between the plate and the exit of the nozzle, was adjusted by raising or lowering the chamber and was varied between 0.103 and 0.495 ft.

## 2.2 Experimental Techniques

### 2.2.1 Nozzle Velocity

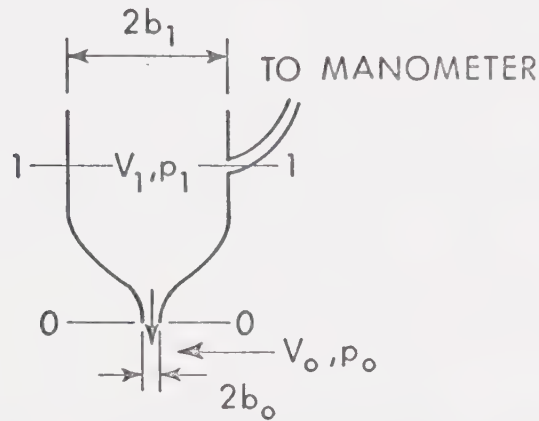


FIG. 2.3 APPLICATION OF BERNOULLI THEOREM

Referring to Fig. 2.3, the Bernoulli theorem applied between section 0-0 and 1-1 gives:

$$p_1 + \frac{\rho U_1^2}{2} = p_0 + \frac{\rho U_0^2}{2} \quad (2.1)$$

where  $\rho$  is the mass density of the fluid,  $p_1$ ,  $U_1$  and  $p_0$ ,  $U_0$  are the static pressure and velocity at the sections 1-1 and 0-0



respectively. By continuity;  $U_1 \cdot 2b_1 = U_o \cdot 2b_o$  or,  $\frac{U_1}{U_o} = \frac{2b_o}{2b_1}$  and

$$\left(\frac{U_1}{U_o}\right)^2 = \left(\frac{2b_o}{2b_1}\right)^2 < < 1. \quad \text{Eq. 1 may therefore be written;}$$

$$\frac{\rho U_o^2}{2} \cong p_1 - p_o = \Delta p_1 \quad (2.2)$$

The validity of Eq. 2.2 was checked by comparing manometer heights with nozzle velocity heads at different velocities  $U_o$ . No difference was recorded between corresponding readings. Since the manometer was vertical and contained water, the minimum reading would be about 3 in. Assuming that reading errors were at most  $\pm 0.05$  in., the maximum head recording error would be about 1.6%. Since  $U_o \propto \sqrt{\Delta p_1}$ , the maximum error in obtaining  $U_o$  values would be less than 1%.

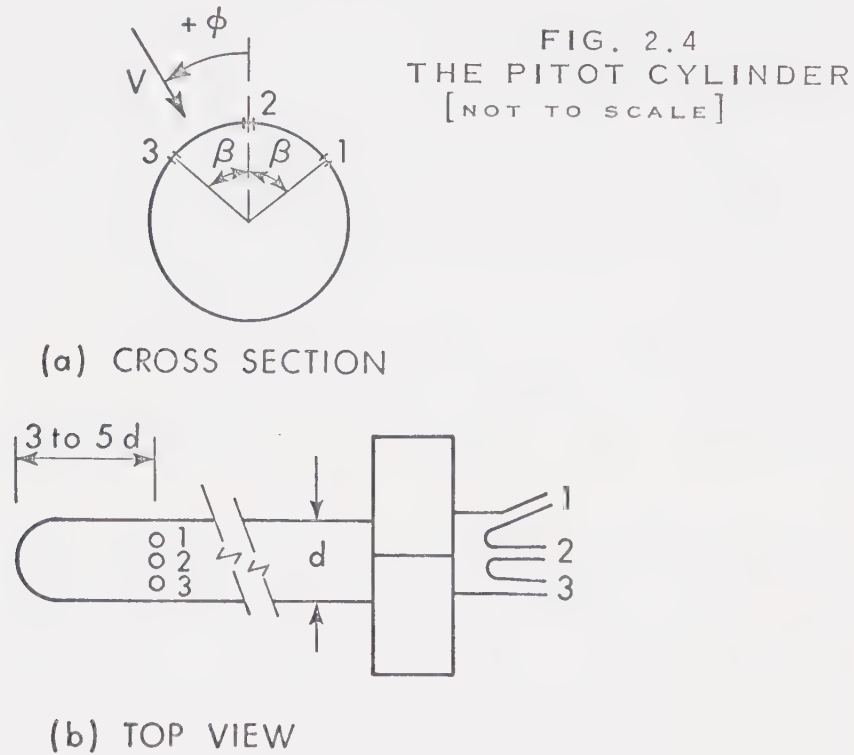
Thus, the nozzle velocity,  $U_o$ , was measured indirectly by recording the pressure  $\Delta p_1$ . This procedure has the advantage that  $U_o$  may be recorded within seconds at any instant, so that corrections for small supply fluctuations can be applied. Manometer heights were converted to pressure and velocity assuming a temperature of 20°C and an atmospheric pressure of 14.7 psi.

### 2.2.2 Velocity and Pressure Measurements in the Impingement Region. Pitot Cylinder.

In the impingement region the direction of the velocity vector is not known before hand. In addition, the static pressure is higher



than the hydrostatic. Therefore, use of ordinary velocity measuring devices was ruled out. After a search of relevant literature [6], [7], [8], [9], it was decided that a Pitot-cylinder be used.



The Pitot cylinder is a cylindrical instrument of small diameter having three orifices (see Fig. 2.4) near its edge which is rounded. When the instrument is placed in any flow and the orifices are connected to a manometer, three readings will be obtained. The values of these readings will depend upon the velocity,  $V$ , the static pressure,  $p_o$ , and the direction of the velocity vector with respect to the axis of the cylinder. When the flow is two-dimensional the instrument may be placed perpendicular to the plane of the flow. Then, the direction of the velocity vector will be fully described by the



angle  $\phi$ , as shown in Fig. 2.4. The ordinary procedure is to rotate the instrument until readings 1 and 3 become equal. Then, reading 2 represents the total head and the direction of  $V$  is indicated. If the static pressure at the point is known, the velocity may be calculated. To avoid rotation of the instrument and separate pressure measurement, an alternative procedure was developed, as follows; if  $p_1, p_2, p_3$  are the pressures recorded for each of the orifices 1, 2, 3 respectively, we may in general write:

$$p_i = p_o + K_i \frac{\rho V^2}{2}, \quad (i = 1, 2, 3) \quad (2.3)$$

where  $\rho$  is the mass density of the fluid and  $K_i$  are three calibration factors. Ordinarily, these factors will depend upon the value of  $\phi$  and the tube Reynolds number,  $R_T = Vd/\nu$  ( $\nu$  is the kinematic viscosity). However, from what is known about pressure distribution around circular cylinders [10], [11], dependence of  $K_i$  on  $R_T$  should be negligible for not excessively large values of  $\phi$ . Thus, it is assumed that:

$$K_i = f_i(\phi), \quad (i = 1, 2, 3) \quad (2.4)$$

From Eqs. 2.3 we obtain:

$$K_i = \frac{p_i - p_o}{\rho V^2 / 2} = \frac{h_i - h_o}{h_u}, \quad (i = 1, 2, 3) \quad (2.5)$$





where  $h_i$ ,  $h_o$  and  $h_u$  are corresponding piezometric heads. Using Eqs. 2.3 it is easy to show that

$$\frac{p_1 - p_2}{p_3 - p_2} = \frac{h_1 - h_2}{h_3 - h_2} = \frac{K_1 - K_2}{K_3 - K_2} \quad (2.6)$$

Setting  $K = \frac{K_1 - K_2}{K_3 - K_2}$ , we deduce from (2.4):

$$K = f_4(\phi) \quad (2.7)$$

If the functions  $f_i$  ( $i = 1, 2, 3$ ) and  $f_4$  are evaluated, then the value of  $\phi$  may be found from Eq. 2.7 by measuring  $h_1, h_2, h_3$  and forming the ratio  $\frac{h_1 - h_2}{h_3 - h_2}$ . Knowing  $\phi$ , the values of  $K_1, K_2, K_3$  may be determined from (2.4). The values of  $V$  and  $p_o$  may be calculated from the following equations:

$$\frac{\rho V^2}{2} = \frac{p_j - p_2}{K_j - K_2}, \quad (j = 1, 3) \quad (2.8)$$

$$p_o = p_i - K_i \frac{\rho V^2}{2}, \quad (i = 1, 2, 3) \quad (2.9)$$

or the equivalent:

$$h_u = \frac{h_j - h_2}{K_j - K_2}, \quad (j = 1, 3) \quad (2.8A)$$



$$h_o = h_i - K_i h_u, (i = 1,2,3) \quad (2.9A)$$

The above equations may easily be derived from Eqs. 2.3. To evaluate the functions  $f_i (i = 1,2,3)$  the following procedure was employed. A Pitot cylinder 1/8 in. in diameter with orifices located at 1/2 in. from the edge, was calibrated in the wind tunnel of the Hydraulics Laboratory for three different values of  $R_T$ . The angle between successive orifices was  $45^\circ$ . The velocity and the static pressure were held constant in each run, while the instrument was rotated by incremental angles and the piezometric heads,  $h_i$ , were recorded each time.

The values of  $K_i$  were computed as indicated in Eqs. 2.5, and are plotted against  $\phi$  in Fig. 2.5. This figure indicates that for the present range of  $R_T$  values (1430 to 5500), any dependence of  $K_i$  on  $R_T$  is indeed negligible. The present results can be extended to larger or smaller values of  $R_T$ , when using geometrically similar instruments, for values of  $\phi$  so that  $|\phi| \leq 30^\circ$ . This restriction is imposed to ensure that none of the orifices will be located in the wake zone where the Reynolds number has significant effect on the pressure distribution. A lower limit for  $R_T$  could be taken as 300, since above this value the wake is fully turbulent. An upper limit for  $R_T$  is obviously the critical value, about  $3 \times 10^5$ , however, it is doubtful that values greater than 50 to 60 thousand will be encountered in practice.



The curves of Fig. 2.5 are almost symmetrical about the axis  $\phi = 0^\circ$ . Deviations from symmetry are believed to be due to imperfections in manufacturing. The calibration factor  $K$  was computed from the above curves and is plotted against  $\phi$  in Fig. 2.6. Figure 2.7 shows the variation of the factors  $K_1 - K_2$  and  $K_3 - K_2$  which appear in Eqs. 2.8 and 2.8A.

For the present study the charts of Figs. 2.5, 2.6 and 2.7 were used for better accuracy, since the tube which was used for calibration purposes was also used for subsequent measurements. Use of the present technique may be done in conjunction with Figs. 2.8 to 2.10, where symmetry is taken into account and generalized curves are drawn.

Equations 2.8 were found to agree very closely. It is recommended that both are used and an average value of  $h_u$  be adopted. In cases where one of the factors  $K_1 - K_2$  and  $K_3 - K_2$  has a very small absolute value, only the equation involving the other factor should be used. Regarding Eqs. 2.9, it is recommended that the one involving the highest absolute value of  $K_i$  be used for better accuracy. The equation involving the next higher value of  $K_i$  may also be used as a check.

The technique described above was based on the same line of thought as that adopted by Rajaratnam and Muralidhar [9] for calibrating yaw and pitch probes, and was mainly developed for measurements in the impingement region. It was also used for measurements in the free jet region where the velocity field is well known.





Measurements in this region could be compared against available data as a means of checking out this technique. No correction for turbulence was applied.

So as to be able to insert the cylinder in the flow, slots were opened on the sidewalls of the flume as shown in Fig. 2.11. Roughness effects of the slots were overcome by taping the slots. The measurements were made in the neighborhood of the centerline of the flume.

To measure the pressure distribution on the wall, 1/16 in. diameter, static taps, located as shown in Fig. 2.12, were connected to a precision manometer. Each distribution was measured two or three times because of the violent fluctuations of the pressure heads.

Measurements of maximum horizontal velocities at the edge of the boundary layer were made with the aid of a total head tube. The static pressure was assumed to be equal to the wall pressure at the same vertical. The tube had a rectangular opening with a height of 0.67 mm and a width of 3.7 mm. This tube was also used for measuring velocities in the wall jet where the static pressure was assumed to be atmospheric.

### 2.2.3 Wall Shear Measurements

Preston's technique [12] was employed to measure wall shear stress with the aid of the calibration curves given by Patel [13] for smooth boundaries and zero pressure gradient flows. This technique is briefly discussed below.



For a Preston tube of external diameter  $d$  resting on a smooth boundary, if  $\Delta p$  is the difference between the total pressure indicated by the tube and the static pressure on the boundary, it could be shown that:

$$\frac{\Delta p d^2}{4\rho\nu^2} = F\left(\frac{\tau_o d^2}{4\rho\nu^2}\right) \quad (2.10)$$

where  $\rho$ ,  $\nu$  are respectively the mass density and kinematic viscosity of the fluid,  $\tau_o$  is the boundary shear stress and  $F$  denotes a functional relation. If we set  $\Delta p d^2/4\rho\nu^2 = \Delta p_*$  and  $\tau_o d^2/4\rho\nu^2 = \tau_{o*}$ , we may write:

$$\Delta p_* = F(\tau_{o*}) \quad (2.11)$$

Using the equations given by Patel for different ranges of the variables,  $\Delta p_*$  and  $\tau_{o*}$ , Eq. 2.11 is plotted in Fig. 2.13.

Ordinarily, this method is applicable when tubes of circular cross-sections are used. However, subsequent investigations [14], [15] have shown that flattened tubes can also be used if the dimensionless groups,  $\Delta p_*$ ,  $\tau_{o*}$ , are formed using the total height of the tube for the external diameter. Since a flattened tube was used to measure horizontal velocities, it was decided that the reading, when the tube rested on the wall, be used for computing shear stress. To control this procedure, wall shear was also measured by means of a circular



tube at several stations. This tube had an external diameter of 1.28 mm and a ratio of internal to external diameter of 0.65. The shear velocities obtained thus were plotted against each other as shown in Fig. 2.14. This figure was used to convert shear velocity values obtained by the flattened tube into values that would be obtained by the circular tube. The difference between corresponding values is generally small.

In the impingement region the pressure gradient is appreciable causing therefore some uncertainty regarding shear measurements. Shear stress was measured by the above technique and subsequently Patel's criteria regarding reliability of the results were applied, as discussed in Chapter III.

### 2.3 Experimental Results

Measurements were conducted for different nozzle velocities and different impingement heights. The nozzle width remained constant throughout the experiments.

Table I shows the combinations of impingement heights and nozzle velocities used, as well as the type of measurements performed in each case. The symbols appearing in this table are explained in the definition sketch, Fig. 2.15, as well as in the "List of Symbols". Referring to Fig. 2.15, in order to retain conventional notations for the co-ordinate systems and the quantities involved, two different systems are used. The system  $x, y$  refers to the free jet and the impingement regions excluding the wall boundary layer, whereas the



TABLE I. RANGE OF EXPERIMENTS

RUN NO.	$\frac{H}{\text{feet}}$	$2b_o$ feet	$U_o$ fps	$\frac{H}{2b_o}$	$R_o^*$	QUANTITIES MEASURED	
						FREE JET AND IMPINGEMENT REGIONS	WALL JET REGION
1	.495	.00733	123.5	67.5	5650	$u, u_m, p, p_m, v, b, b_u, p, p_w, p_s$	—
2	.485	.00733	155.0	66.15	7100	$u_{m1}, \tau_o$	$u_1, u_{m1}, b_1, \tau_o$
3	.485	.00733	124.0	66.15	5680	$p_w, p_s, u_{m1}, \tau_o$	$u_1, u_{m1}, b_1, \tau_o$
4	.320	.00733	205.0	43.6	9400	$p_w, p_s, u_{m1}, \tau_o$	$u_1, u_{m1}, b_1, \tau_o$
5	.320	.00733	155.0	43.6	7100	$u_m, p_m, p_w, p_s, u_{m1}, \tau_o$	$u_1, u_{m1}, b_1, \tau_o$
6	.320	.00733	115.0	43.6	5270	$u_m, p_m, p_w, p_s, u_{m1}, \tau_o$	—
7	.227	.00733	152.0	31.0	6970	$u_m, p_m, p_w, p_s$	—
8	.103	.00733	115.0	14.04	5270	$u_m, p_m, p_w, p_s$	—

$$* R_o = \frac{2U_o b_o}{\nu}$$





system  $x_1, y_1$  refers to the wall jet region, including the boundary layer in the impingement region. Thus,  $x, x_1$  and  $y, y_1$  always denote longitudinal and transverse distances respectively, while the letters  $u$  and  $v$  always denote longitudinal and transverse velocity components respectively. The suffix  $m$  generally denotes maximum at a particular cross-section.

The experimental results, which follow, do not include finalized plots. These will be presented in the next chapter together with analytical considerations.

### 2.3.1 Free Jet and Impingement Regions

#### (i) The velocity field

Detailed velocity measurements were made only in run No. 1. Transverse distributions of the velocity component  $u$  are shown in Fig. 2.16. If  $u_m$  is the axial velocity and  $b_u$  is the value of  $y$  at which  $u = \frac{1}{2} u_m$ , these profiles may be normalized by plotting  $\frac{u}{u_m}$  vs  $\frac{y}{b_u}$ , as shown in Fig. 2.17. This figure suggests that the profiles remain similar as far from the nozzle as 85% of the impingement height,  $H$ . In this range, the error distribution:

$$f(\eta) = e^{-(0.834\eta)^2} \quad (2.12)$$

(where  $f(\eta) = \frac{u}{u_m}$ ,  $\eta = \frac{y}{b_u}$ ), describes the data very well, at least for  $\eta \leq 2.0$ . Tollmien's theoretical curve is also a good



description of the data although it is not shown. Due to considerable scatter occurring at small values of  $f(\eta)$ , it is difficult to determine the value of  $\eta$  for which  $f(\eta) = 0$ . However, the commonly accepted value of  $\bar{\eta} = 2.3$  appears reasonable. Therefore,

$$\bar{b}_u = 2.3b_u.$$

The profiles are not similar for  $\frac{x}{H}$  values greater than about 0.85, although the deviation is not large. It is interesting to note in Fig. 2.16 that the  $u$  components assume negative values at large values of  $y$ . As the wall is approached further, these components are reduced in magnitude and very near the wall they tend to disappear ( $x = 5.63$  in.). This may be explained if it is understood that at large values of  $y$ , the velocity vector assumes the direction of the (time average) streamlines of the wall jet. Therefore,  $u$  becomes negative and it is nothing but the  $v_1$  component of the wall jet velocity. As the wall is approached, the angle of the streamline with the horizontal tends to zero and so does the magnitude of  $v_1$ .

Fig. 2.18 shows distributions of the horizontal velocity component,  $v$ . As would be expected,  $v$  acquires a maximum value and then decreases slowly to become the  $u_1$  component of velocity in the wall jet.

As the flow deflects in the impingement region, a boundary layer forms on the wall. The velocity vector is almost parallel to the wall and acquires a maximum value at the edge of the boundary layer. This quantity is denoted by  $u_{m1}$  and a typical variation with



$x_1$  is shown in Fig. 2.19. This resembles the curves of Fig. 2.18, although  $u_{m1}$  does not necessarily occur at a constant distance above the wall.

The distribution of the product  $u.v$  is shown in Fig. 2.20. Physically,  $uv$  if multiplied by  $\rho$  represents the flux of  $x$ -momentum in the  $y$ -direction. Figure 2.20 suggests that  $uv$  is almost independent of  $x$  for  $y \leq 0.2$  in. As we shall see in the next chapter, this observation is of considerable importance in predicting the variation of  $u_m$  with  $x$  in the impingement region.

#### (ii) The Pressure Field

Figure 2.21 shows pressure profiles in the impingement region. The symbol  $h_{10}$  stands for manometer reading at a slope 1 vertical to 10 horizontal. Reliable profiles for  $\frac{x}{H} \leq 0.70$  could not be obtained with the present equipment because the pressure was so small that the relative error became unacceptable. The term pressure will be used to denote the excess static pressure above the atmospheric in the remaining part of this thesis. If  $p_m$  is the axial pressure and  $b_p$  is the value of  $y$  at which  $p = \frac{1}{2} p_m$ , then the pressure profiles may be reduced to a single curve if  $\frac{p}{p_m}$  is plotted against  $\frac{y}{b_p}$ . This is shown in Fig. 2.22. If  $\frac{p}{p_m} = f(\eta)$ ,  $\eta = y/b_p$ , the function:

$$f(\eta) = e^{-(0.834\eta)^2} \quad (2.12A)$$

describes the data reasonably well.



Figure 2.23, shows a typical wall pressure distribution. In the next chapter it will be shown how all the wall pressure profiles may be reduced to a single curve.

(iii) Length, Velocity and Pressure Scales

We have seen already how the velocity and pressure profiles may be made similar. For full evaluation of the velocity and pressure fields the variation of the scales  $u_m$ ,  $b_u$ ,  $p_m$ ,  $b_p$  must be known.

Figure 2.24 shows the variation of  $\frac{u_m}{U_o}$  with  $\frac{x}{2b_o}$  for different dimensionless heights  $\frac{H}{2b_o}$ . The decay of the maximum velocity in the free jet is given by the equation:

$$\frac{u_m}{U_o} = \frac{C_1}{\sqrt{\frac{x - x'}{2b_o}}} \quad (2.13)$$

where  $C_1$  is a constant with an average value of 2.35 and  $x'$  is a virtual origin correction, usually equal to a few nozzle widths. The present data follow the above law for a certain distance, after which they deviate more and more from this law. The data are described by Eq. 2.13 if  $C_1 = 2.40$  and  $x' = 2.5 (2b_o)$ . Therefore, for this set of experiments:

$$\frac{u_m}{U_o} = \frac{2.40}{\sqrt{\frac{x}{2b_o} - 2.5}} \quad (2.14)$$

This equation is applicable at distances greater than the length of





the potential core which for the present data is about 8 nozzle widths.

A typical distribution of the axial pressure,  $p_m$ , is shown in Fig. 2.25. The pressure is seen to increase rapidly for  $x \gtrsim 4.5$  in., reaching a maximum value at the wall.

Figures 2.26 and 2.27 show the variation of the length scales  $b_u$  and  $b_p$  with distance  $x$ . The scale  $b_u$  is seen to vary linearly with  $x$  for  $x \lesssim 4$  in., following the equation:

$$b_u = 0.1(x + 0.9) \quad (2.15)$$

Equation 2.15 is almost identical with the free jet equation which states that  $b_u = 0.097(x + x'')$ , where  $x''$  is a virtual origin correction, not necessarily corresponding to the virtual origin for velocities.

#### (iv) The Wall Shear Stress

Figure 2.28 shows typical variations of shear velocity,  $u_*$ , with distance  $x_1$ , along the wall. By definition  $u_* = \sqrt{\tau_0/\rho}$ . The shear velocity, and therefore the shear stress, rises from zero at the axis to a maximum value, decreasing steadily beyond this point. Since these data were obtained by use of Patel's curves [13] for zero pressure gradient flows, their reliability is subject to certain limitations, because the pressure gradient is significant in this region. These limitations will be discussed in detail in the next chapter.



### 2.3.2 Wall Jet Region

This region was investigated with respect to the velocity field, the wall shear stress and the growth of the jet thickness. Since the horizontal velocity component,  $u_1$ , is almost equal to the total magnitude of the velocity vector and the vertical component,  $v_1$ , is very small in this region, the velocity field was studied with respect to the  $u_1$  component only.

#### (i) Velocity Distribution

Typical velocity distributions in the  $y_1$  direction are shown in Fig. 2.29.

If  $b_1$  is the value of  $y_1$  at which  $u_1 = \frac{1}{2} u_{m1}$  and  $\frac{\partial u_1}{\partial y_1} < 0$ , the velocity profiles may be reduced to a single similarity curve if  $\frac{u_1}{u_{m1}}$  is plotted against  $\frac{y_1}{b_1}$ . This is shown in Fig. 2.30.

Although, it is difficult to determine the value of  $\eta_1$  at which  $f(\eta_1) = 0$ , a value  $\eta_1 = 1.8$  appears to be reasonable. Thus  $\overline{b_1} = 1.8 b_1$ . The value of  $\eta_1$  at which  $f(\eta_1) = 1$  may be taken as  $\eta_1 = 0.16$ . Thus,  $\delta = 0.16 b_1$ . The present results agree closely with those reported by Schauer and Eustis [1]. The distribution for the classical wall jet [16] is also shown and is seen to agree well with the data for  $\eta_1 \leq 1.0$ . The discrepancy between the experimental data and the classical wall jet curve may be explained if it is recognized that the velocity  $u_1$  is likely to assume negative values for  $\eta_1 > 1.8$ , which are nothing but entrainment velocities,  $v_e$ , for the initial jet. Such negative components are not present in the case



of the classical wall jet, so that  $u_1$  tends to zero at a somewhat larger value of  $\eta_1$ . According to the above, the velocity profile could be sketched as shown in Fig. 2.31.

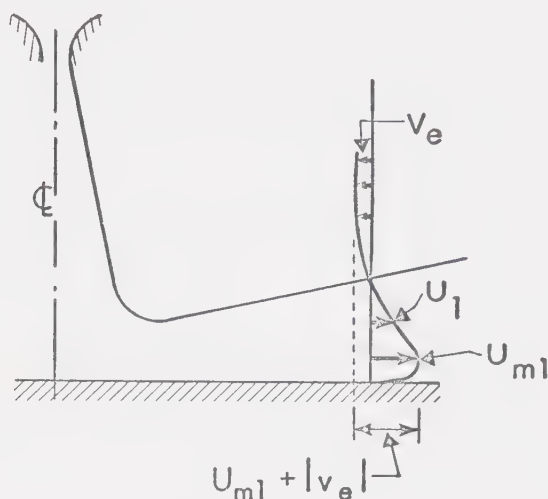


FIG. 2.31 SKETCH OF 'TRUE' VELOCITY PROFILE

Then, the "true" velocity scale would be  $u_{ml} + |v_e|$  and the "true" length scale would be somewhat larger than  $b_1$ , say  $b_1'$ . The variation of  $\frac{u_1 + |v_e|}{u_{ml} + |v_e|}$  with  $\frac{y_1}{b_1}$  should agree better with the classical wall jet curve.

Measurements of  $v_e$  components were not carried out in this work, although their existence was noticed.

A transitional zone exists between the impingement and wall jet regions in which the flow undergoes a process towards establishment of similarity. It is difficult to define the distance after which the profiles become similar. This is because transition towards



similarity takes place gradually. Careful inspection of the data suggests that the free-mixing region is established first (i.e. at earlier  $x_1$  stations), followed by establishment of similarity in the boundary layer.

## (ii) Velocity and Length Scales

Figure 2.32 shows the decay of the dimensionless velocity scale  $\frac{u_{m1}}{U_o}$  with dimensionless distance,  $\frac{x_1}{2b_o}$ , from the stagnation point. A dependence on the dimensionless height  $\frac{H}{2b_o}$  is obvious. Data reported by Schauer and Eustis [1], are also shown. These data were obtained at a value of nozzle Reynolds number of about  $R_o = 43,000$ . Since the present results were obtained for  $R_o$  less than 10,000, a dependence of  $\frac{u_{m1}}{U_o}$  upon the Reynolds number,  $R_o$ , is indicated.

The variation of the length scale,  $b_1$ , with  $x_1$  is shown in Fig. 2.33. The results indicate a linear variation. This is in agreement with what is known already about the wall jet [17, ch. 10]. The value of  $C_b = \frac{db}{dx_1}$  is approximately 0.04 and appears to be independent of the parameter  $\frac{H}{2b_o}$ . This conclusion is supported by the results of [1], where  $C_b \approx 0.10$  for  $\frac{H}{2b_o} = 20$  and 40. The difference between the present value of  $C_b$  and that of [1] is possibly due to the large difference in the Reynolds number. An average value of  $C_b$  in classical wall jets may be taken as 0.068 [17, ch. 10].





(iii) Wall Shear Stress

This will be best studied in conjunction with analytical considerations in the next chapter.



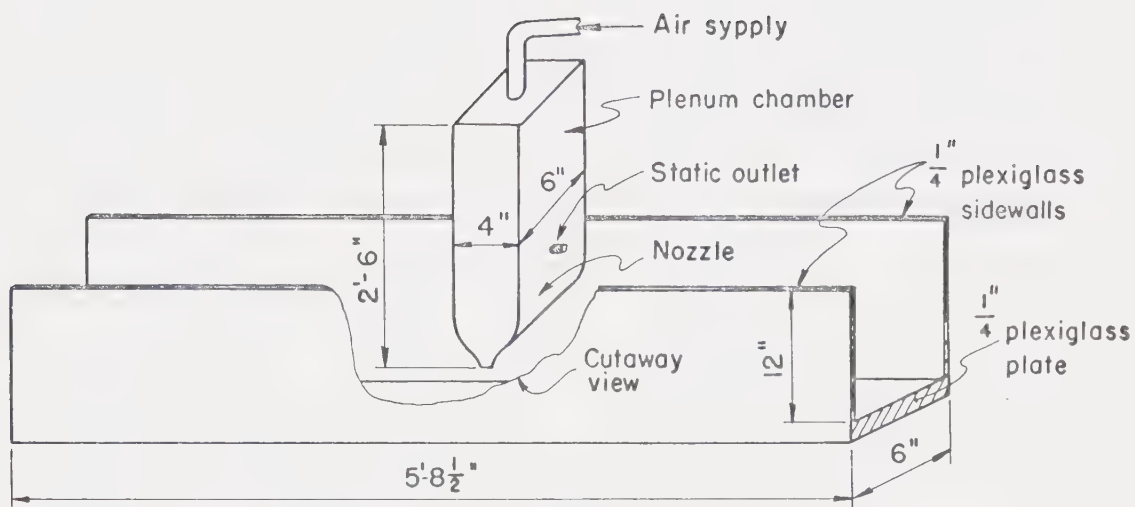


FIG. 2.1 EXPERIMENTAL SET UP  
[NOT TO SCALE]

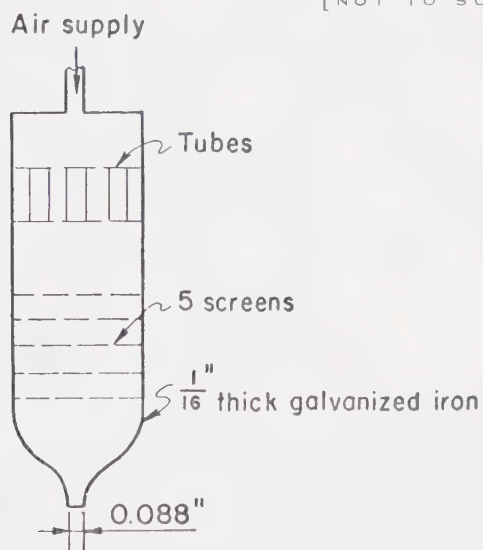
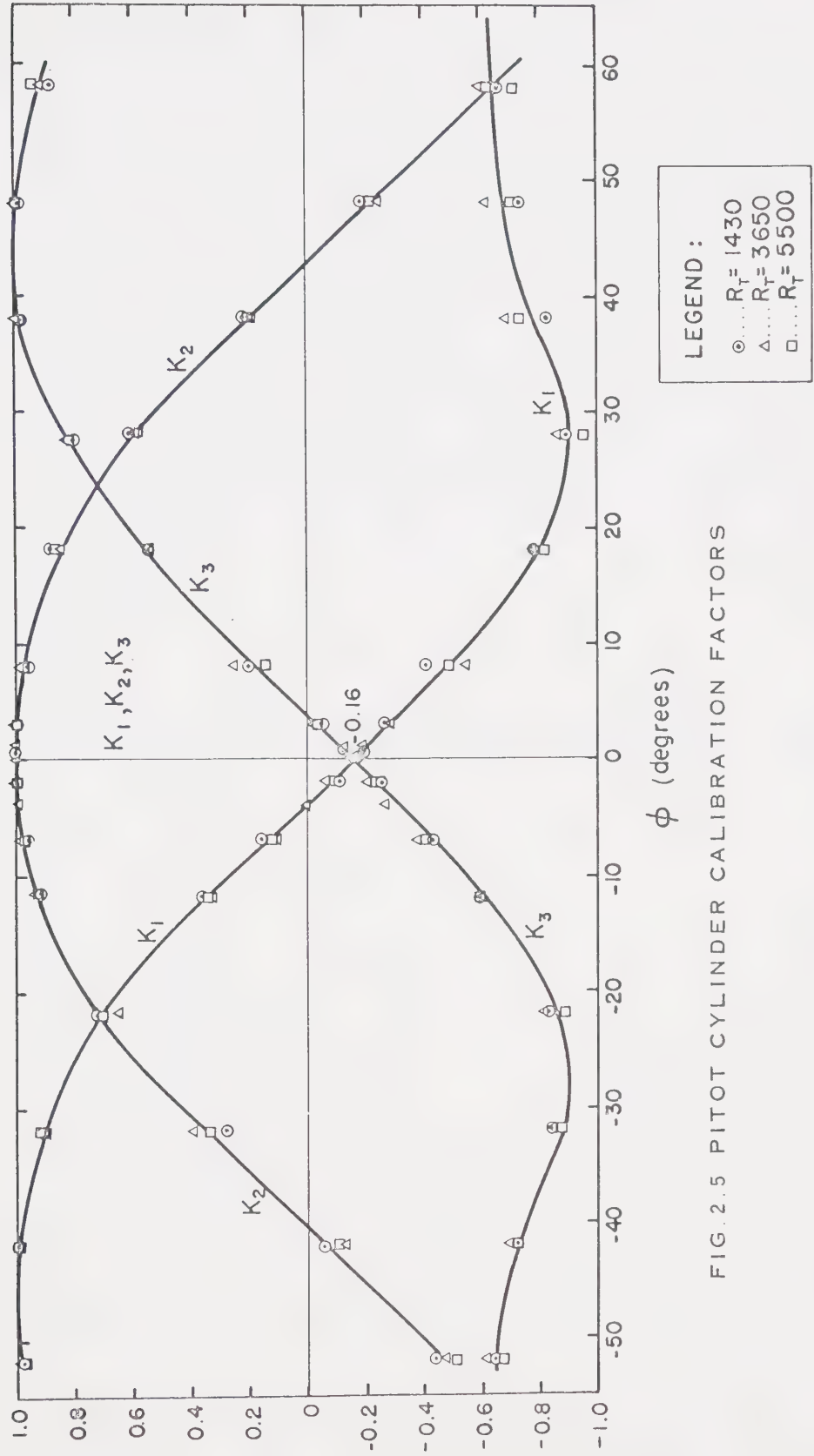


FIG. 2.2 NOZZLE AND CHAMBER DETAILS  
[NOT TO SCALE]







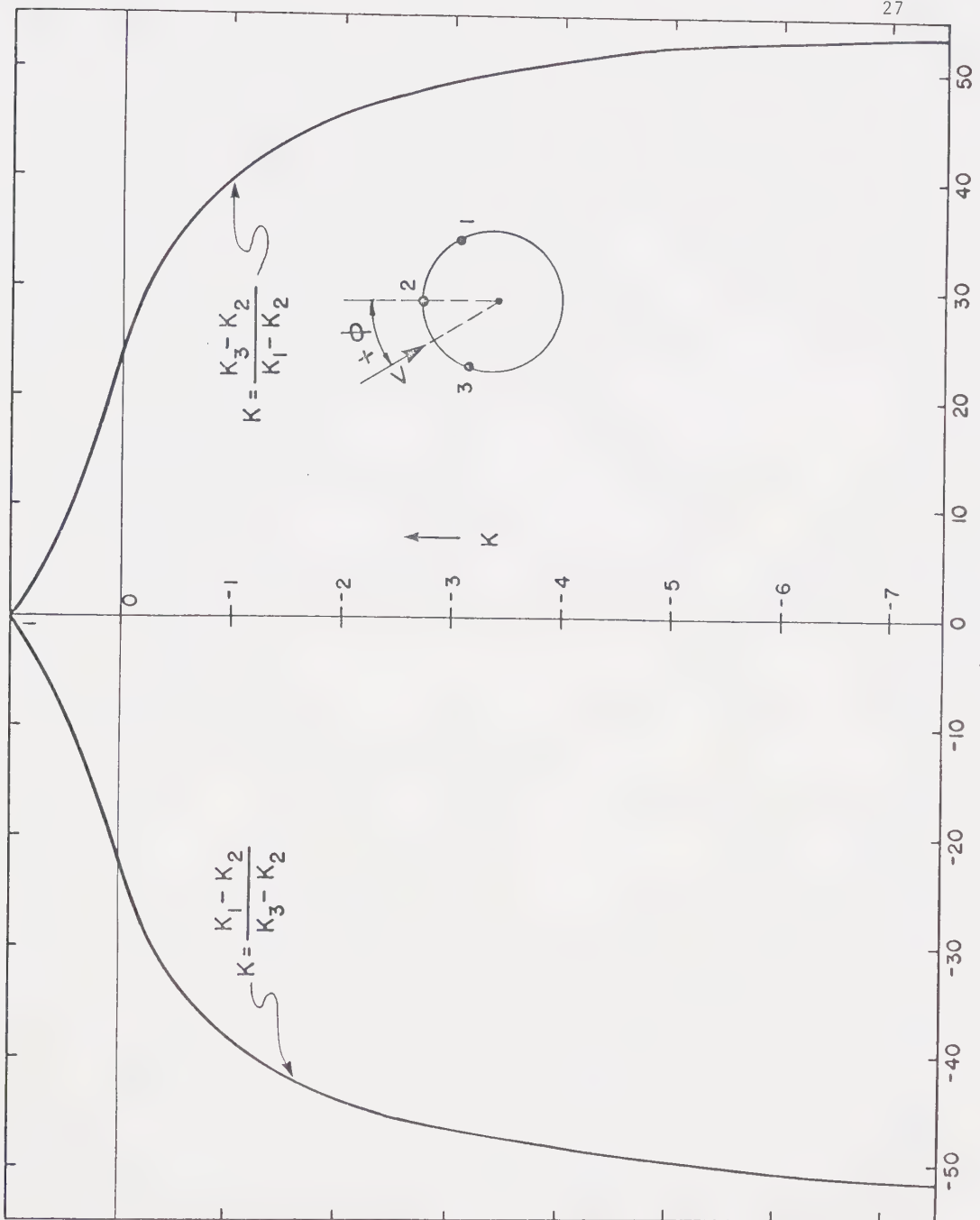


FIG. 2.6 CALIBRATION FACTOR  $K$





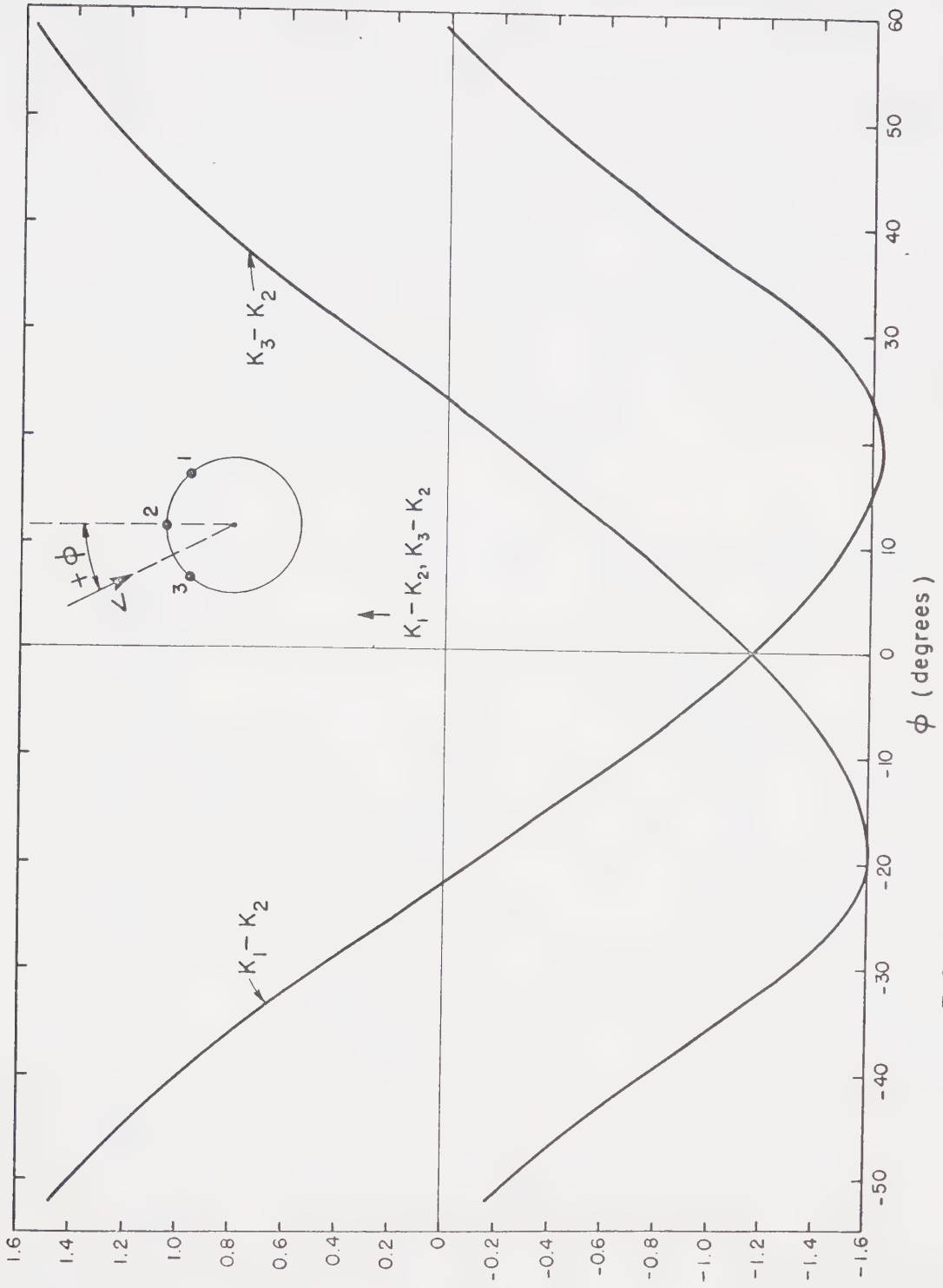
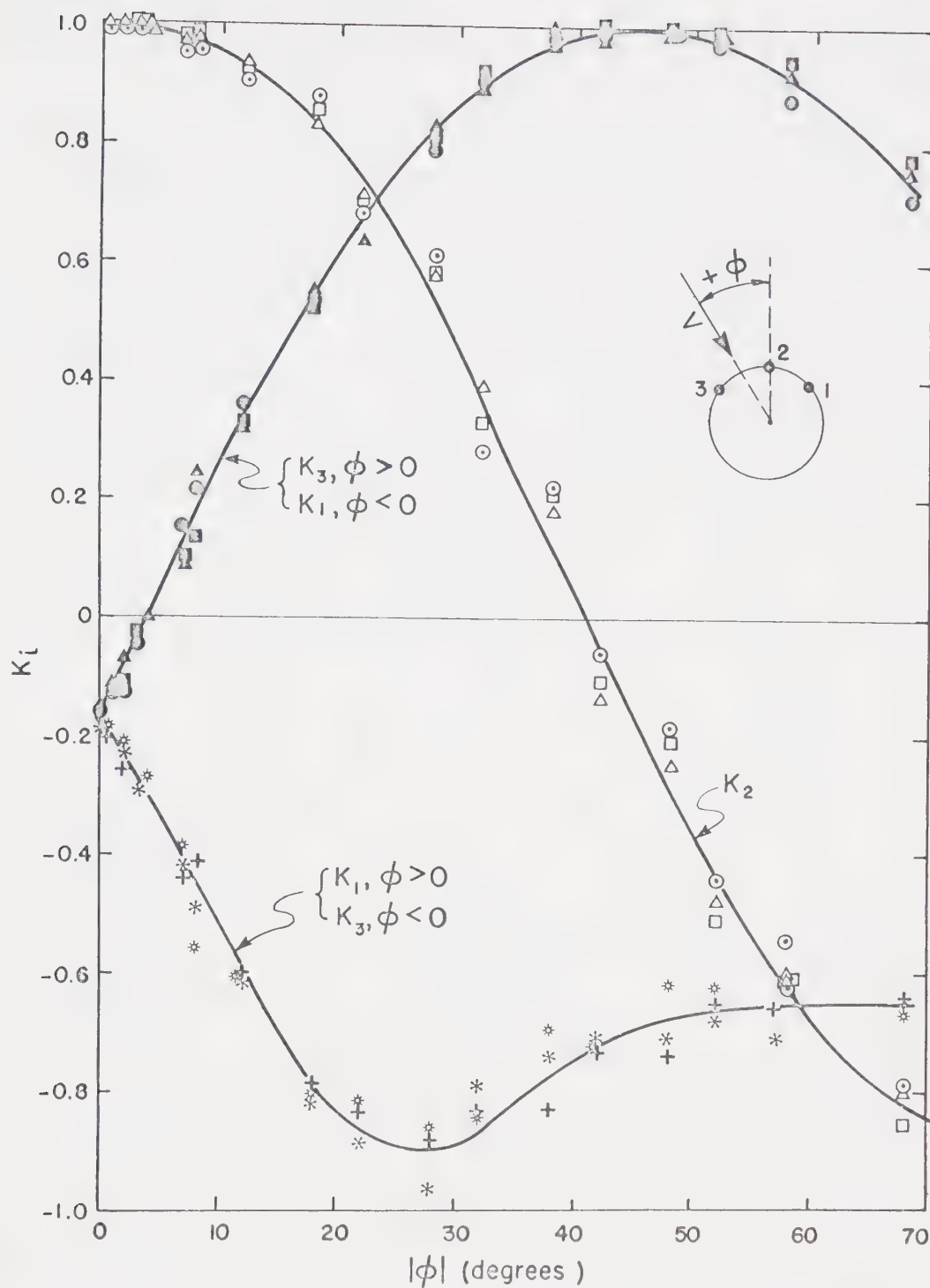


FIG. 2.7 CALIBRATION FACTORS  $K_1 - K_2$  AND  $K_3 - K_2$



FIG. 2.8 GENERALIZED FACTORS  $K_1, K_2, K_3$ 

Legend :	$\circ R_T = 1430$	} $K_2$	$+ R_T = 1430$	} $K_1$	$\circ R_T = 1430$	} $K_3$
	$\triangle R_T = 3650$		$* R_T = 3650$		$\triangle R_T = 3650$	
	$\square R_T = 5500$		$* R_T = 5500$		$\square R_T = 5500$	



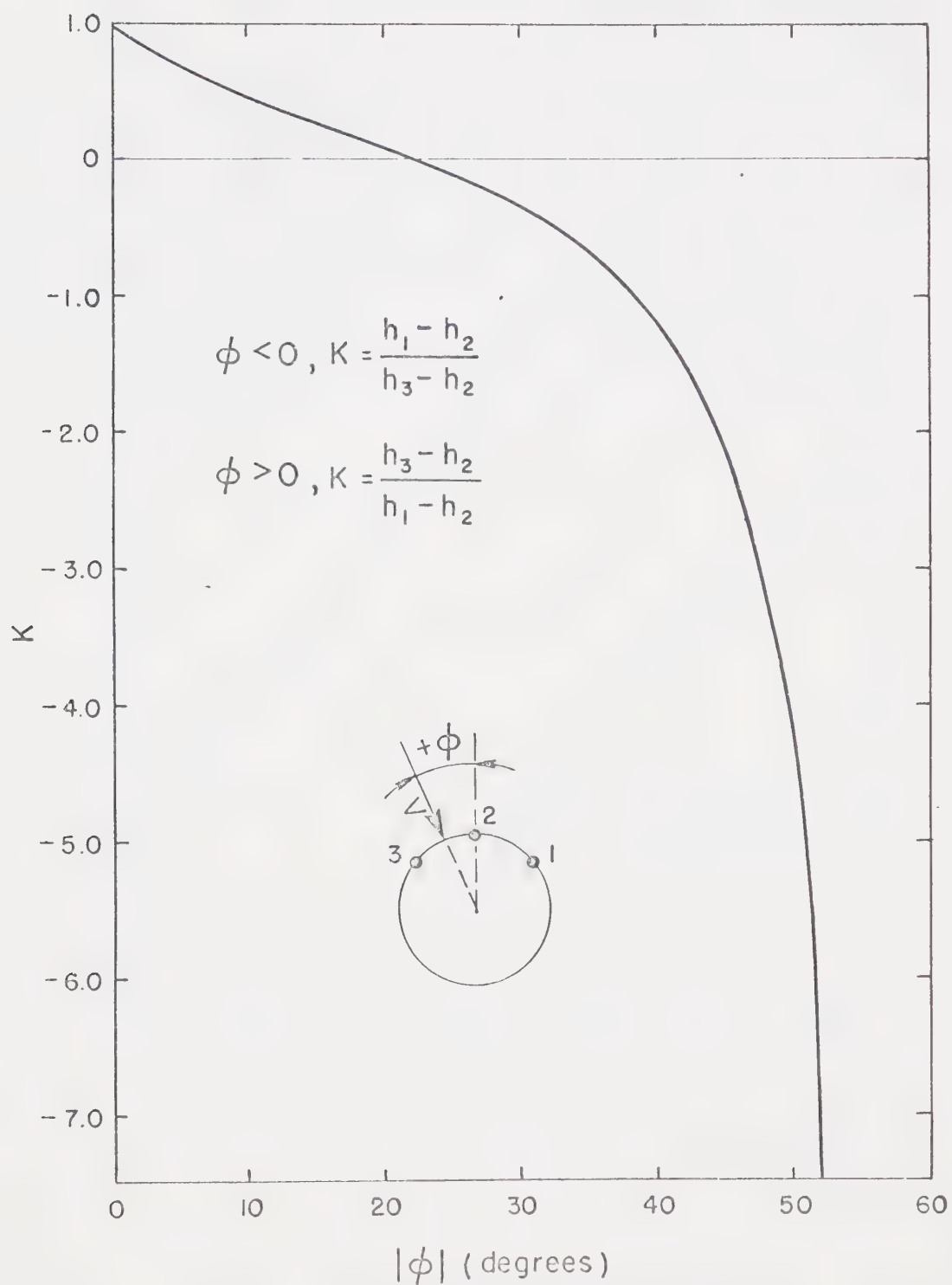


FIG. 2.9 GENERALIZED FACTOR K



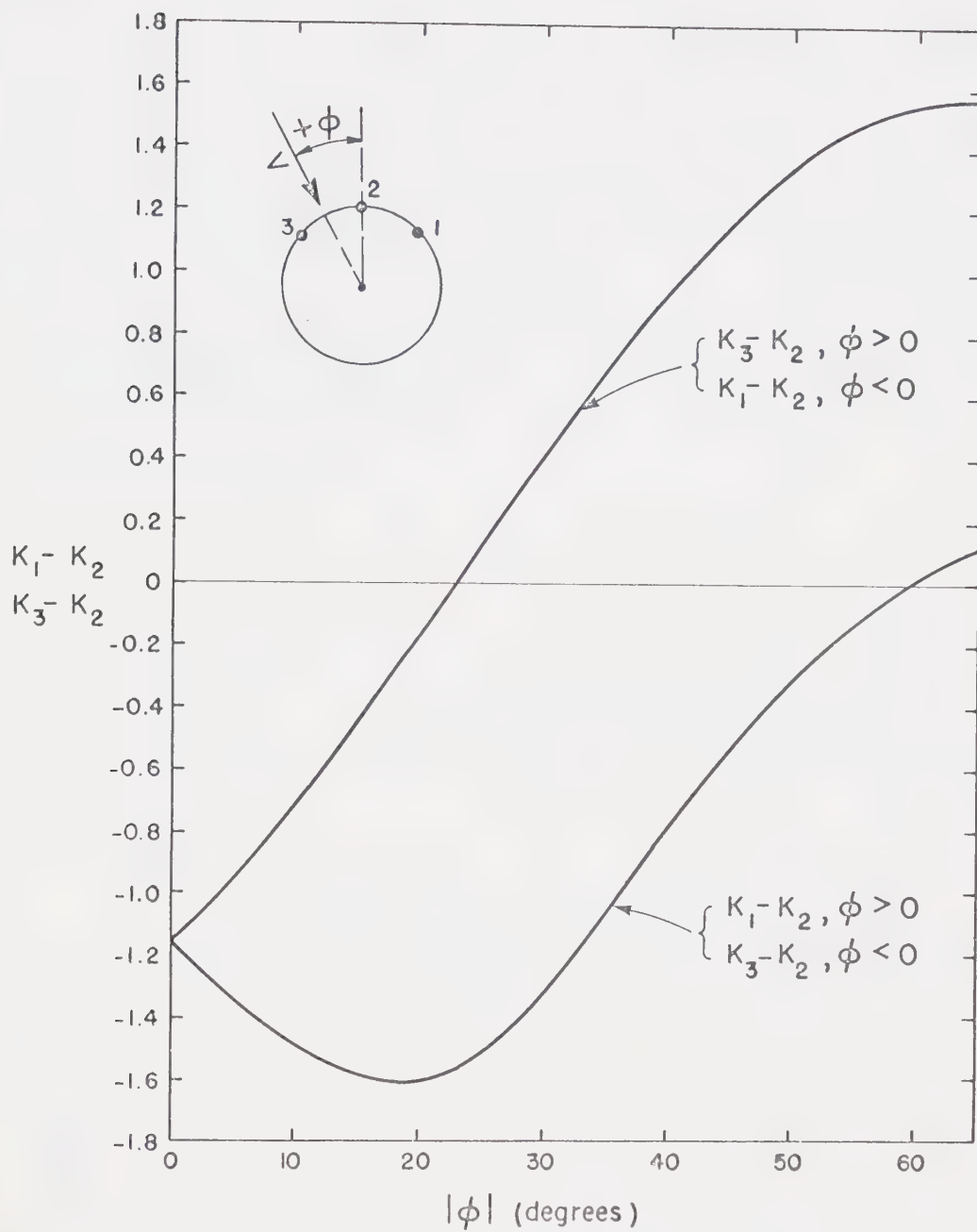


FIG. 2.10 GENERALIZED FACTORS  $K_1 - K_2$  AND  $K_3 - K_2$









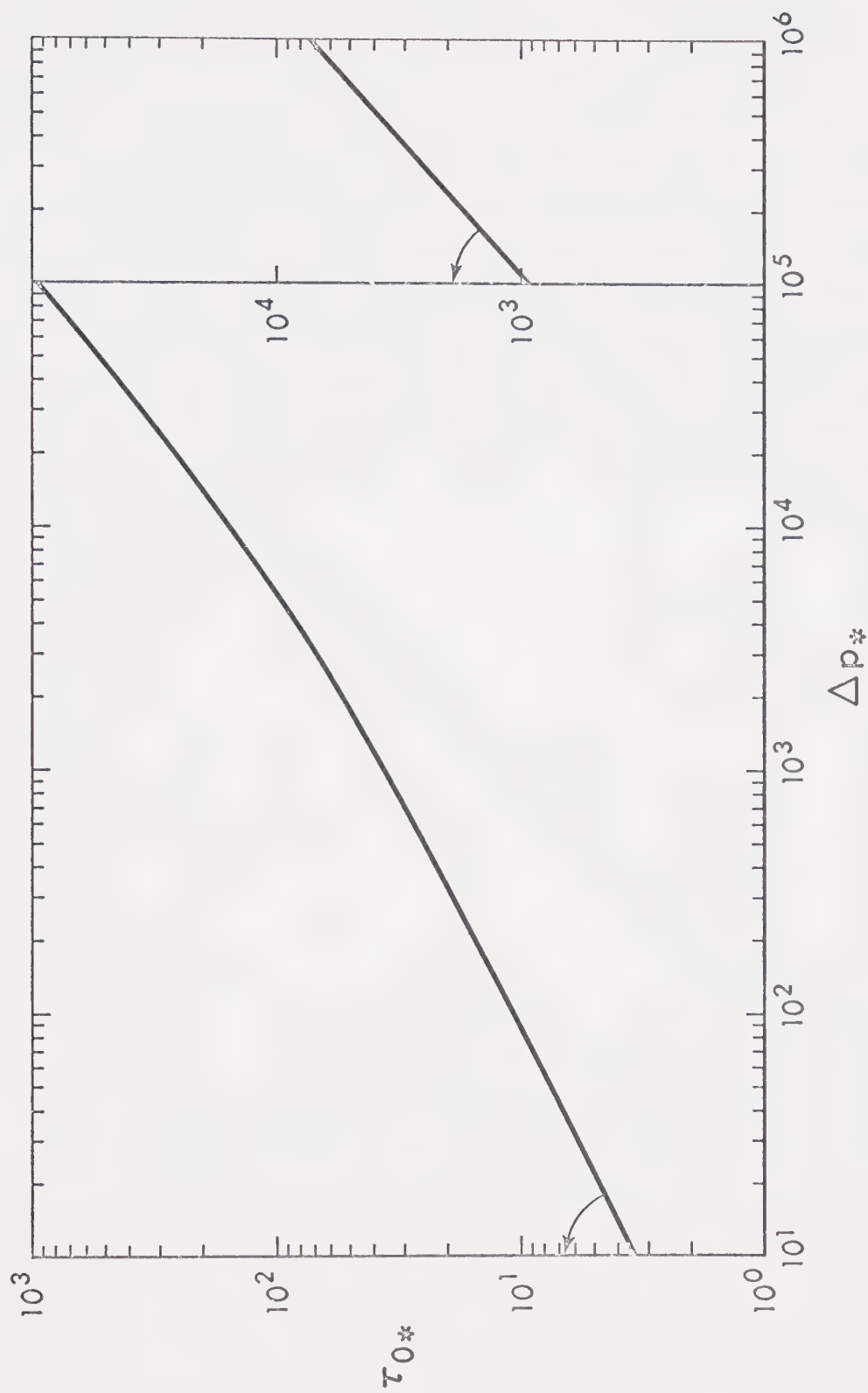


FIG. 2.13 PATEL EQUATIONS FOR SMOOTH WALLS



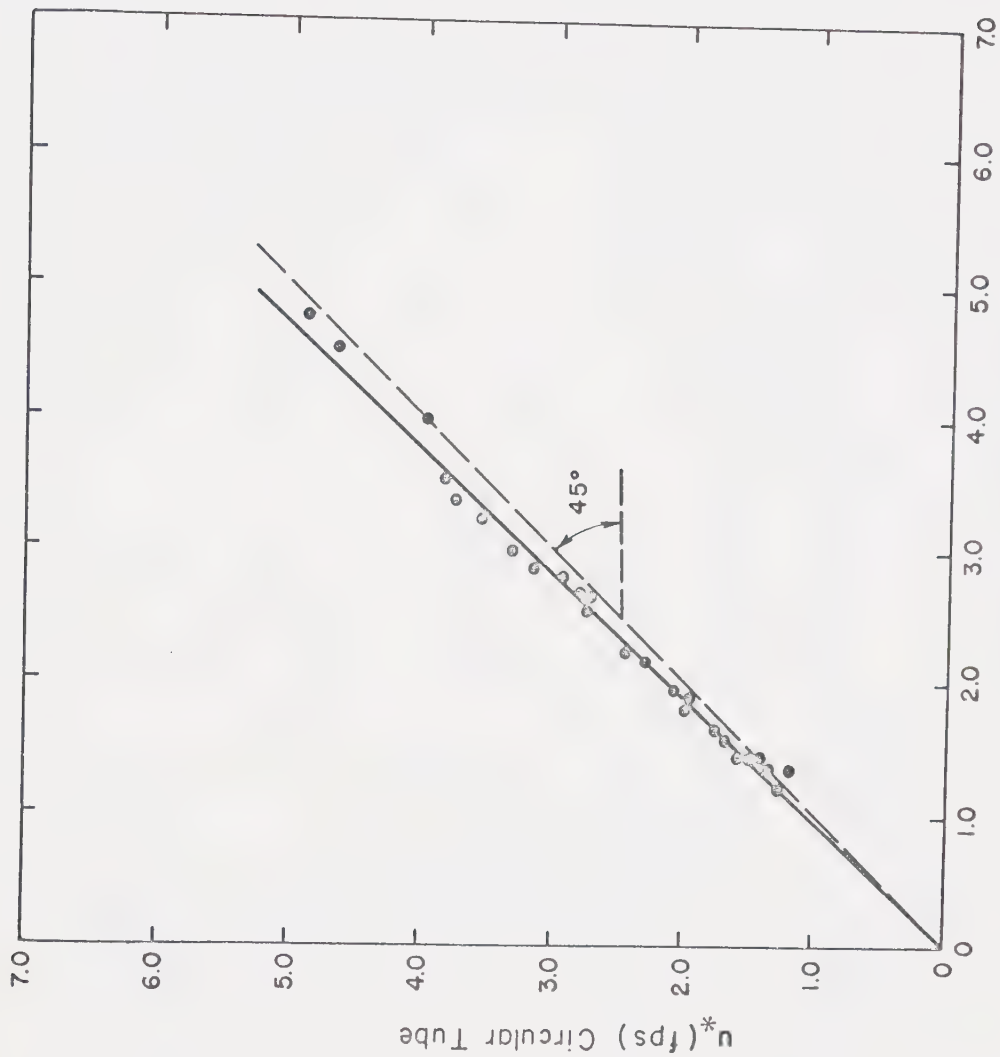


FIG. 2.14 CHART TO CORRECT FLATTENED TUBE READINGS



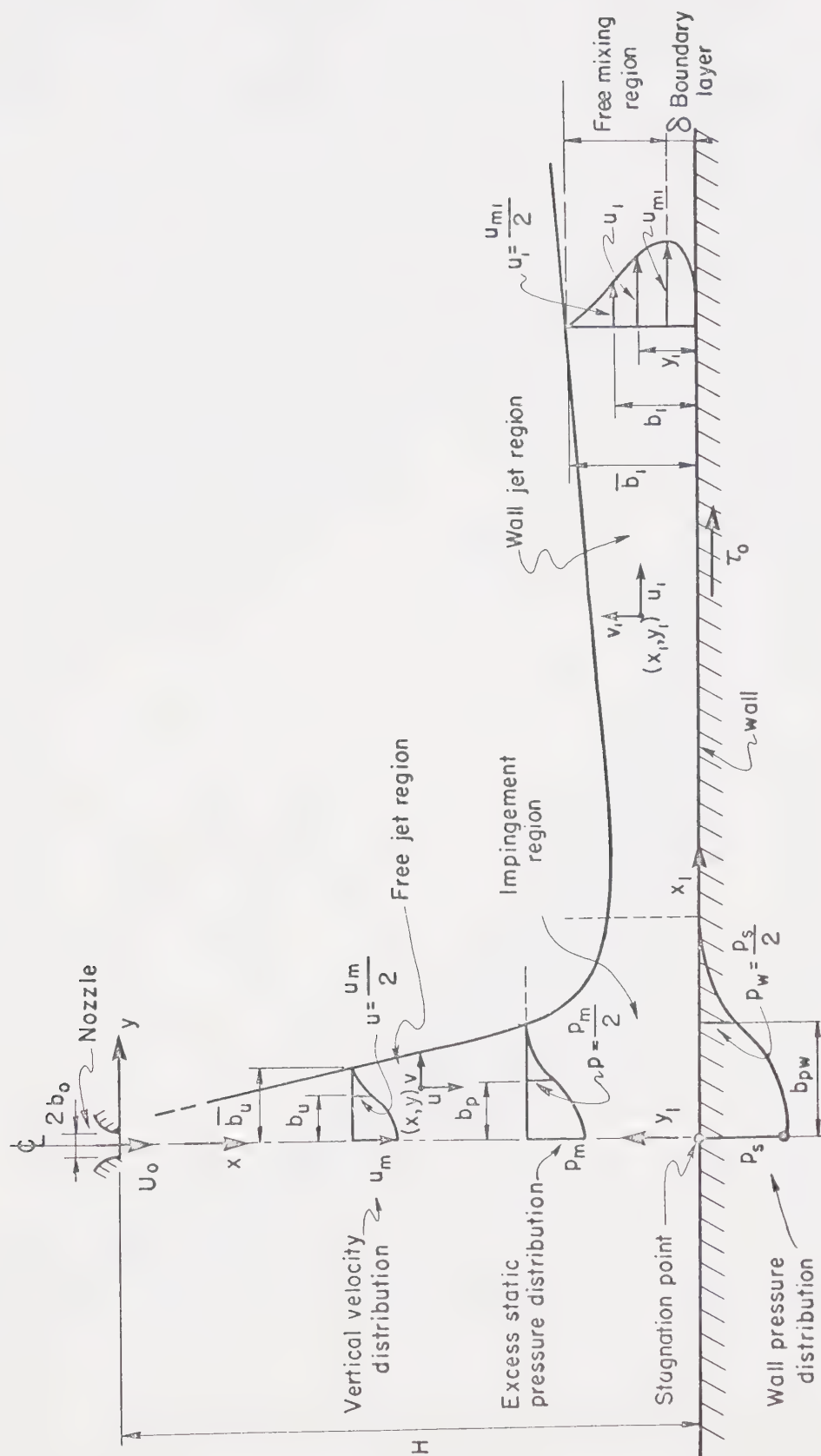


FIG. 2.15 DEFINITION SKETCH





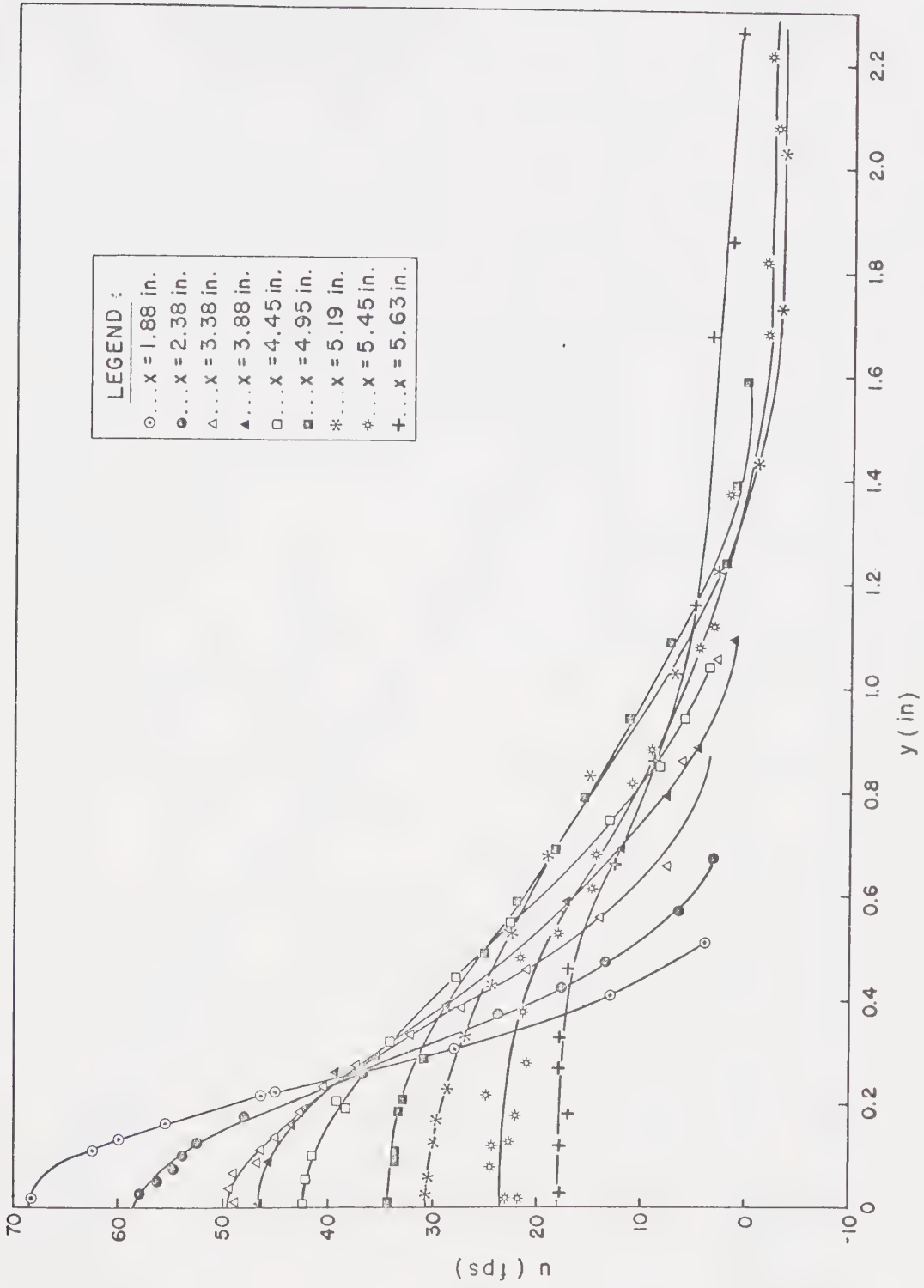


FIG. 2.16 VELOCITY PROFILES IN FREE JET AND IMPINGEMENT REGIONS [RUN NO. 1]



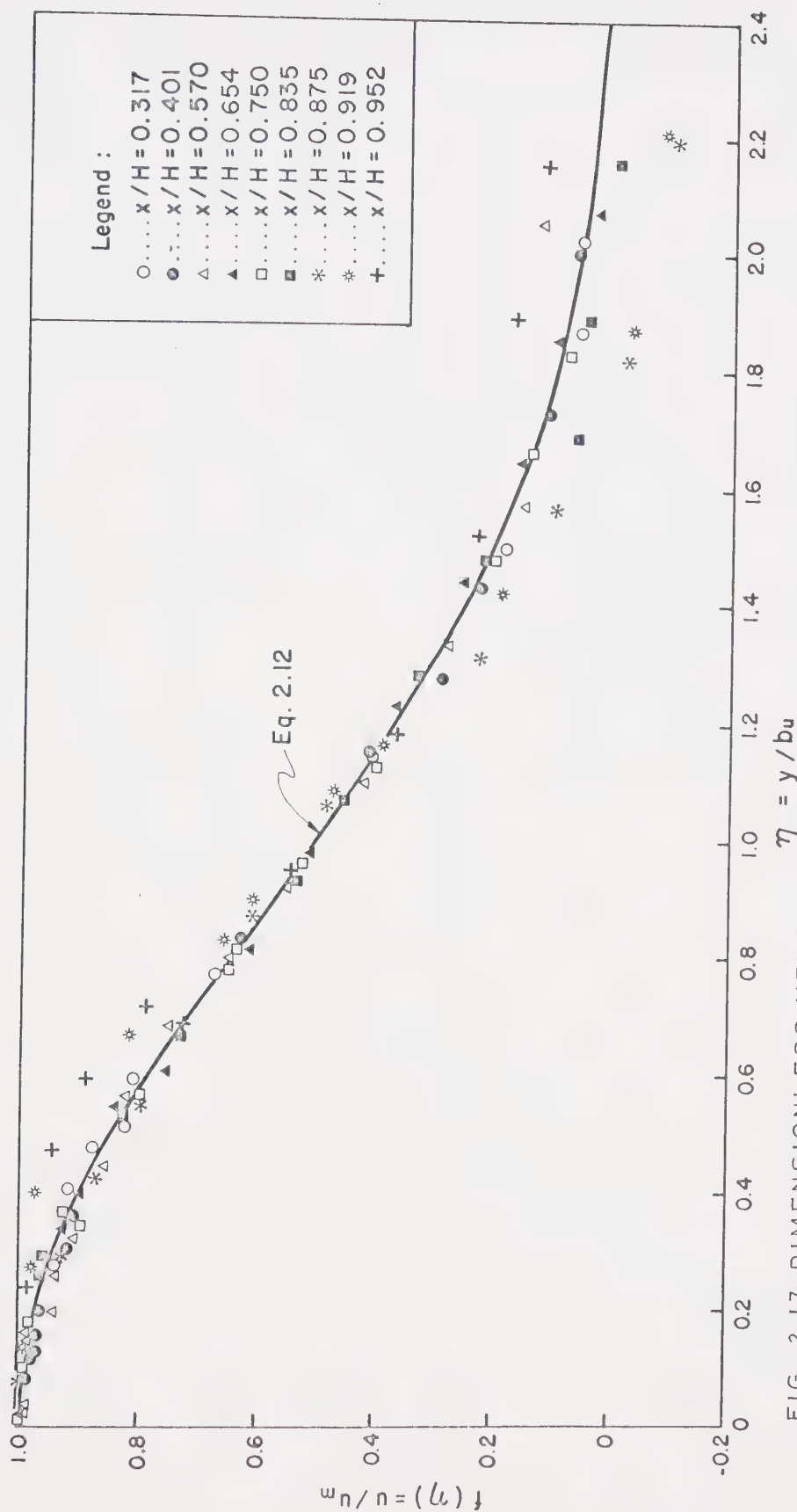


FIG. 2.17 DIMENSIONLESS VELOCITY DISTRIBUTION IN FREE JET AND IMPINGEMENT REGIONS [RUN NO.1]



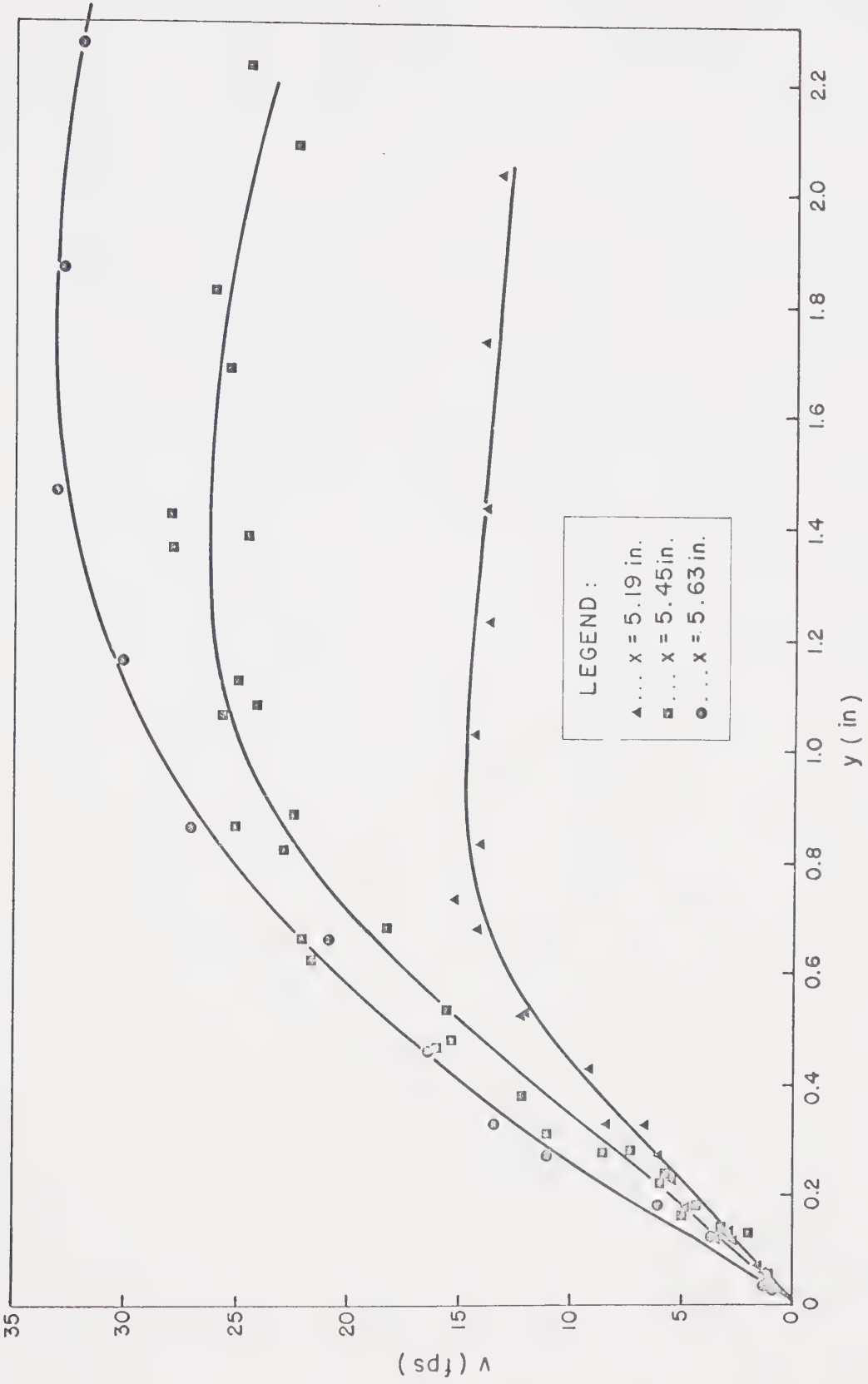


FIG. 2.18 DISTRIBUTION OF  $v$  COMPONENT IN IMPINGEMENT REGION [RUN NO.1]



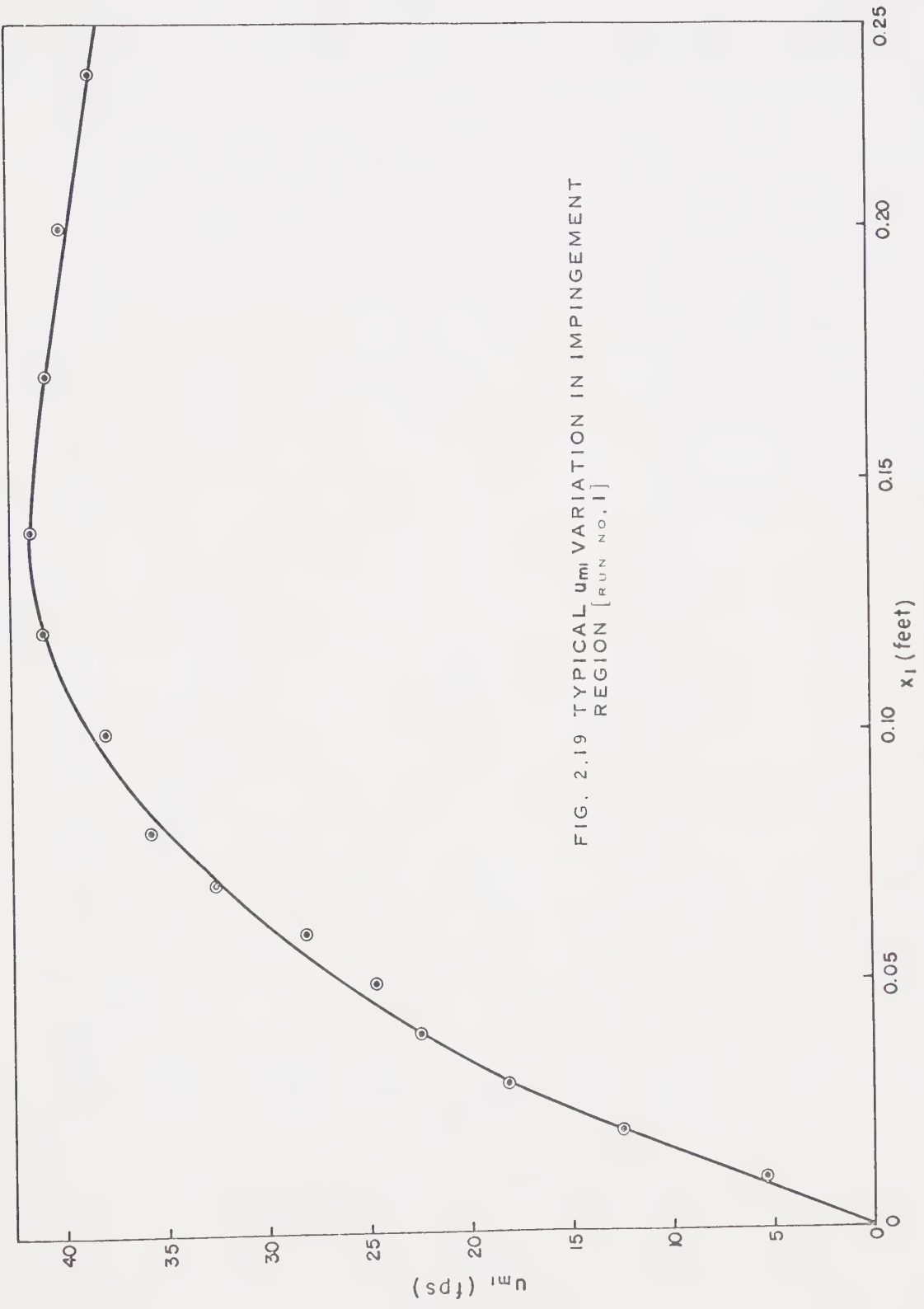


FIG. 2.19 TYPICAL  $u_m$  VARIATION IN IMPINGEMENT REGION [RUN NO. 1]





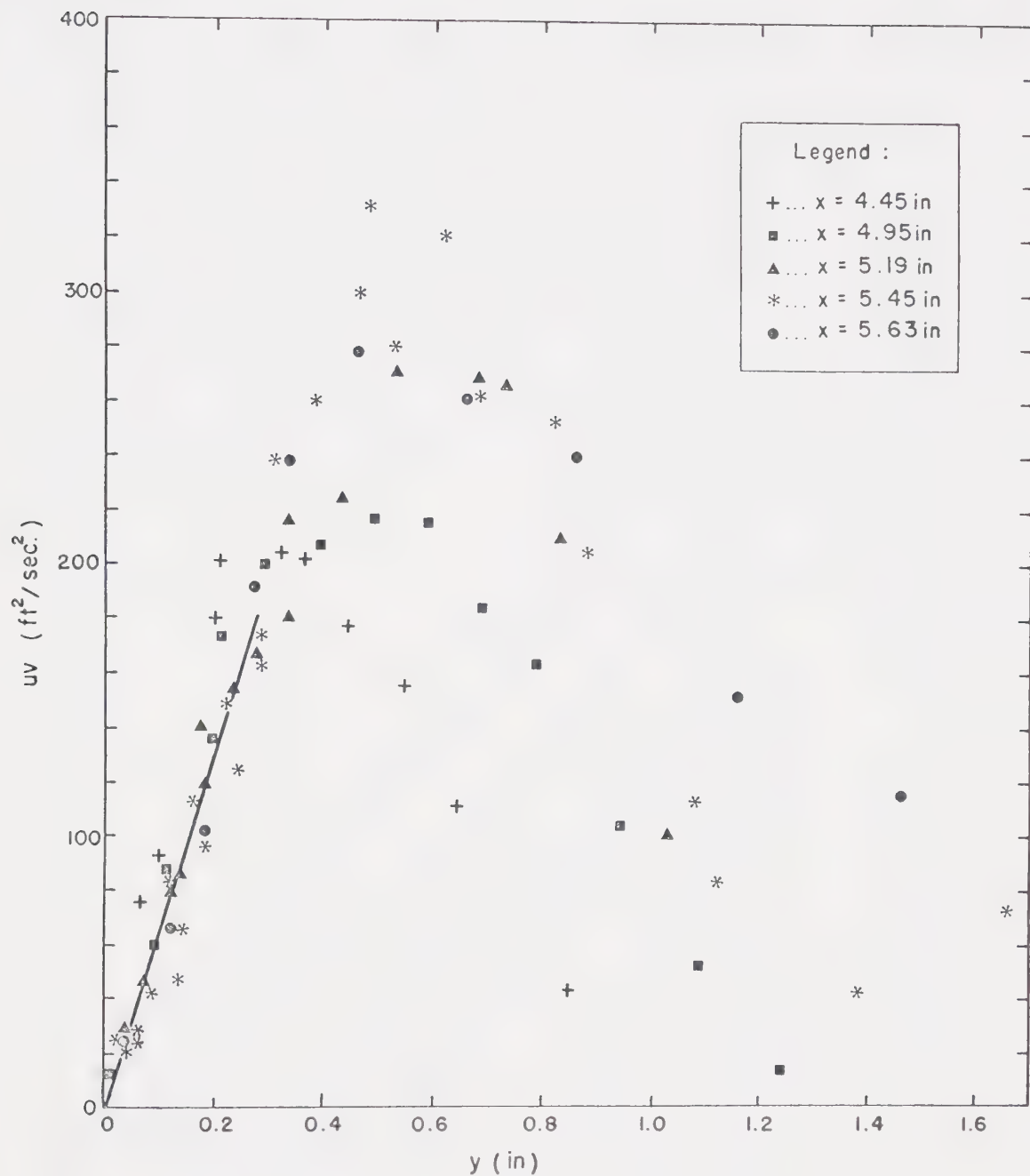


FIG. 2.20 DISTRIBUTION OF THE PRODUCT  $uv$  IN IMPINGEMENT REGION [RUN NO. 1]



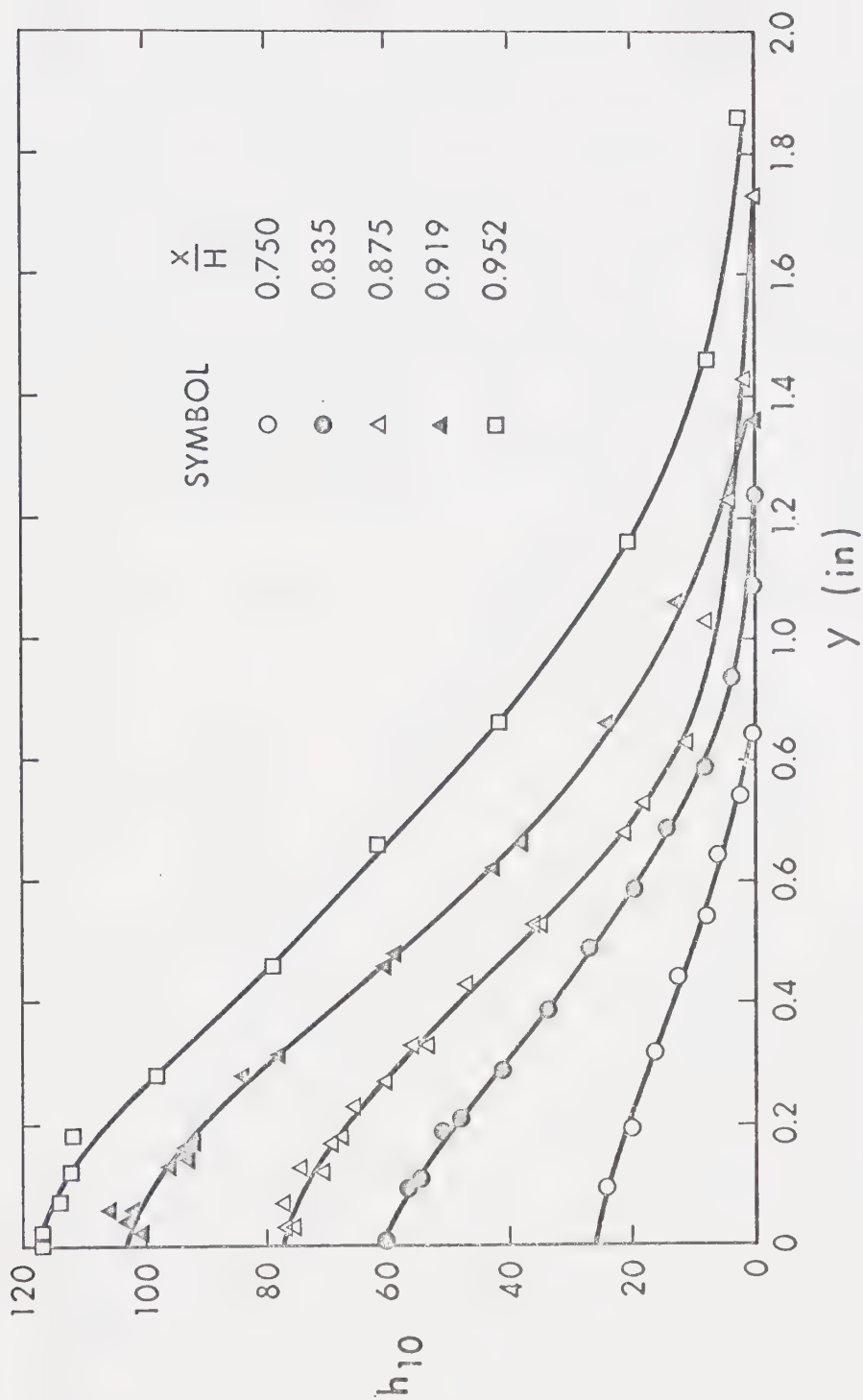


FIG. 2.21 EXCESS STATIC PRESSURE IN IMPINGEMENT REGION [RUN NO. 1]  
 $[h_{10}: \text{MANOMETER RDG. AT SLOPE 1:10}]$



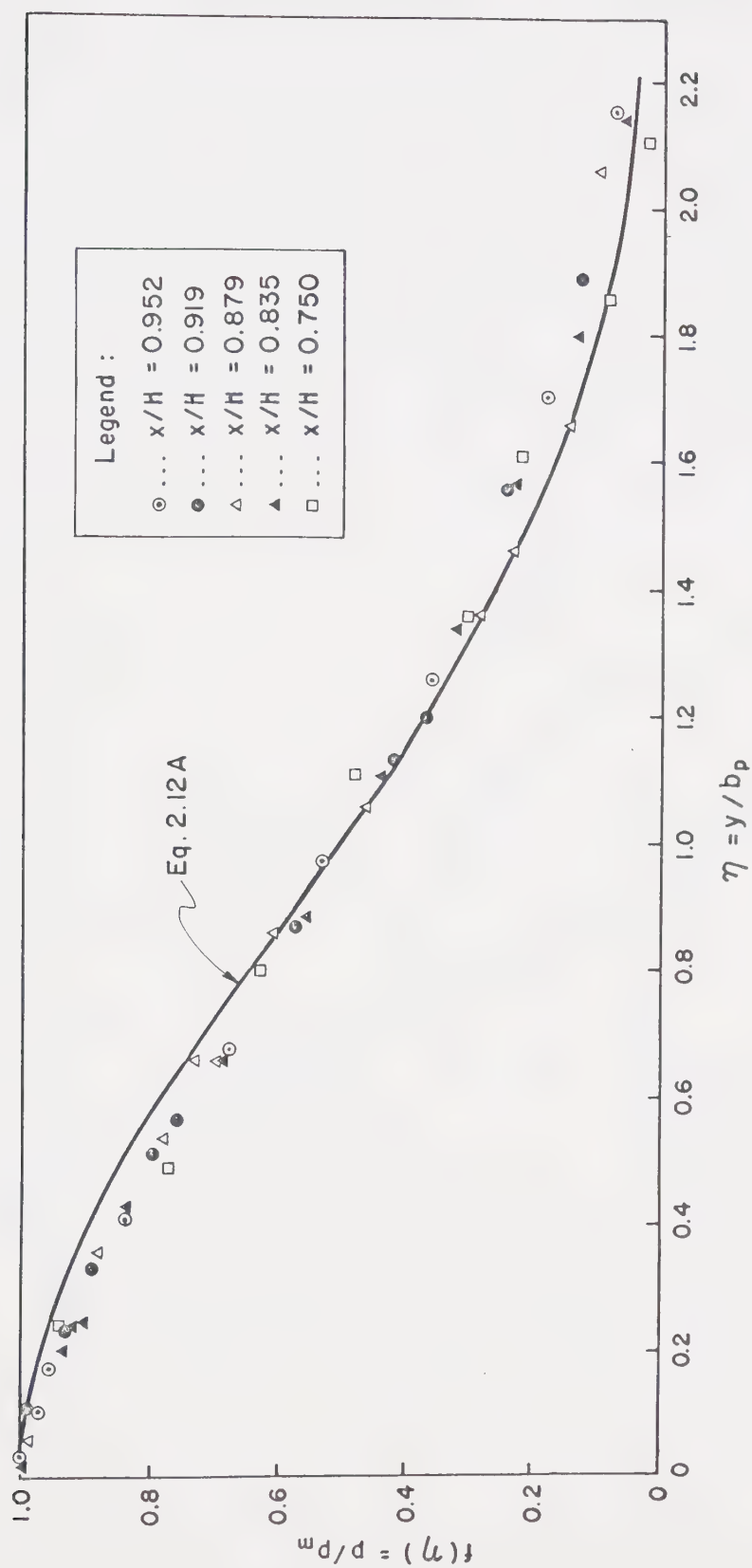


FIG. 2.22 DIMENSIONLESS PRESSURE DISTRIBUTION IN IMPINGEMENT REGION [RUN NO. 1]



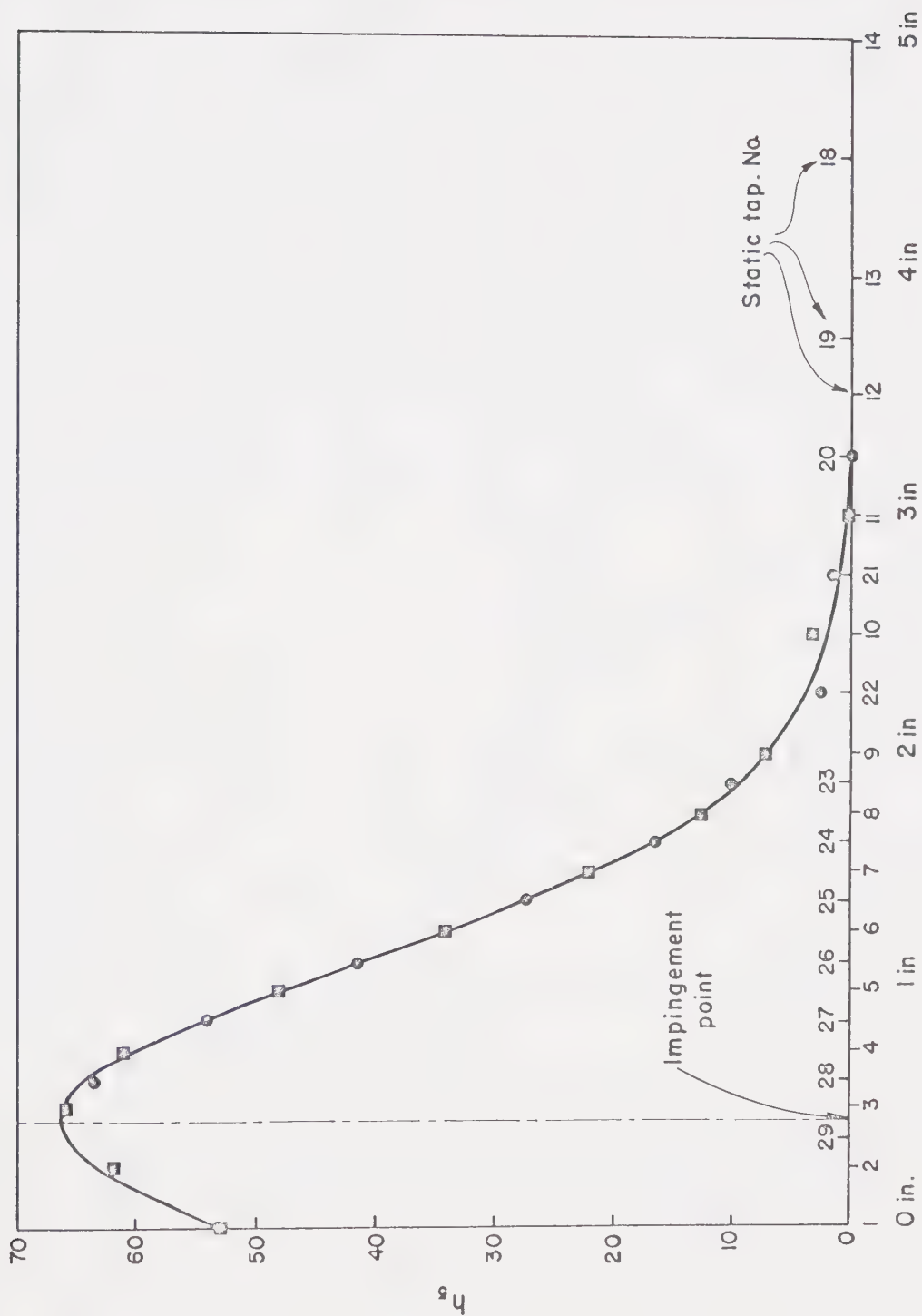


FIG. 2.23 TYPICAL WALL PRESSURE DISTRIBUTION [RUN NO. 1]  
 $[h_s: \text{MANOMETER RDG. AT SLOPE 1:5}]$





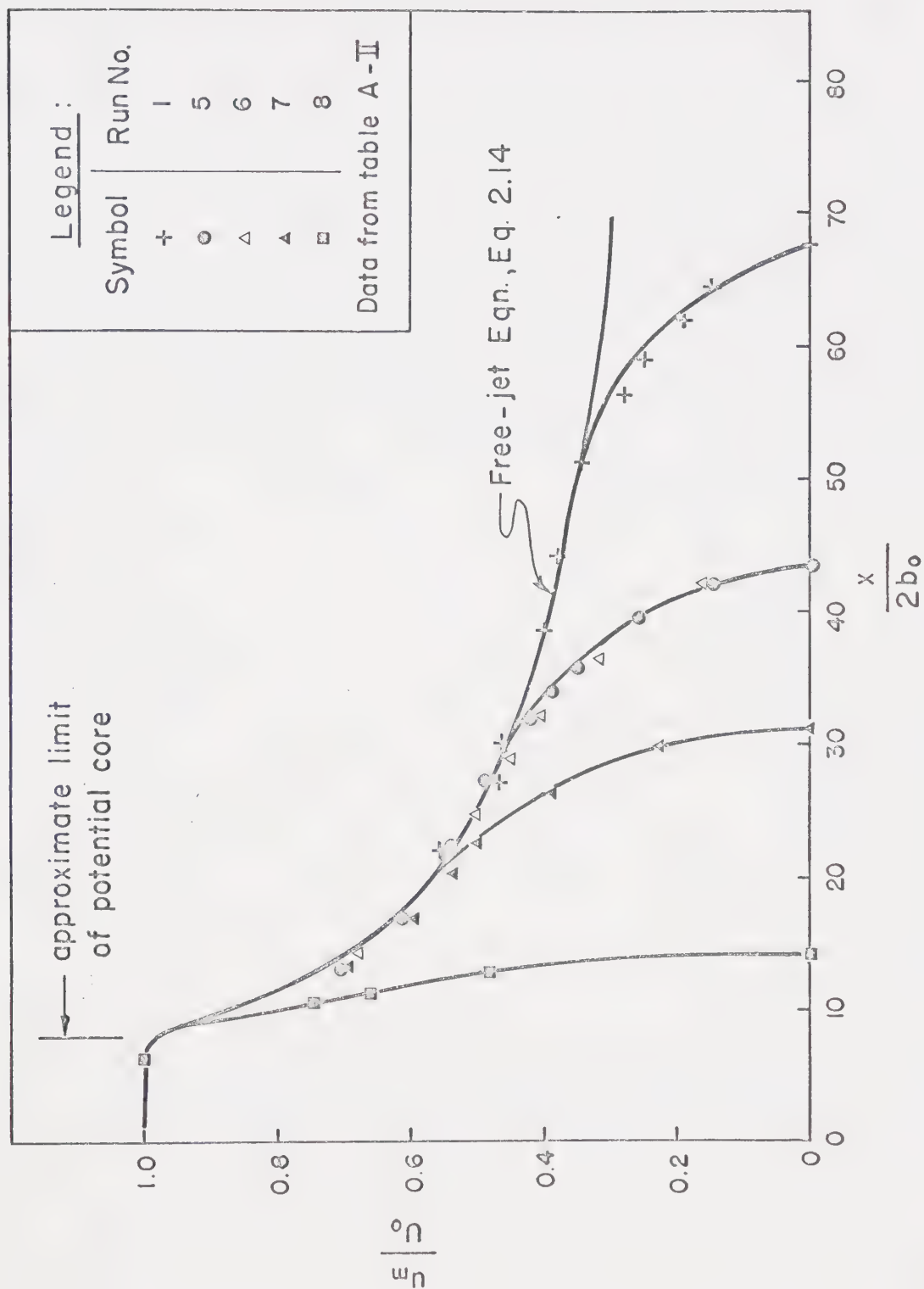


FIG. 2.24 DECAY OF AXIAL VELOCITY IN FREE JET AND IMPINGEMENT REGIONS



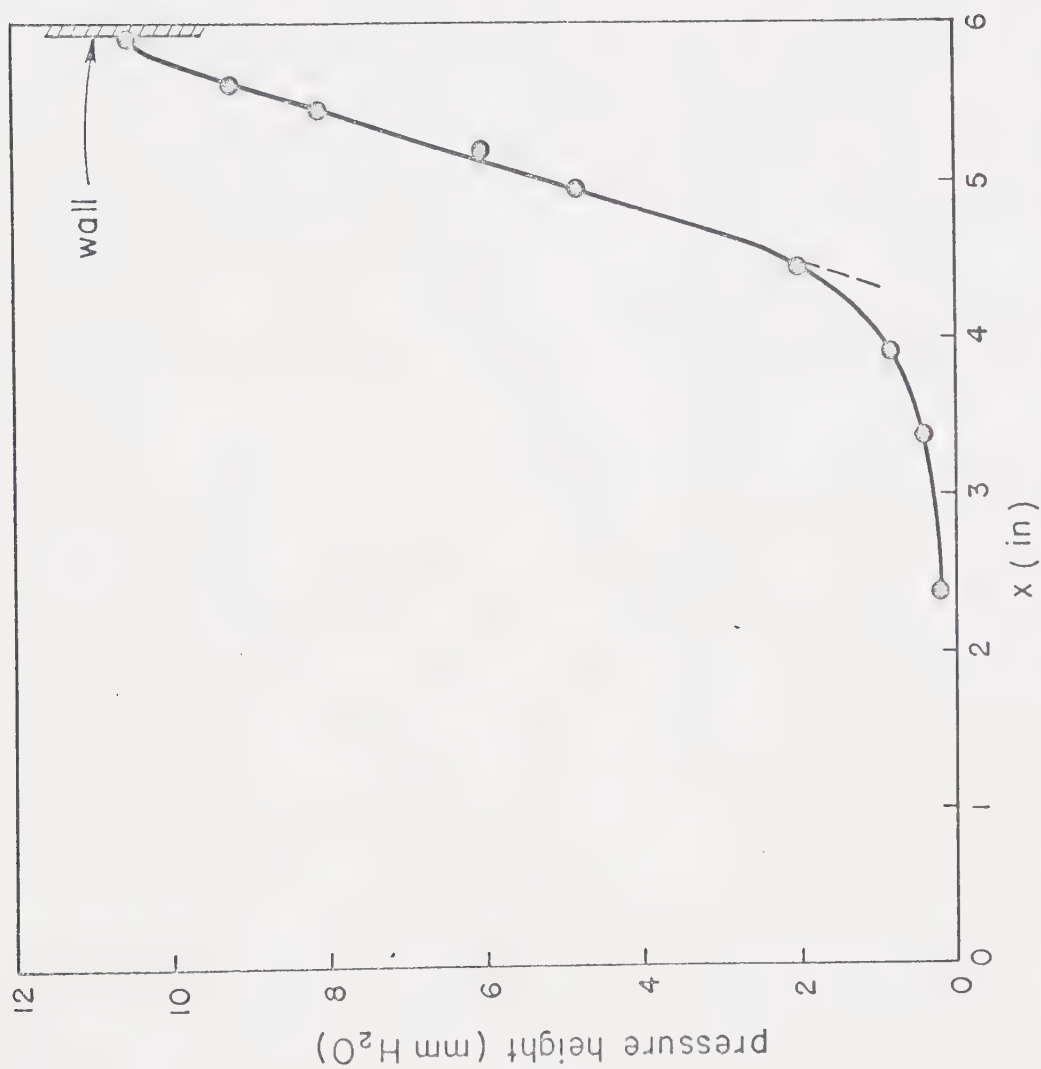


FIG. 2.25 AXIAL PRESSURE IN FREE JET AND IMPINGEMENT REGIONS [RUN NO. 1]



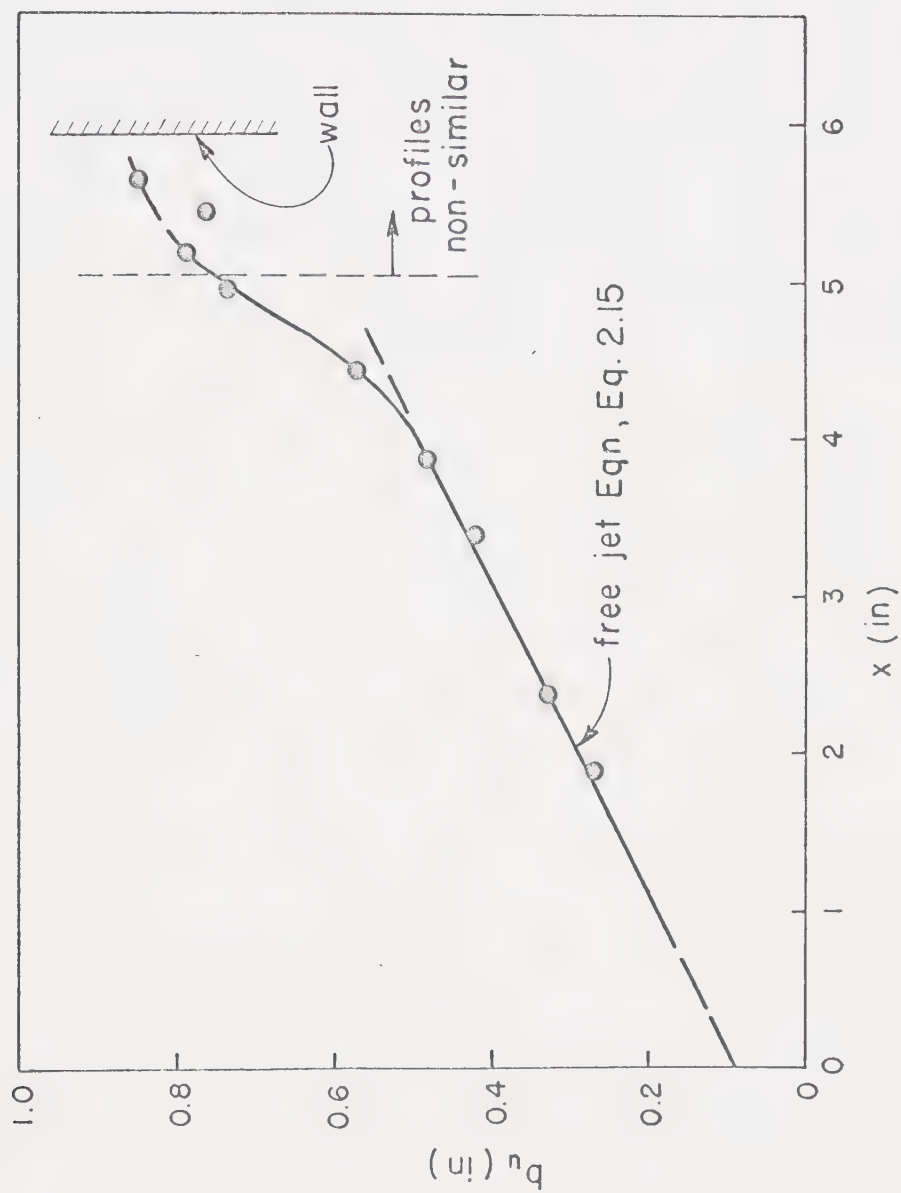


FIG. 2.26 LENGTH SCALE FOR VELOCITY IN FREE JET AND IMPINGEMENT REGIONS [RUN NO. I]



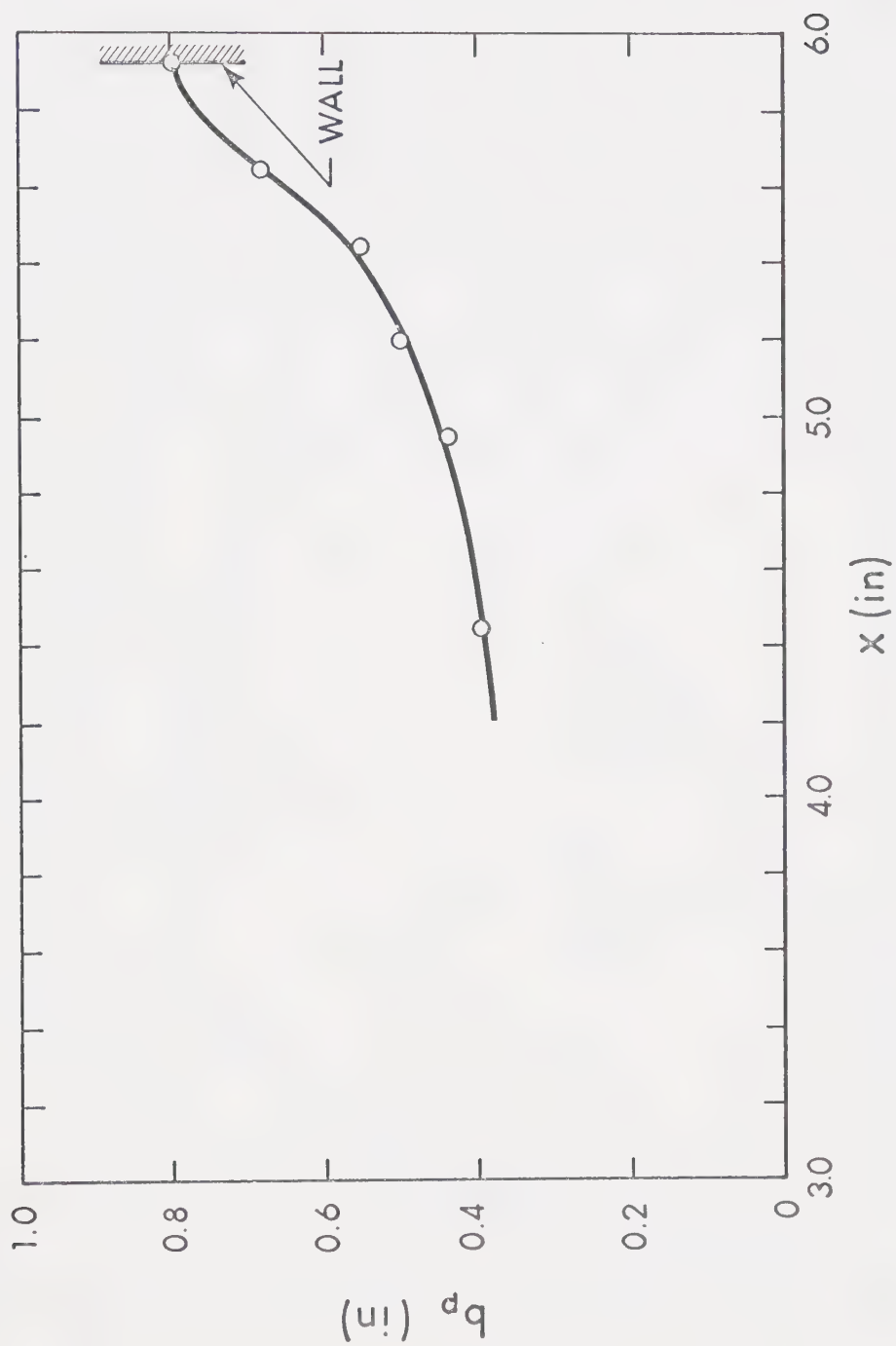


FIG. 2.27 LENGTH SCALE FOR PRESSURE IN IMPINGEMENT REGION [RUN NO.1]





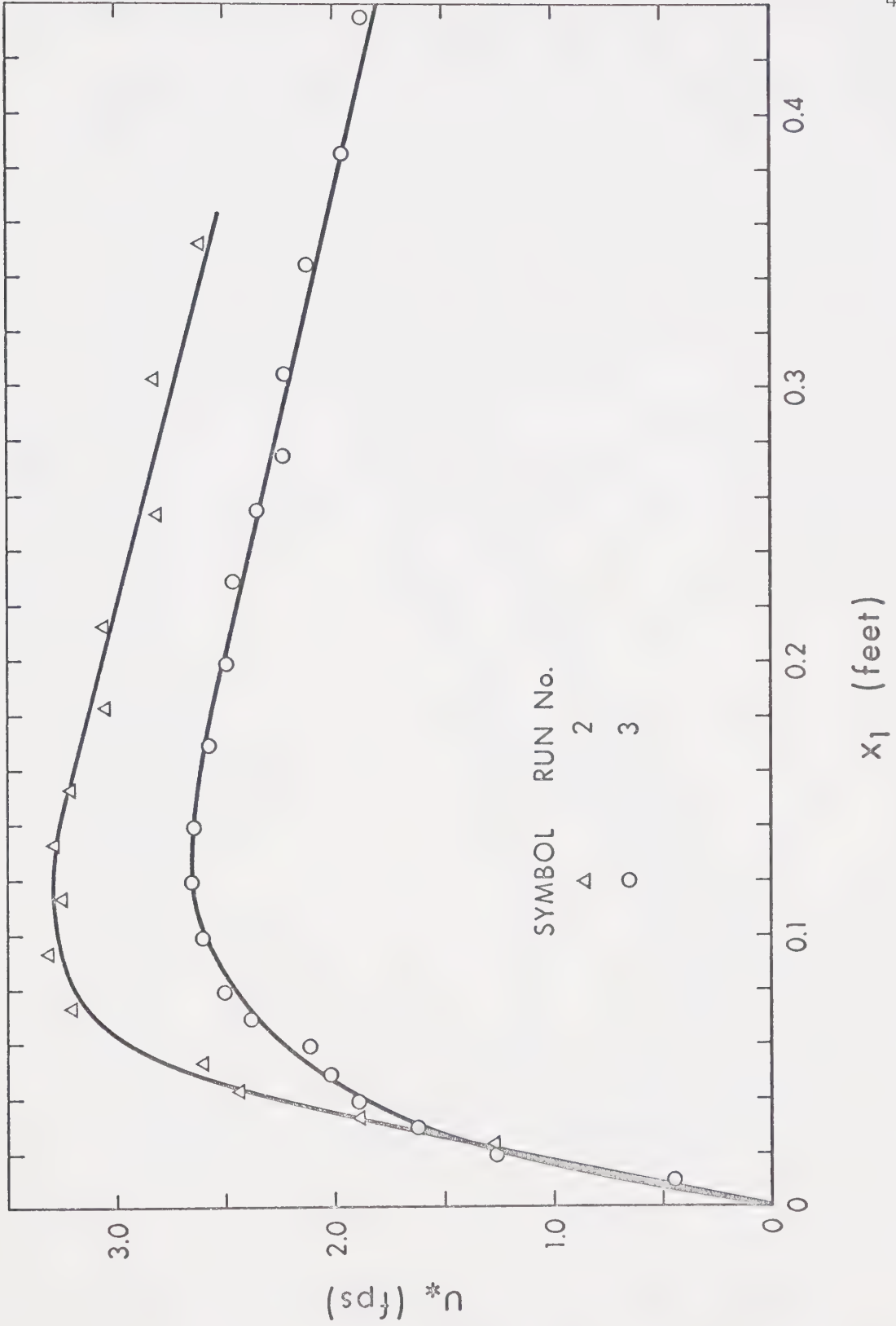


FIG. 2.28 SHEAR VELOCITY DISTRIBUTION IN IMPINGEMENT REGION



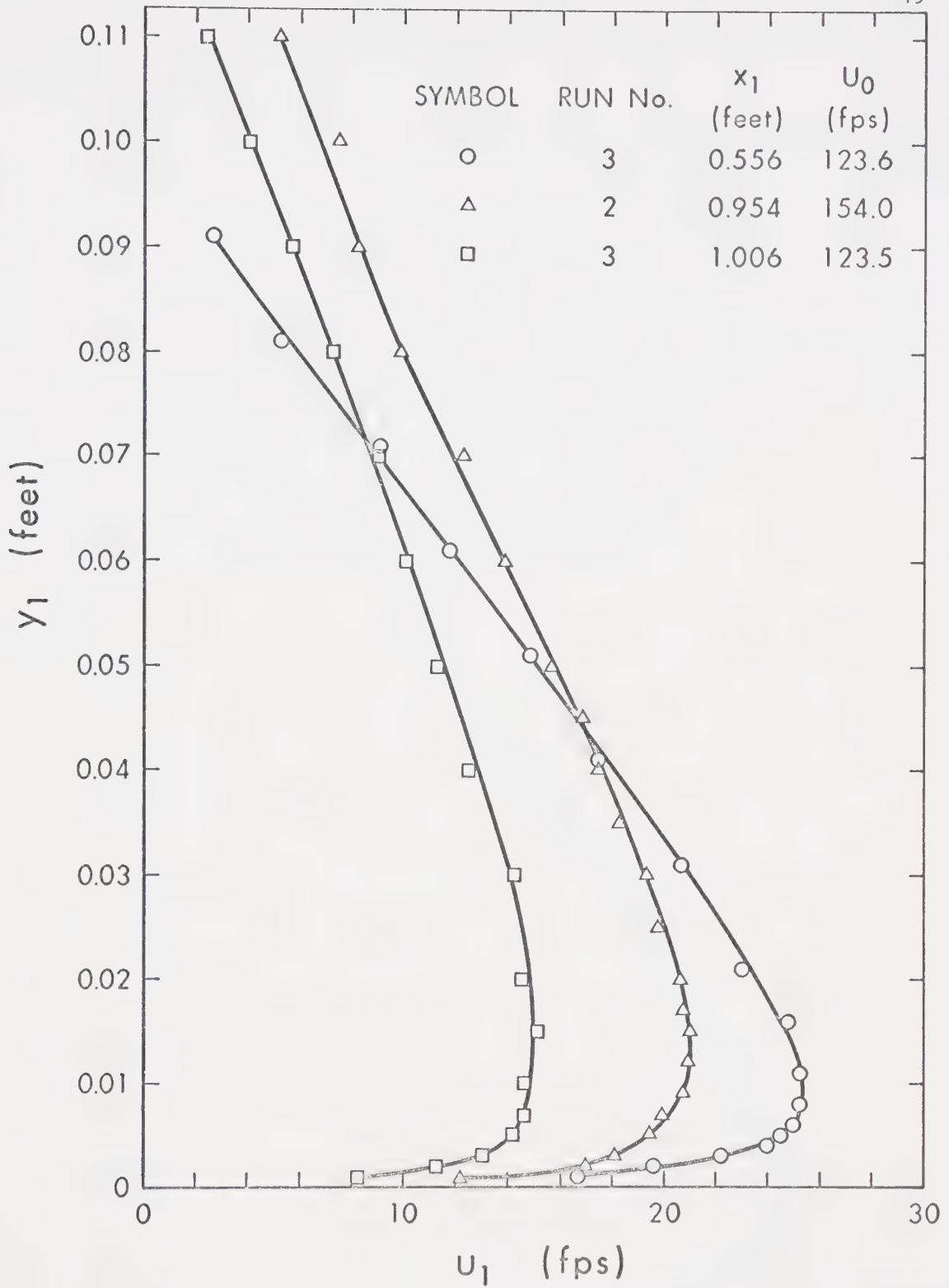


FIG. 2.29 TYPICAL VELOCITY PROFILES  
IN WALL JET



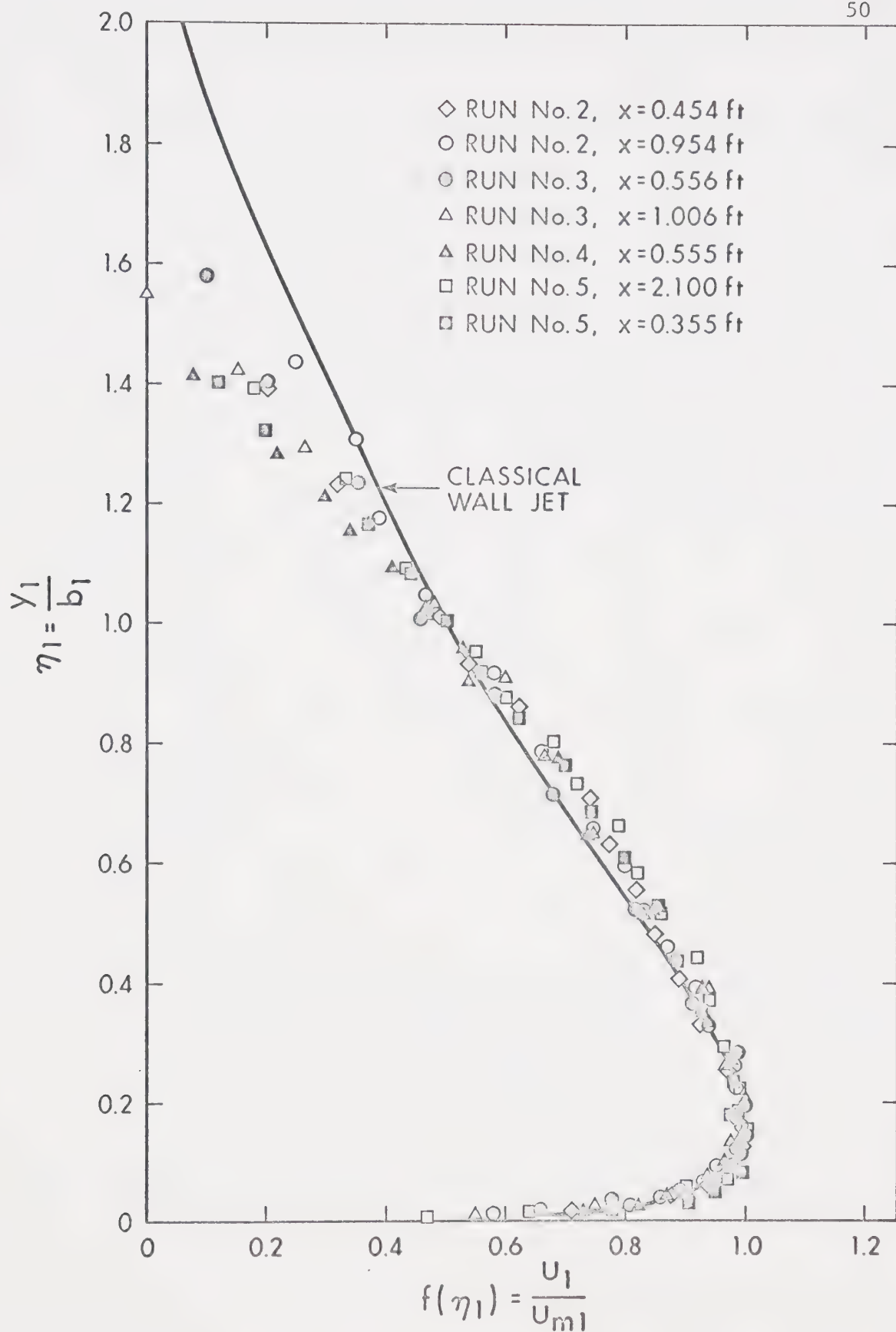


FIG. 2.30 DIMENSIONLESS VELOCITY DISTRIBUTION IN WALL JET



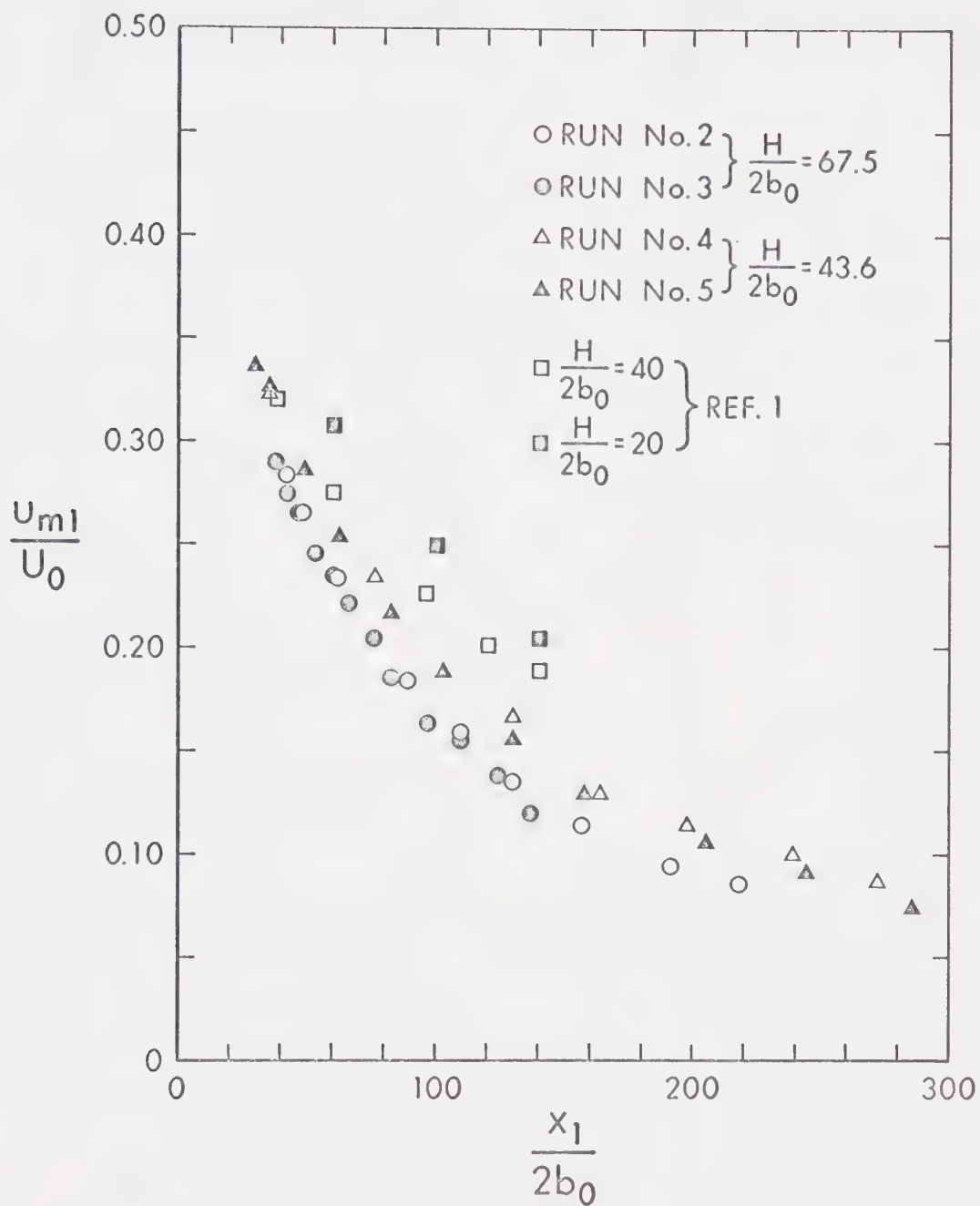


FIG. 2.32 MAXIMUM VELOCITY DECAY IN WALL JET





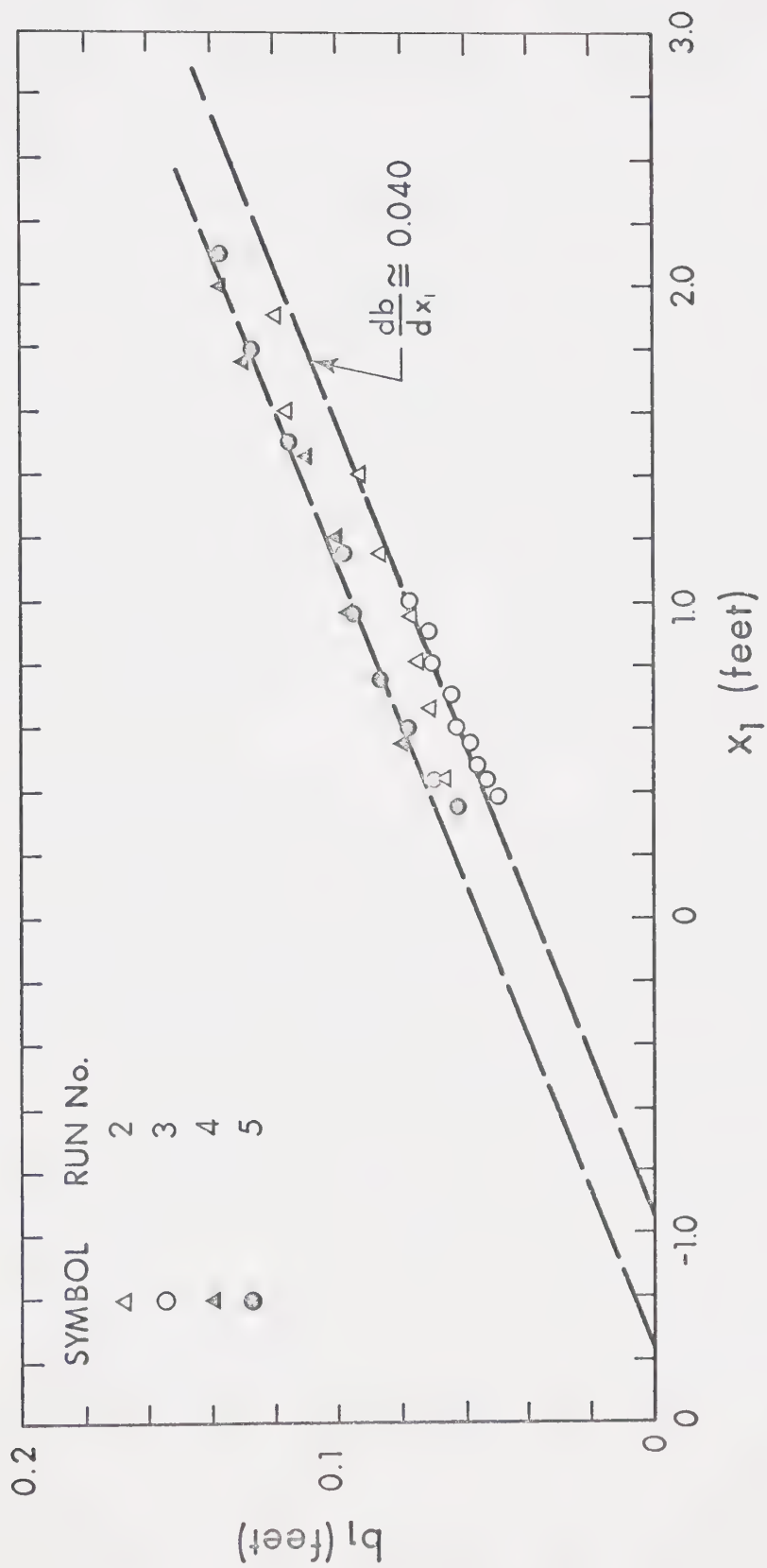


FIG. 2.33 LENGTH SCALE VARIATION IN WALL JET



## CHAPTER III

### ANALYSIS

This chapter is an attempt to produce a means of predicting different properties of the plane impinging jet with the aid of dimensional analysis and theoretical equations. Emphasis is placed on the study of the impingement region. Since a qualitative understanding of the problem precedes any analytical attempt, we propose to present briefly the various physical concepts involved.

#### 3.1 Physical Considerations

The flow from the nozzle enters a region in which the main properties of the jet vary almost identically with those of the corresponding free jet. Thus,  $u_m$  varies as  $x^{-1/2}$ ,  $b_u$  varies as  $x$ ,  $v \ll u$ , and the velocity profiles are similar for  $x$  greater than the length of the potential core. Therefore the effect of the wall in this region must be very small. This effect is transmitted by means of increased static pressures, hence the excess static pressures must be very small in comparison with dynamic pressures.

Downstream of this region the presence of the wall significantly alters the above characteristics. The flow is deflected and becomes parallel to the wall, so that ultimately it forms a wall jet. Between the free jet and the wall jet we have the impingement region.



The impingement region is characterized by a sharp increase in the static pressure, a fast decay of the vertical velocity component,  $u$ , and by the fact that the horizontal velocity component,  $v$ , is generally of the same order of magnitude as  $u$ . Quantitative definition of the limits of this region is arbitrary because it depends upon the particular criteria used in defining those limits. Two particular boundaries are of distinct interest in this case. One is the beginning of the region,  $x_0$ , which is the boundary between the free jet and impingement regions at the axis. The other is the end of the region along the wall, which could be defined as that distance  $x_{10}$  at which the pressure increase becomes very small.

If the subscript  $f$  is used to denote properties of the corresponding free jet, then  $x_0$  could arbitrarily be defined as that value of  $x$  at which;  $u_m = 0.98 u_{mf}$  or  $b_u = 1.02 b_{uf}$  or  $p_m = 0.05 p_s$ . The values of  $x_0$  defined thus may be expected to be close, they cannot, however, be expected to coincide.

The impingement region is characterized by reduced turbulence near the axis. This may be deduced from the results of previous investigations [2], [3], where it appears that the total head on the axis does not vary excessively between  $x = x_0$  and  $x = H$ . The flow is thus almost potential in the neighborhood of the stagnation point [3] and a flow pattern known as "stagnation flow" [10, p. 87], is likely to occur. Under these conditions, the boundary layer could be laminar for some distance from the stagnation point. Further



downstream along the wall, the flow becomes established as a wall jet. A transition between the end of the impingement region and the wall jet is likely to exist. The main difference between the wall jet after impingement and the classical plane wall jet, lies in the manner in which they are produced. The latter is produced by the efflux of momentum through a small opening. This situation closely approximates the idealization of a point source. However, the wall jet after impingement is produced by a pressure distribution on the axis and a favourable pressure gradient persisting for a certain distance downstream.

### 3.2 Dimensional Analysis

#### 3.2.1 Free Jet and Impingement Regions

For a plane, turbulent free jet, it has been proved both analytically and experimentally that:

$$u_{mf}, b_f = f_{1,2}(M_o, \rho, x) \quad (3.1)$$

where  $M_o = \rho \cdot 2b_o \cdot U_o^2$  = efflux of momentum. Equation 3.1 suggests that viscous effects are negligible and that the concept of a point source is valid.

Assuming that the above are valid in the case of an impinging jet also, we may write:





$$u_m, b = f_{3,4}(M_o, \rho, x, H) \quad (3.2)$$

$$p = f_5(M_o, \rho, H, x, y) \quad (3.3)$$

Applying the principles of dimensional analysis to Eqs. 3.2 and 3.3 we obtain:

$$\frac{u_m}{U_o} \sqrt{\frac{H}{2b_o}} = g_1\left(\frac{x}{H}\right) \quad (3.4)$$

$$\frac{b}{H} = g_2\left(\frac{x}{H}\right) \quad (3.5)$$

$$\frac{p}{\rho U_o^2/2} \frac{H}{2b_o} = g_3\left(\frac{x}{H}, \frac{y}{H}\right) \quad (3.6)$$

Eq. 3.1 gives:

$$\frac{u_{mf}}{U_o} \sqrt{\frac{x}{2b_o}} = C = \text{const.} \quad (3.7)$$

Dividing Eq. 3.4 by 3.7 we obtain:

$$\frac{u_m}{u_{mf}} = h\left(\frac{x}{H}\right) \quad (3.8)$$



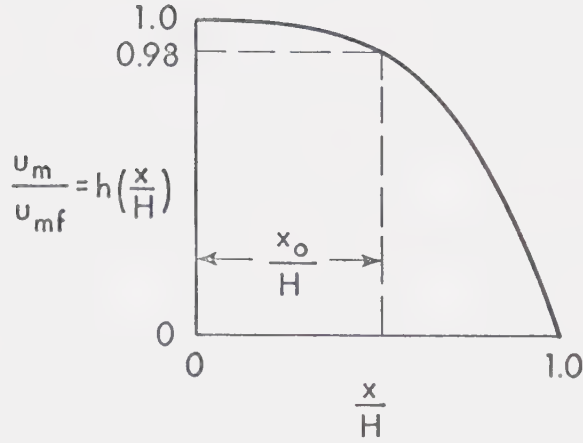


FIG. 3.1 SKETCH OF FUNCTION  $h\left(\frac{x}{H}\right)$

The function  $h\left(\frac{x}{H}\right)$  is schematically sketched in Fig. 3.1. If the beginning of the impingement region is defined to occur at a distance  $x_o$  at which  $u_m = 0.98 u_{mf}$ , then  $\frac{x_o}{H}$  is the solution of  $h\left(\frac{x_o}{H}\right) = 0.98$ . Therefore, the distance  $x_o$  is a fixed fraction of the impingement height,  $H$ . The experimental results are plotted in Fig. 3.2 which supports the arguments used in the dimensional analysis leading to Eq. 3.4.

Eq. 3.6 may be applied to the axis ( $y = 0$ ) to find the axial pressure,  $p_m$ .

$$\frac{p_m}{\rho U_o^2/2} \frac{H}{2b_o} = g_3\left(\frac{x}{H}, 0\right) = g_4\left(\frac{x}{H}\right) \quad (3.9)$$

The stagnation pressure  $p_s$ , will be:



$$\frac{p_s}{\rho U_o^2/2} \frac{H}{2b_o} = g_4(1) = \text{const.} \quad (3.10)$$

Dividing (3.9) with (3.10) we obtain:

$$\frac{p_m}{p_s} = g_5\left(\frac{x}{H}\right) \quad (3.11)$$

The experimental observations on pressure variation are plotted in Fig. 3.3 and the structure of Eq. 3.11 is well supported. Although the scatter is appreciable it is believed to be due to the number of computational steps involved in obtaining values of pressure, as well as to the difficulty of obtaining  $p_s$ .

The wall pressure distribution,  $p_w$ , may be obtained from Eq. 3.6 for  $x = H$ . Then:

$$\frac{p_w}{\rho U_o^2/2} \frac{H}{2b_o} = g_3\left(1, \frac{y}{H}\right) = g_6\left(\frac{y}{H}\right) \quad (3.12)$$

In Eq. 3.12,  $y$  is the distance along the wall from the stagnation point. It may therefore be substituted by  $x_1$  in the coordinate system  $x_1, y_1$ . Hence:

$$\frac{p_w}{\rho U_o^2/2} \frac{H}{2b_o} = g_6\left(\frac{x_1}{H}\right) \quad (3.13)$$

Dividing (3.13) with (3.10) we obtain



$$\frac{p_w}{p_s} = g_7 \left( \frac{x_1}{H} \right) \quad (3.14)$$

Equation 3.14 is verified in Fig. 3.4. The data suggest that the pressure vanishes when  $x_1 \approx 0.4H$ . However, even at  $\frac{x_1}{H} = 0.30$ , the pressure is only 5% of the stagnation pressure,  $p_s$ , and the gradient is very small. Hence, it is suggested that the end of the impingement region be taken as  $x_{10} = 0.3H$ .

We have seen already that the pressure profiles are similar in the impingement region. To check whether similarity extends to the wall we proceed as follows. The value of  $b_p$  at the wall,  $b_{pw}$ , is found from the data of Fig. 3.4 to be:

$$b_{pw} = 0.134H$$

The similarity curve for pressures is given by Eq. 2.12A:

$$p/p_m = f(\eta) = e^{-(0.834\eta)^2}, \quad \eta = \frac{y}{b_p}.$$

At the wall,  $\eta = \frac{y}{b_{pw}} = \frac{x_1}{0.134H} = 7.45 \left( \frac{x_1}{H} \right)$ . Thus, if the wall profile is similar to the profiles in the jet, the function:

$$\frac{p_w}{p_s} = e^{-(0.834 \times 7.45 \left( \frac{x_1}{H} \right))^2} \text{ should describe the data.}$$

After performing computations, this becomes:





$$\frac{p_w}{p_s} = e^{-38.5 \left(\frac{x_1}{H}\right)^2} \quad (3.15)$$

This is plotted in Fig. 3.4 and appears to be in good agreement with experimental results, hence supporting the statement that similarity extends to the wall.

In Eq. 3.5,  $b$  is an unspecified length scale. In the present case two length scales are involved, one for velocities,  $b_u$ , and one for pressures,  $b_p$ . Thus:

$$\frac{b_u}{H} = g_{2u} \left(\frac{x}{H}\right) \quad \text{and} \quad \frac{b_p}{H} = g_{2p} \left(\frac{x}{H}\right) \quad (3.16)$$

The experimental results are plotted in Figures 3.5 and 3.6, in the form suggested by Eqs. 3.16. Although there are no results for different heights and nozzle velocities to confirm (3.16), it is believed that these equations are valid because they are based on the same assumptions as Eqs. 3.4, 3.11 and 3.14 which were verified.

For the wall shear stress,  $\tau_o$ , and the horizontal velocity component,  $u_{m1}$ , at the edge of the boundary layer in the impingement region, we could also write:

$$u_{m1}, \tau_o = h_{1,2}(M_o, \rho, x_1, H)$$

or

$$\frac{u_{m1}}{U_o} \sqrt{\frac{H}{2b_o}} = h_3 \left(\frac{x_1}{H}\right) \quad (3.17A)$$

and



$$\frac{u_*}{U_o} \sqrt{\frac{H}{2b_o}} = h_4\left(\frac{x_1}{H}\right) \quad (3.17B)$$

The experimental data are plotted, as suggested in (3.17), in Figures 3.7 and 3.8. Although there is some scatter, it is believed that Eqs. 3.17 are valid with the possible exception of a small region near the stagnation point where the boundary layer is likely to be laminar.

In the impingement region the wall pressure gradient is appreciable, therefore, the reliability of shear stress data is subject to limitations.

Patel [13] suggests that in favourable pressure gradients, use of the Preston technique will produce errors not larger than 6% if the following conditions are satisfied;

$$(i) \quad 0 > \Delta > -0.007 \quad \text{or} \quad |\Delta| < 0.007$$

$$(ii) \quad \frac{u_* d}{\nu} \leq 200$$

$$(iii) \quad \frac{d\Delta}{dx} < 0$$

where  $\Delta \equiv \frac{\nu}{3} \frac{dp}{dx}$ ,  $d$  = external tube diameter. These criteria are rough guides rather than absolute restrictions.

Condition (i) was derived empirically with the aid of fence readings. Condition (ii) is imposed to ensure that the tube is located in the region of wall similarity. Condition (iii) is imposed to ensure that the flow is not subjected to relaminarization. In the present case, the only physically plausible sequence of different flow



regimes is firstly laminar and later turbulent. If the boundary layer is laminar this must happen at the early stages of its development. Any sequence therefore, that includes laminar reversion in the direction of flow is physically unacceptable.

Using Eqs.3.17B and 3.15 we find, after some manipulations, that:

$$|\Delta| \approx \frac{285}{R_H} \frac{\xi_1 e^{-38.5\xi_1^2}}{(h_4(\xi_1))^3}$$

where

$$\xi_1 = \frac{x_1}{H} \quad \text{and} \quad R_H = \frac{2U_o b_o}{\nu} \sqrt{\frac{H}{2b_o}} = R_o \sqrt{\frac{H}{2b_o}}$$

For condition (i) to be satisfied:

$$\frac{\xi_1 e^{-38.5\xi_1^2}}{(h_4(\xi_1))^3} \leq 0.0246 \left(\frac{R_H}{10^3}\right) \quad (3.18)$$

For the present set of experiments, (3.18) is satisfied for  $\xi_1 \geq 0.325$ , whereas for the results of [1] it is satisfied for  $\xi_1 \geq 0.225$ .

Since the present results are in agreement with those of [1], this limit may be extended to  $\xi_1 = 0.225$ . For values of  $\frac{x_1}{H} \leq 0.225$  the results are likely to involve an error larger than about 6%.

The maximum value of  $\frac{u_* d}{\nu}$  in the present experiments was about 140, hence condition (ii) is satisfied.



### 3.2.2 Wall Jet Region

Considering the region where the flow is established to similarity, a first approximation is obtained if, in spite of the wall shear,  $\tau_0$ , the momentum is assumed to be preserved. That is to say the frictional force is small compared with the momentum flux involved.

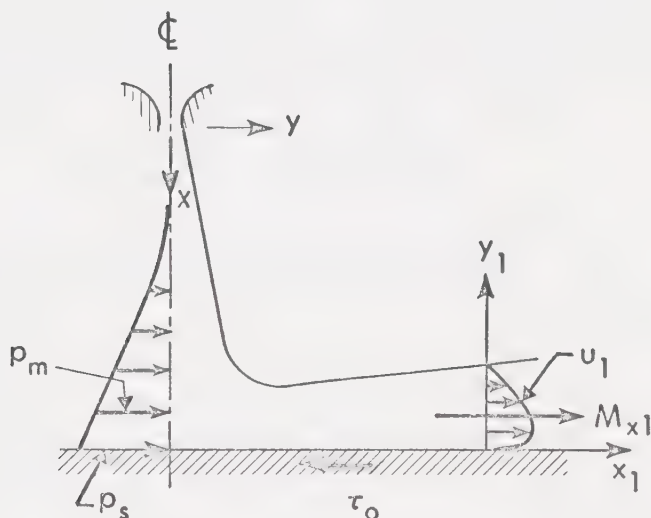


FIG. 3.9 SKETCH OF MOMENTUM BALANCE

With reference to Fig. 3.9, the momentum equation in the  $x_1$  direction will give (neglecting  $\tau_0$ ):

$$M_{x1} = \int_0^{\infty} \rho u_1^2 dy_1 = \int_0^H P_m dx$$





Thus,  $M_{x1}$  is "preserved". On this basis, we could write:

$$u_{m1} = \psi_1(M_{x1}, \rho, \nu, x_1) \quad (3.19)$$

But

$$M_{x1} = \int_0^H p_m dx = H p_s \int_0^1 \frac{p_m}{p_s} d\left(\frac{x}{H}\right)$$

or, from Eq. 3.11,  $M_{x1} = \text{const. } p_s H$ . But, by Eq. 3.10:

$$p_s = \rho \frac{U_o^2}{2} \frac{2b_o}{H} \cdot \text{const.},$$

hence

$$M_{x1} = \text{const.} \cdot \rho U_o^2 \cdot 2b_o = \text{const. } M_o$$

Therefore:

$$u_{m1} = \psi_2(\rho U_o^2 \cdot 2b_o, \rho, x_1)$$

neglecting viscous effects. Hence:

$$\frac{u_{m1}}{U_o} = \frac{\text{const}}{\sqrt{x_1/2b_o}} \quad (3.20)$$

Eq. 3.20 will hold approximately if the shear stress is relatively small. It is interesting to note that this equation is independent of  $H$ . Eq. 3.20 may also be written as:



$$\frac{u_{m1}}{U_o} \sqrt{\frac{H}{2b_o}} = \frac{\text{const}}{\sqrt{x_1}/H} \quad (3.21)$$

The data are plotted in this form in Fig. 3.10, along with the results of [1] . Eq. 3.21 and therefore Eq. 3.20 describe the data for a certain distance  $\frac{x_1}{H}$  , beyond which the exponent of  $x_1$  appears to differ from  $-\frac{1}{2}$  . This value of  $\frac{x_1}{H}$  obviously depends upon the relative magnitude of  $\tau_o$  . From the above, we conclude that a more general statement of the problem is necessary, as follows:

$$u_{m1} = \psi_3(U_o, 2b_o, \rho, \nu, H, x_1)$$

or

$$\frac{u_{m1}}{U_o} = \psi_4(R_o, \frac{H}{2b_o}, \frac{x_1}{2b_o}) \quad (3.22)$$

where

$$R_o = \frac{2U_o b_o}{\nu} .$$

Similarly, we may deduce that:

$$\frac{b_1}{2b_o} = \psi_5(R_o, \frac{H}{2b_o}, \frac{x_1}{2b_o}) \quad (3.23)$$



### 3.3 Theoretical Development

#### 3.3.1 Free Jet Region

We have seen in the previous chapter that (Eq. 2.14):

$$\frac{u_m}{U_o} = \frac{2.40}{\sqrt{\frac{x}{2b_o} - 2.5}}$$

To make this equation compatible with Eq. 3.4 which is a result of dimensional analysis, multiply with  $\sqrt{\frac{H}{2b_o}}$ . Then:

$$\frac{u_m}{U_o} \sqrt{\frac{H}{2b_o}} = \frac{2.40}{\sqrt{\frac{x}{H} - \frac{2.5}{H/2b_o}}}$$

The quantity  $\frac{2.5}{H/2b_o}$  is a virtual origin correction and generally small in comparison with  $\frac{x}{H}$ . Thus, the above Equation may be rewritten as:

$$\frac{u_m}{U_o} \sqrt{\frac{H}{2b_o}} = \frac{2.40 C_1}{\sqrt{\frac{x}{H}}}$$

where  $C_1$  is an adjustment coefficient. The present data indicate a value of  $C_1 \approx 1.04$ , hence:



$$\frac{u_m}{U_o} \sqrt{\frac{H}{2b_o}} = \frac{2.50}{\sqrt{\frac{x}{H}}} \quad (3.24)$$

This is verified in Fig. 3.2, and is valid for  $\frac{x}{H} \leq 0.65$ . The length scale for velocities is given by:

$$\frac{b_u}{H} = 0.10 \left( \frac{x}{H} + 0.15 \right) \text{ for } \frac{x}{H} \leq 0.65$$

The pressure  $p_m$  is very small in this region. The velocity field may be predicted by means of the similarity curve and the scales  $b_u$  and  $u_m$ .

### 3.3.2 Impingement Region

An approximate analysis can be carried out for the decay of  $u_m$  as shown below.

Assuming that  $uv$  is independent of  $x$  at small values of  $y$  (see Fig. 2.20), we could write:

$$\left( \frac{\partial uv}{\partial y} \right)_{y \rightarrow 0} = k \quad (3.25)$$

where  $k$  is a constant. But,

$$\frac{\partial uv}{\partial y} = u \frac{\partial v}{\partial y} + v \frac{\partial u}{\partial y} = -u \frac{\partial u}{\partial x} + v \frac{\partial u}{\partial y}$$





(using the continuity equation,  $\frac{\partial u}{\partial x} + \frac{\partial v}{\partial y} = 0$ ). Therefore:

$$\left(\frac{\partial uv}{\partial y}\right)_{y=0} = k = - \left(u \frac{\partial u}{\partial x}\right)_{y=0},$$

since  $(v)_{y=0} = 0$ . But,

$$\left(u \frac{\partial u}{\partial x}\right)_{y=0} = u_m \frac{du_m}{dx} = \frac{1}{2} \frac{d}{dx} (u_m^2),$$

hence,

$$\frac{d}{dx} (u_m^2) = -2k$$

or,

$$u_m^2 = -2kx + k_1,$$

where  $k_1$  is another constant. Using Eq. 3.4 we may write:

$$\left(\frac{u_m}{U_o}\right)^2 \frac{H}{2b_o} = k_3 \frac{x}{H} + k_4$$

or,

$$\left(\frac{u}{U_o}\right)^2 \frac{H}{2b_o} = k_5^2 \left(1 - \frac{x}{H}\right) + k_6 \quad (3.26)$$

This is verified in Fig. 3.11, where the constants are found to be

$k_5 \approx 5.50$  and  $k_6 \approx 0$ . Hence:



$$\frac{u_m}{U_o} \sqrt{\frac{H}{2b_o}} = 5.50 \sqrt{1 - \frac{x}{H}} \quad (3.26A)$$

This equation is plotted in Fig. 3.2. It is seen that the unique function indicated in Eq. 3.4 may be approximated by two different laws. Between  $\frac{x}{H} = 0.65$  and  $\frac{x}{H} = 0.75$  a smooth transition exists. However, neglect of this transition results in only small errors. For practical purposes, the boundary between the free jet and impingement region may be defined as the intersection of Eqs. 3.24 and 3.26A, which yields  $\frac{x_o}{H} \cong 0.70$ .\*

The maximum stagnation pressure on the wall,  $p_s$ , may be predicted as follows. Applying the momentum theorem between the nozzle and the wall, we have (neglecting shear stresses):

$$\rho U_o^2 2b_o = 2 \int_0^\infty p_w dx_1$$

or

$$2 p_s H \int_0^\infty \left( \frac{p_w}{p_s} \right) d \left( \frac{x_1}{H} \right) = \rho U_o^2 2b_o .$$

Let

$$\int_0^\infty \left( \frac{p_w}{p_s} \right) d \left( \frac{x_1}{H} \right) = K_{pw}$$

---

\* A similar analysis was carried out for the case of circular impinging jets and was found to be in good agreement with the experimental results reported in [2] .



Then,

$$\frac{P_s}{\rho U_o^2/2} \frac{H}{2b_o} = \frac{1}{K_{pw}} \quad (3.27)$$

The constant  $K_{pw}$  is found (using Eq. 3.15) to be 0.143. The average value of  $K_{pw}$  by direct measurement was found to be 0.127. It appears that the integral tends to overestimate the value of  $K_{pw}$ , hence it is suggested that  $K_{pw}$  be taken equal to 0.130. The maximum discrepancy would then be about 10%. This is attributed to the difficulty of measuring wall pressure distributions precisely and in possible non-uniformity of the nozzle mouth. Using  $K_{pw} = 0.13$ , Eq. 3.27 reads:

$$\frac{P_s}{\rho U_o^2/2} \frac{H}{2b_o} = 7.7 \quad (3.28)$$

To predict the axial pressure,  $p_m$ , the variation of the total pressure,  $P_T$ , on the axis is studied first. This is done, because if turbulence is reduced in the impingement region, then the total pressure will not vary excessively and with reference to Fig. 3.12, it might be possible to approximate it by a straight line. Knowing  $u_m$ , the variation of  $p_m$  could be found by subtraction.

We have:

$$P_T = p_m + \frac{\rho u_m^2}{2}$$

To make this dimensionless, divide with  $p_s$  :



$$\frac{p_T}{p_s} = \frac{p_m}{p_s} + \frac{\rho u_m^2}{2p_s} \quad (3.29)$$

But,

$$p_s = \frac{\rho U_o^2}{2} \left( \frac{2b_o}{H} \right) \frac{1}{K_{pw}}$$

by Eq. 3.27. Substituting in (3.29) we have:

$$\frac{p_T}{p_s} = \frac{p_m}{p_s} + K_{pw} \left( \frac{u_m}{U_o} \sqrt{\frac{H}{2b_o}} \right)^2 \quad (3.30)$$

The data are plotted in this form in Fig. 3.12, where  $p_T$  is seen to vary mildly with  $x$  and the straight line:

$$\frac{p_T}{p_s} = 1.73 - 0.73 \frac{x}{H} \quad (3.31)$$

appears to be a reasonable approximation.

From Eq. 3.30 the axial pressure,  $p_m$ , is found as

$$\frac{p_m}{p_s} = \frac{p_T}{p_s} - K_{pw} \left[ \frac{u_m}{U_o} \sqrt{\frac{H}{2b_o}} \right]^2$$

or, by Eqs. 3.26A, 3.27 and 3.28:





$$\frac{p_m}{p_s} = 3.2 \frac{x}{H} - 2.2 \quad (3.32)$$

This is plotted in Fig. 3.3 and appears to be a reasonable description of the data for  $\frac{x}{H} \gtrsim 0.75$ .

Equations 3.26 and 3.32 cannot be expected to hold in a region very near the stagnation point, where the flow may approximate a potential pattern. However, the data indicate that such region is very small.

With the information already available it is now possible to derive generalized equal-pressure contours. Let any contour value be  $n = \frac{p}{p_s}$ . By Eqs. 2.12A and 3.11:

$$n = \frac{p}{p_s} = \frac{p}{p_m} \frac{p_m}{p_s} = e^{-(k\eta)^2} g_5(\xi)$$

where

$$\eta = \frac{y}{b_p}, \quad k = 0.834, \quad \xi = \frac{x}{H}$$

Taking logarithms:

$$\ln n = -k^2 \eta^2 + \ln g_5(\xi)$$

or

$$\eta = \frac{1}{k} \sqrt{\ln g_5 - \ln n} = \frac{1}{k} \left[ \ln \frac{g_5(\xi)}{n} \right]^{1/2}$$

But,



$$\eta = \frac{y}{b_p} = \frac{y}{H} \frac{H}{b_p} ,$$

hence

$$\frac{y}{H} = \frac{1}{k} \left( \frac{b_p}{H} \right) \sqrt{\ln \frac{g_5(\xi)}{n}}$$

By Eq. 3.16,

$$\frac{b_p}{H} = g_{2p}(\xi) ,$$

therefore

$$\frac{y}{H} = \frac{1}{k} g_{2p}(\xi) \sqrt{\ln \frac{g_5(\xi)}{n}}$$

In general:

$$\frac{y}{H} = F\left(n, \frac{x}{H}\right) \quad (3.33)$$

Some contours are shown in Fig. 3.13.

The variation of the maximum horizontal velocity component,  $u_{m1}$ , along the wall may be found by assuming the flow to be potential immediately outside the boundary layer. By the Bernoulli theorem:

$$\frac{\rho u_{m1}^2}{2} + p_w = p_s ,$$

or



$$\frac{\rho U_{m1}^2}{2p_s} + \frac{p_w}{p_s} = 1 \quad .$$

Using Eqs. 3.28 and 3.15 and after some manipulations, we find:

$$\frac{u_{m1}}{U_o} \sqrt{\frac{H}{2b_o}} = 2.77 \left\{ 1 - e^{-38.5 \left(\frac{x_1}{H}\right)^2} \right\}^{1/2} \quad (3.34)$$

In Fig. 3.7, Equation 3.34 is seen to describe the data reasonably well, for values of  $\frac{x_1}{H} \leq 0.4$ . Beyond this value, the decelerating effect of entrainment becomes appreciable and  $u_{m1}$  decays steadily to assume wall jet variation further downstream.

The wall shear stress,  $\tau_o$ , is found as follows. The equation of motion in the  $x$ -direction for plane flow is:

$$u \frac{\partial u}{\partial x} + v \frac{\partial u}{\partial y} = -\frac{1}{\rho} \frac{\partial p}{\partial x} + \frac{1}{\rho} \frac{\partial \tau}{\partial y} \quad (3.35)$$

where  $\tau$  is the total shear stress constituting of both laminar and turbulent shear stresses, and  $u, v, p$  are time average quantities. On the wall, this equation reduces to:

$$0 = -\frac{1}{\rho} \frac{\partial p}{\partial x} \Big|_{x=H} + \frac{1}{\rho} \frac{\partial \tau}{\partial y} \Big|_{x=H} \quad ,$$

or

$$\left(\frac{\partial \tau}{\partial y}\right)_{x=H} = \left(\frac{\partial p}{\partial x}\right)_{x=H}$$



But  $\left(\frac{\partial \tau}{\partial y}\right)_{x=H} = \frac{d\tau_0}{dx_1}$ , where  $x_1$  is referred to the coordinate system  $x_1, y_1$  and denotes distance from the stagnation point along the wall. Hence:

$$\tau_0 = \int_0^{x_1} \left(\frac{\partial p}{\partial x}\right)_{x=H} dx_1 \quad (3.36)$$

Due to similarity (Eq. 2.12A):  $p = p_m f(\eta)$ , where  $f(\eta) = e^{-k\eta^2}$ ,  
 $k = 0.693$ ,  $\eta = \frac{y}{b_p}$ .

$$\frac{\partial p}{\partial x} = f(\eta) \frac{dp_m}{dx} + p_m \frac{df}{d\eta} \frac{\partial \eta}{\partial x}$$

But

$$\frac{\partial \eta}{\partial x} = -\frac{y}{b_p^2} \frac{db_p}{dx} = -\eta \frac{1}{b_p} \frac{db_p}{dx}.$$

Thus,

$$\frac{\partial p}{\partial x} = f \frac{dp_m}{dx} - \frac{p_m}{b_p} \frac{db_p}{dx} \eta \frac{df}{d\eta}$$

and

$$\left(\frac{\partial p}{\partial x}\right)_{x=H} = f \left(\frac{dp_m}{dx}\right)_H - \frac{p_s}{(b_p)_H} \left(\frac{db_p}{dx}\right)_H \eta \frac{df}{d\eta}$$

The experimental data (Fig. 3.6) indicate that  $\left(\frac{db_p}{dx}\right)_H = 0$ . Using this observation we have:





$$\left(\frac{\partial p}{\partial x}\right)_H = f(\eta) \left(\frac{dp_m}{dx}\right)_H,$$

Thus,

$$\tau_o = \int_0^{x_1} f(\eta) \left(\frac{dp_m}{dx}\right)_H dx_1$$

or

$$\tau_o = \left(\frac{dp_m}{dx}\right)_H \int_0^{x_1} f(\eta) dx_1$$

At the wall;  $\eta = \frac{x_1}{b_{pw}}$ ,  $b_{pw} = (b_p)_H = 0.134H$ . Hence:

$$\tau_o = \left(\frac{dp_m}{dx}\right)_H b_{pw} \int_0^{\eta} f(\eta) d\eta \quad (3.37)$$

But, from Eq. 3.11,  $p_m = p_s g_5\left(\frac{x}{H}\right)$ , and therefore:

$$\frac{dp_m}{dx} = p_s g'_5\left(\frac{x}{H}\right) \frac{1}{H}.$$

By Eq. 3.27:

$$\frac{dp_m}{dx} = \frac{1}{K_{pw}} \frac{\rho U_o^2}{2} \frac{2b_o}{H} \frac{1}{H} g'_5\left(\frac{x}{H}\right),$$

hence:



$$\left(\frac{dp_m}{dx}\right)_H = \frac{1}{K_{pw}} \frac{\rho U_o^2}{2} \frac{2b_o}{H} \frac{1}{H} g'_5(1) \quad (1)$$

The quantity  $g'_5(1)$  is a constant, however, the available experimental data do not extend to the wall and it cannot be evaluated before hand. Let:

$$g'_5(1) = C_p$$

Then,

$$\left(\frac{dp_m}{dx}\right)_H = \frac{C_p}{K_{pw}} \frac{\rho U_o^2}{2} \frac{2b_o}{H} \frac{1}{H}$$

Substituting in (3.37) we find:

$$\tau_o = \frac{C_p}{K_{pw}} \frac{\rho U_o^2}{2} \frac{2b_o}{H} \left(\frac{b_{pw}}{H}\right) \int_0^\eta f(\eta) d\eta$$

or,

$$\frac{\tau_o}{\rho U_o^2/2} \frac{H}{2b_o} = 0.134 \frac{C_p}{K_{pw}} \int_0^\eta f(\eta) d\eta$$

or,

$$2\left(\frac{u_*}{U_o}\right)^2 \frac{H}{2b_o} = 0.134 \frac{C_p}{K_{pw}} \int_0^\eta f(\eta) d\eta \quad (3.38)$$

But,



$$\begin{aligned} \int_0^{\eta} f(\eta) d\eta &= \int_0^{\eta} e^{-k\eta^2} d\eta = \frac{1}{\sqrt{k}} \int_0^{\eta} e^{-(\sqrt{k}\eta)^2} d(\sqrt{k}\eta) \\ &= \frac{1}{\sqrt{k}} \frac{\sqrt{\pi}}{2} \frac{2}{\sqrt{\pi}} \int_0^{\sqrt{k}\eta} e^{-z^2} dz, \end{aligned}$$

where  $z$  is a dummy variable.

$$\text{Letting } I_p(\sqrt{k}\eta) = \frac{2}{\sqrt{\pi}} \int_0^{\sqrt{k}\eta} e^{-z^2} dz \quad \text{we recognize } I_p$$

to be the probability integral. Values of  $I_p$  may be obtained from any tables of functions. Substituting in (3.38) we obtain:

$$2 \left( \frac{u_*}{U_o} \right)^2 \frac{H}{2b_o} = 0.134 \frac{C_p}{K_{pw}} \frac{1}{2} \sqrt{\frac{\pi}{k}} I_p(\sqrt{k}\eta)$$

or,

$$\frac{u_*}{U_o} \sqrt{\frac{H}{2b_o}} = \left\{ \frac{0.134}{4} \frac{C_p}{K_{pw}} \sqrt{\frac{\pi}{k}} \right\}^{1/2} \cdot I_p(\sqrt{k}\eta)$$

Letting

$$C_1 = \left\{ \frac{0.134}{4} \frac{C_p}{K_{pw}} \sqrt{\frac{\pi}{k}} \right\}^{1/2}$$

we have finally:

$$\frac{u_*}{U_o} \sqrt{\frac{H}{2b_o}} = C_1 \sqrt{I_p(\sqrt{k}\eta)} \quad (3.39)$$

The value of  $C_1$  is evaluated from the shear stress data to



be equal to 0.17. With  $k = 0.693$  and

$$\eta = \frac{1}{0.134} \frac{x_1}{H} ,$$

we obtain:

$$\frac{u_*}{U_o} \sqrt{\frac{H}{2b_o}} = 0.17 \sqrt{I_p \left(6.2 \frac{x_1}{H}\right)} \quad (3.40)$$

Eq. 3.40 is plotted in Fig. 3.8 where it is seen to describe the data reasonably well, for values of  $\frac{x_1}{H}$  less than 0.4. Beyond this point the normal pressure gradient cannot be predicted by similarity considerations. From (3.40) we find:

$$\frac{\tau_o}{\rho U_o^2/2} \frac{H}{2b_o} = 0.058 I_p \left(6.2 \frac{x_1}{H}\right) \quad (3.41)$$

The value 0.17 for  $C_1$  indicates that  $C_p \approx 0.053$ . That is to say the axial pressure gradient at the wall is very small, owing to occurrence of nearly potential flow at the neighborhood of the stagnation point.

### 3.3.3 Wall Jet Region

After a certain distance downstream of impingement, the flow becomes established, so that the velocity distributions at different  $x_1$  stations may be reduced to a single similarity curve (Fig. 2.30):





$$\frac{u_1}{u_{m1}} = f(\eta_1) \quad , \quad \eta_1 = \frac{y_1}{b_1} \quad ,$$

where  $b_1$  is the value of  $y_1$  at which:

$$u_1 = \frac{1}{2} u_{m1} \quad \text{and} \quad \frac{\partial u_1}{\partial y_1} < 0 \quad .$$

The Reynolds equations, after the usual boundary layer approximations read (plane turbulent flow):

$$u_1 \frac{\partial u_1}{\partial x_1} + v_1 \frac{\partial u_1}{\partial y_1} = - \frac{1}{\rho} \frac{\partial p_1}{\partial x_1} + \frac{1}{\rho} \frac{\partial \tau_1}{\partial y_1} \quad (3.42)$$

$$\frac{\partial u_1}{\partial x_1} + \frac{\partial v_1}{\partial y_1} = 0 \quad (3.43)$$

where  $\tau_1 = - \overline{\rho u'_1 v'_1}$  and  $u'_1, v'_1$  are the fluctuating components of velocity.

$u_1, v_1, p_1$  are time average quantities.

The pressure  $p_1$  is very nearly atmospheric throughout the jet, hence  $\frac{\partial p_1}{\partial x_1} \approx 0$ . Therefore:

$$u_1 \frac{\partial u_1}{\partial x_1} + v_1 \frac{\partial u_1}{\partial y_1} = \frac{1}{\rho} \frac{\partial \tau_1}{\partial y_1} \quad (3.44)$$

Due to similarity;  $u_1 = u_{m1} f(\eta_1)$ . Assuming that the shear stress profiles may be made similar by means of the maximum dynamic pressure,



we could write:

$$\tau_1 = \rho u_{m1}^2 g(\eta_1)$$

Substituting the similarity expressions in Eqs. 3.43 and 3.44 we obtain after some manipulations:

$$\frac{b_1}{u_{m1}} \frac{du_{m1}}{dx_1} G_1(\eta_1) + \frac{db_1}{dx_1} G_2(\eta_1) = \frac{dg}{d\eta_1} \quad (3.45)$$

where  $G_1$ ,  $G_2$  are functions of  $\eta_1$  only. Since the variables  $x_1$ ,  $\eta_1$  are formally independent:

$$\frac{db_1}{dx_1} = \text{const} \quad (3.46)$$

$$\frac{b_1}{u_{m1}} \frac{du_{m1}}{dx_1} = \text{const} \quad (3.47)$$

Eq. 3.46 yields:

$$b_1 = C_b \bar{x}_1 \quad (3.48)$$

where  $C_b$  is a constant and  $\bar{x}_1$  is measured from a virtual origin for the length scale  $b_1$ .

The linearity of  $b_1$  is verified in Fig. 2.33. The value



of  $C_b$  is 0.04. Thus:

$$\frac{b_1}{2b_o} = C_b \frac{x_1}{2b_o} + C_1 .$$

Recalling Eq. 3.23, we deduce that

$$C_b = C_b \left( \frac{H}{2b_o}, R_o \right) \quad \text{and} \quad C_1 = C_1 \left( \frac{H}{2b_o}, R_o \right)$$

The present results suggest that  $C_b$  does not depend on  $\frac{H}{2b_o}$ . This is also supported by the results of [1]. However, the value of  $C_b$  from [1] is 0.10, which indicates that

$$C_b = C_b(R_o) \quad \text{and} \quad \frac{dC_b}{dR_o} > 0 \quad (3.49)$$

Using Eq. 3.47, we find:

$$u_{m1} = k \bar{x}_1^a \quad (3.50)$$

where  $k, a$  are constants.

Returning to Eq. 3.44 we rewrite (using Eq. 3.43):

$$\frac{\partial u_1^2}{\partial x_1} + \frac{\partial u_1 v_1}{\partial y_1} = \frac{1}{\rho} \frac{\partial \tau_1}{\partial y_1}$$

Integrating from  $y_1 = 0$  to  $\infty$  :



$$\frac{1}{\rho} [\tau_{\infty} - \tau_0] = (u_1 v_1)_{\infty} - (u_1 v_1)_0 + \int_0^{\infty} \frac{\partial u_1^2}{\partial x_1} dy_1$$

But  $\tau_{\infty} = 0$ ,  $(u_1)_{\infty} = 0$ ,  $(u_1)_0 = (v_1)_0 = 0$ . Using Leibnitz' rule, we have:

$$\frac{\partial}{\partial x_1} \int_0^{\infty} u_1^2 dy_1 = -\frac{\tau_0}{\rho} = -u_*^2,$$

or

$$\frac{\partial}{\partial x_1} \left\{ u_{m1}^2 b_1 \int_0^{\infty} \left( \frac{u_1}{u_{m1}} \right)^2 d \left( \frac{y_1}{b_1} \right) \right\} = -u_*^2$$

Due to similarity the value of the integral is a constant, say  $F$ .

Hence:

$$F \frac{d}{dx_1} (b_1 u_{m1}^2) = -u_*^2$$

Using (3.48) and (3.50) we find:

$$F C_b (2a + 1) = - \left( \frac{u_*}{u_m} \right)^2 = - \frac{C_f}{2} \quad (3.51)$$

where  $C_f$  is a local skin friction coefficient, defined as:

$$C_f = \frac{\tau_0}{\rho u_m^2 / 2}$$





Eq. 3.51 indicates that the local skin friction coefficient is independent of  $x_1$ . Figure 3.14 shows  $\frac{u_*}{u_{m1}}$  plotted against  $\frac{x_1}{H}$ . After a certain value of  $\frac{x_1}{H}$ ,  $\frac{u_*}{u_{m1}}$  becomes indeed a constant. This is in agreement with the conclusions of Schwartz and Cosart [18]. Sigalla [19] reports a dependence of  $C_f$  on the local Reynolds number  $\frac{u_{m1} b_1}{\nu}$ , however, this variation is very "mild" so that in substance there is no contradiction. The constancy of  $C_f$  in the wall jet may also be derived in a different way, which can indicate its dependence on other parameters such as  $R_o$  and  $\frac{H}{2b_o}$ . If the defect law is assumed to be valid in the boundary layer for some range of  $y_1$ , then:

$$\frac{u_1 - u_{m1}}{u_*} = h\left(\frac{y_1}{\delta}\right),$$

where  $\delta$  is the boundary layer thickness. Due to similarity:

$$\frac{u_1}{u_{m1}} = f\left(\frac{y_1}{b_1}\right)$$

and therefore:

$$f\left(\frac{\delta}{b_1}\right) = 1,$$

hence  $\frac{\delta}{b_1} = \text{const.}$  and  $\delta = \text{const} \times b_1$ . Therefore:

$$\frac{u_1 - u_{m1}}{u_*} = h_1 \left(\frac{y_1}{b_1}\right)$$



or,

$$\frac{u_1}{u_{m1}} - 1 = \frac{u_*}{u_{m1}} h_1(\eta_1)$$

or,

$$\frac{u_*}{u_{m1}} = \frac{f(\eta_1) - 1}{h_1(\eta_1)}$$

This suggests that  $\frac{u_*}{u_{m1}}$ , and therefore  $C_f$ , is independent of  $x_1$ , and depends only on the form of the functions  $f$  and  $h_1$ . Functions  $f(\eta_1)$  and  $h_1(\eta_1)$  are unlikely to change with the dimensionless height,  $\frac{H}{2b_o}$ , however, it is possible that they change slightly with Reynolds number.

Values of  $C_f$  are plotted against  $R_o$  in Fig. 3.15. It is seen that  $C_f$  decreases with  $R_o$  whereas any dependence on  $\frac{H}{2b_o}$  appears to be very small. To evaluate fully the variation of  $C_f$  with  $R_o$  more experiments may be required. As a conclusion we may state that  $\tau_o$  varies as  $u_{m1}^2$  with the constant of proportionality being dependent on  $R_o$ .

Solving Eq. 3.51 for  $a$ , we find:

$$a = -\frac{1}{2} \left( 1 + \frac{C_f}{2FC_b} \right) \quad (3.52)$$

where  $F = \int_0^\infty f^2 d\eta \approx 0.70$  (by graphical integration). Eq. 3.52



suggests that as long as  $C_f > 0$  ,  $a < -\frac{1}{2}$  . We have seen already that  $C_b = C_b(R_o)$  ,  $C_f = C_f(R_o)$  and  $\frac{dC_b}{dR_o} > 0$  ,  $\frac{dC_f}{dR_o} < 0$  . We may therefore conclude that:

$$|a| = a(R_o) \text{ and } \frac{d|a|}{dR_o} < 0 \quad (3.53)$$

Eq. 3.52 should be used only as an approximation for values of the exponent  $a$  . The actual value of  $F$  should be generally smaller than 0.70 due to negative velocities occuring outside the jet.

The following table shows values of the exponent  $a$  computed from Eq. 3.52, using  $F = 0.70$ .

TABLE II. EXPONENT  $a$

Source	$R_o$	$H/2b_o$	$C_f$	(Computed) $a$	Run No.
Present	7,100	66.15	0.0079	- 0.576	2
	5,680	--	0.0082	- 0.573	3
Experiments	9,400	43.6	0.0069	- 0.561	4
	7,100	--	0.0072	- 0.564	5
Ref. 1	43,000	40	0.0054	- 0.519	-
	43,000	20	0.0054	- 0.519	-



The present results were evaluated using  $a = 0.60$  in Figures 3.16 and 3.17. The results of [1] are plotted in the same manner in Fig. 3.18 using  $a = 0.52$ . The exponential variation is verified for values of  $x_1$  greater than about 70 nozzle widths.

From the above, an equation for  $u_{m1}$  is derived:

$$\frac{u_{m1}}{U_o} = C \left( \frac{x_1}{2b_o} - C_o \right)^a \quad (3.53)$$

Recalling Eq. 3.22, we conclude that in general:

$$C, C_o, a = f_i(R_o, \frac{H}{2b_o}), \quad (i = 1, 2, 3)$$

We have seen already that  $a = a(R_o)$ . Values of  $C$  are plotted against  $\frac{H}{2b_o}$  in Fig. 3.19 where a single line may be drawn through the data. Although these values of  $C$  are tentative it appears that  $C$  depends little on  $R_o$ . The coefficient  $C_o$  is a virtual origin correction and appears to depend on both  $R_o$  and  $\frac{H}{2b_o}$ . For the present experiments  $C_o \approx 35$ , whereas for the results of [1]  $C_o \approx 0$ .

A weakness of this analysis lies in the fact that the virtual origins for velocity and length scale do not coincide. This is very common in jet flows and at present there is no plausible explanation for the discrepancy.

In spite of this the analysis may be retained to serve as a guide for evaluation of experimental results. Moreover, at Reynolds





numbers higher than about  $4 \times 10^4$  the distance between the virtual origins becomes so small that it could be neglected altogether without causing appreciable errors in computing  $u_{m1}$  and  $b_1$ .

With the results already available it is possible to draw a general outline of the impinging jet. This is done in Fig. 3.13.



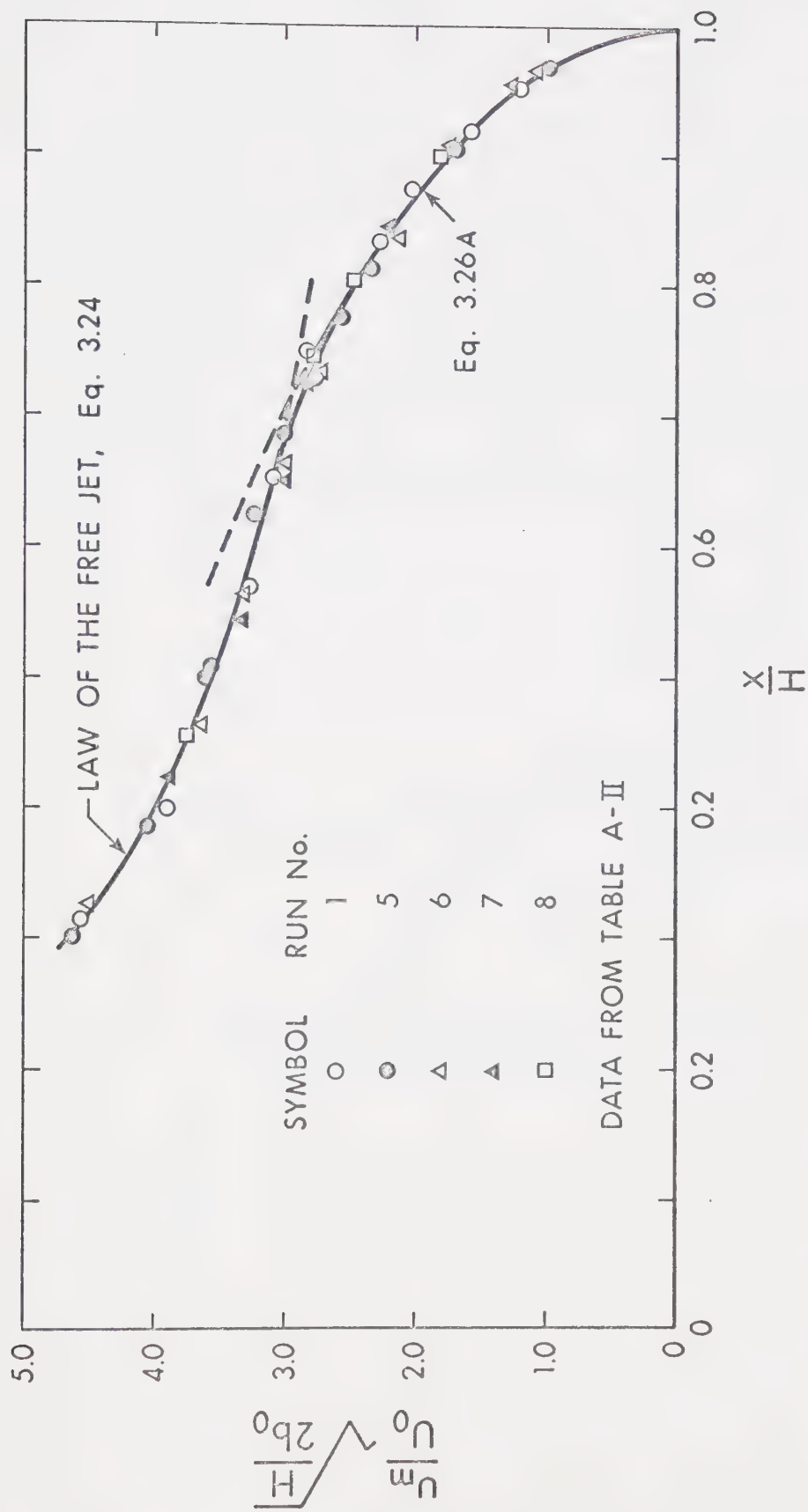


FIG. 3.2 AXIAL VELOCITY IN FREE JET AND IMPINGEMENT REGIONS



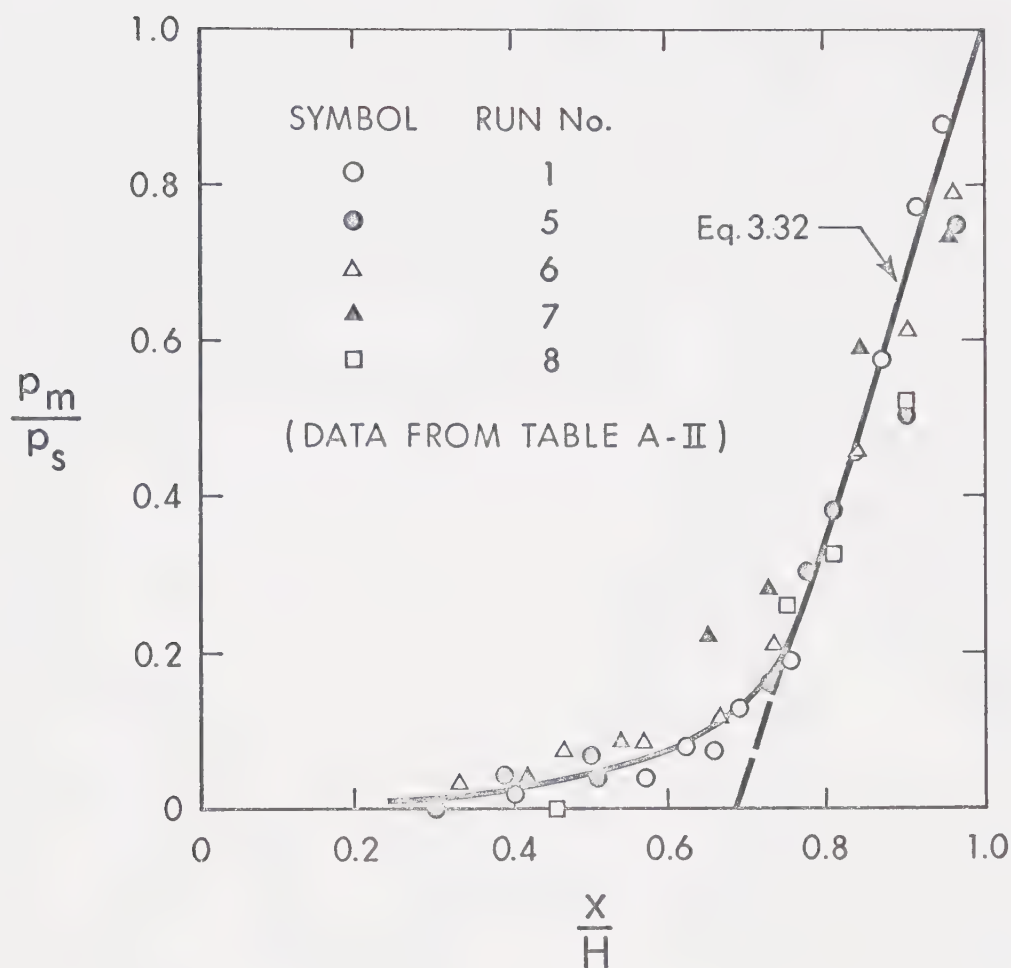


FIG. 3.3 AXIAL PRESSURE IN FREE JET AND IMPINGEMENT REGIONS



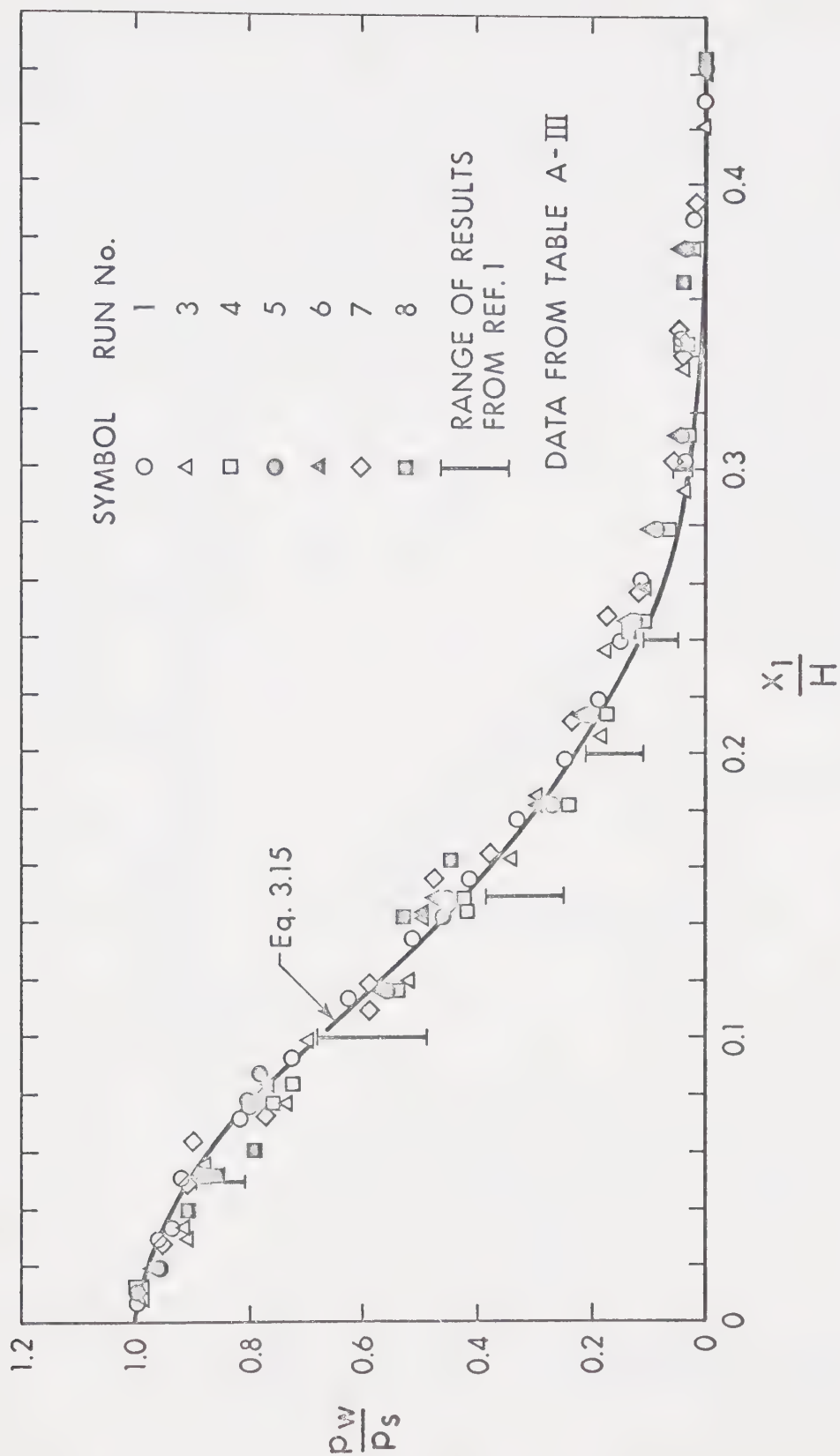


FIG. 3.4 UNIVERSAL WALL PRESSURE DISTRIBUTION





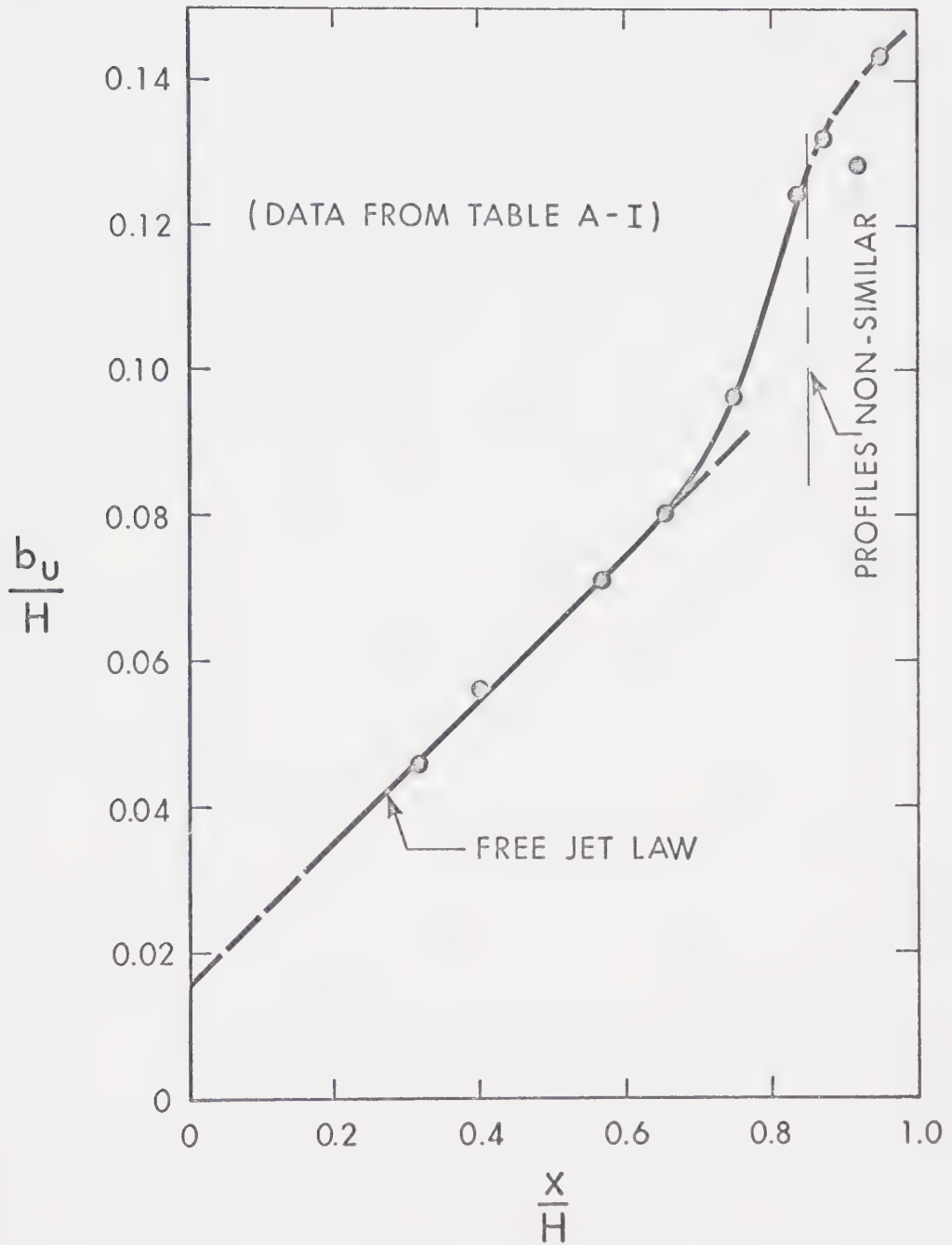


FIG. 3.5 LENGTH SCALE FOR VELOCITY IN FREE JET AND IMPINGEMENT REGIONS



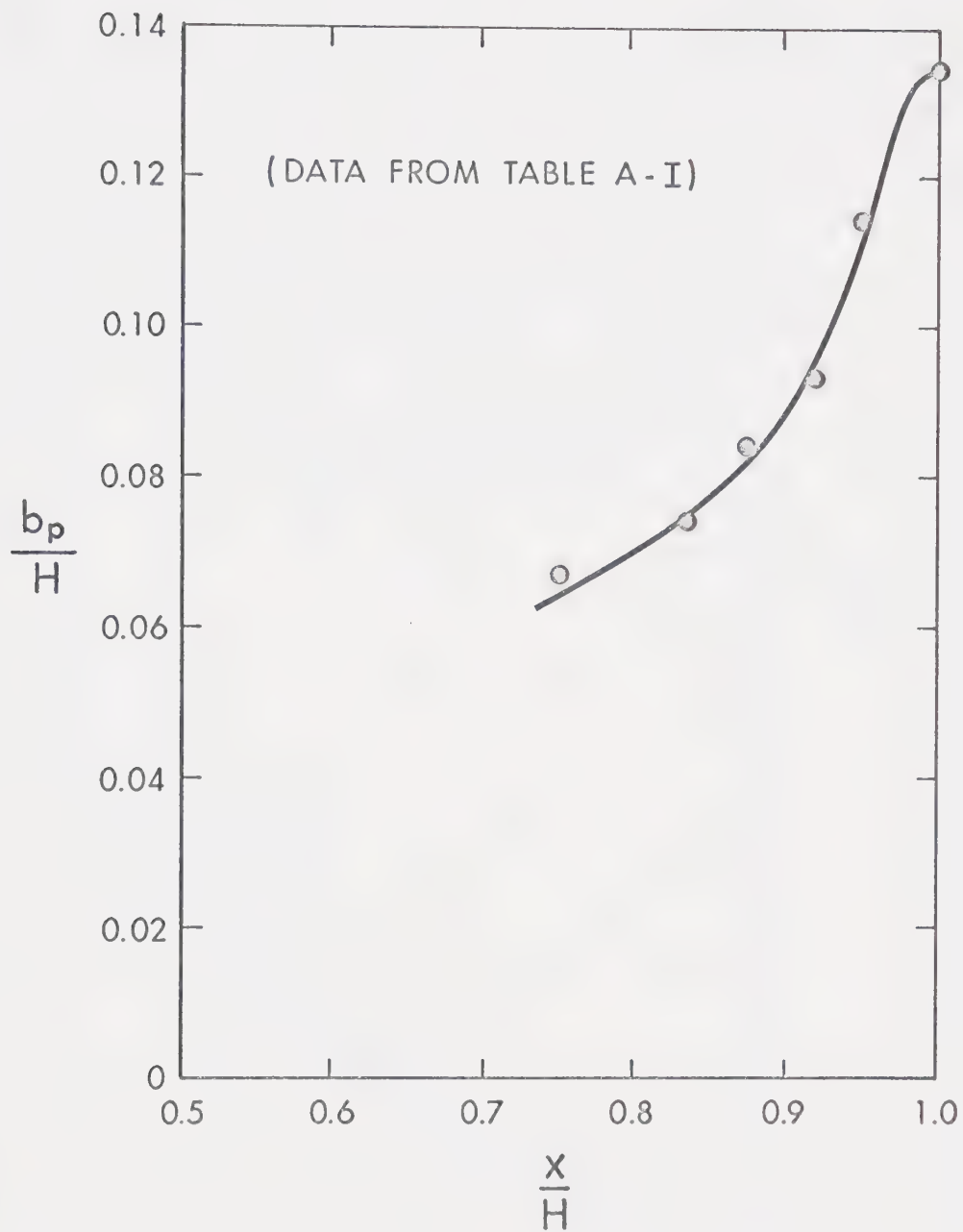


FIG. 3.6 LENGTH SCALE FOR PRESSURE IN IMPINGEMENT REGION



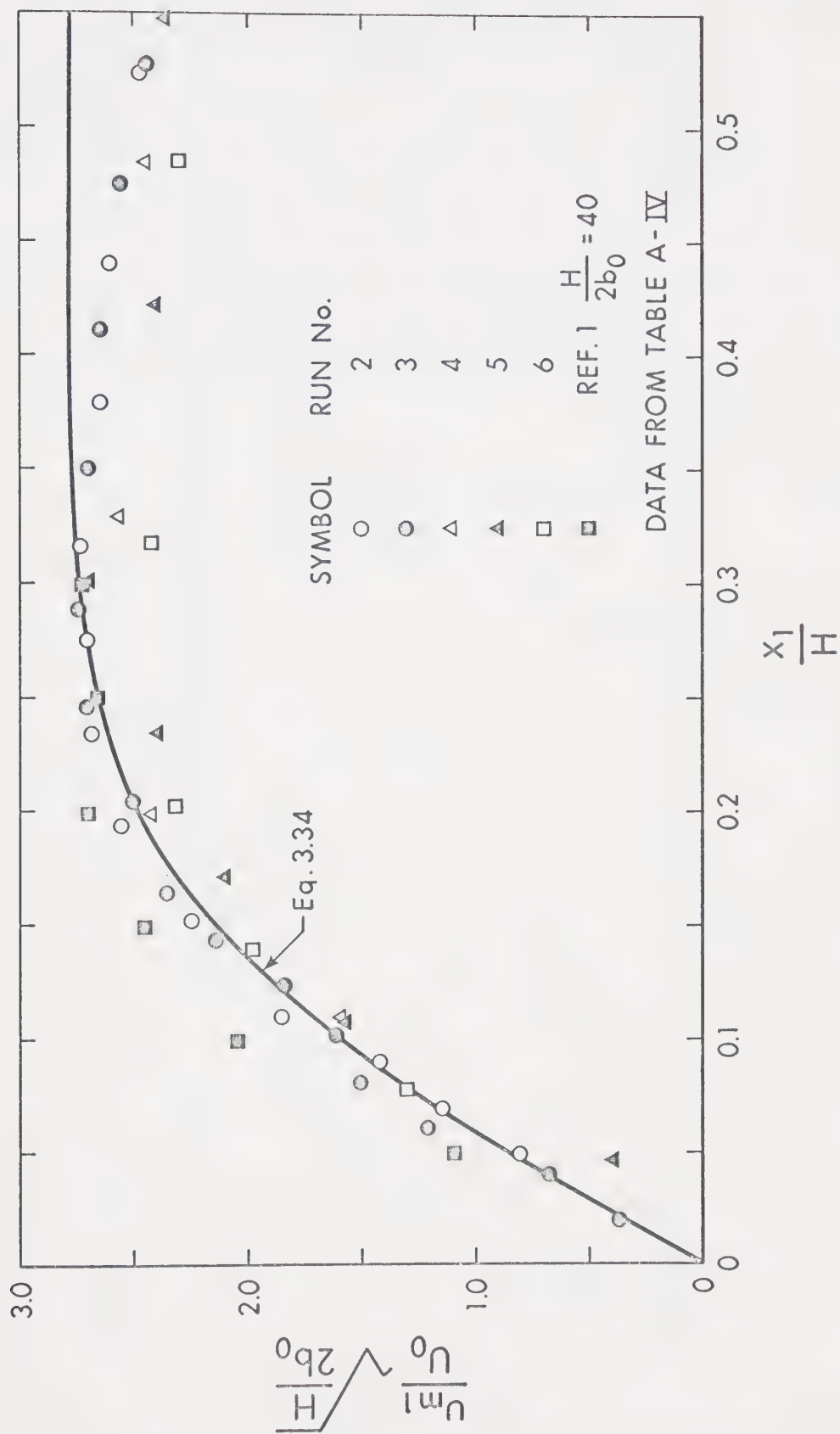


FIG. 3.7 MAXIMUM HORIZONTAL VELOCITY IN IMPINGEMENT REGION



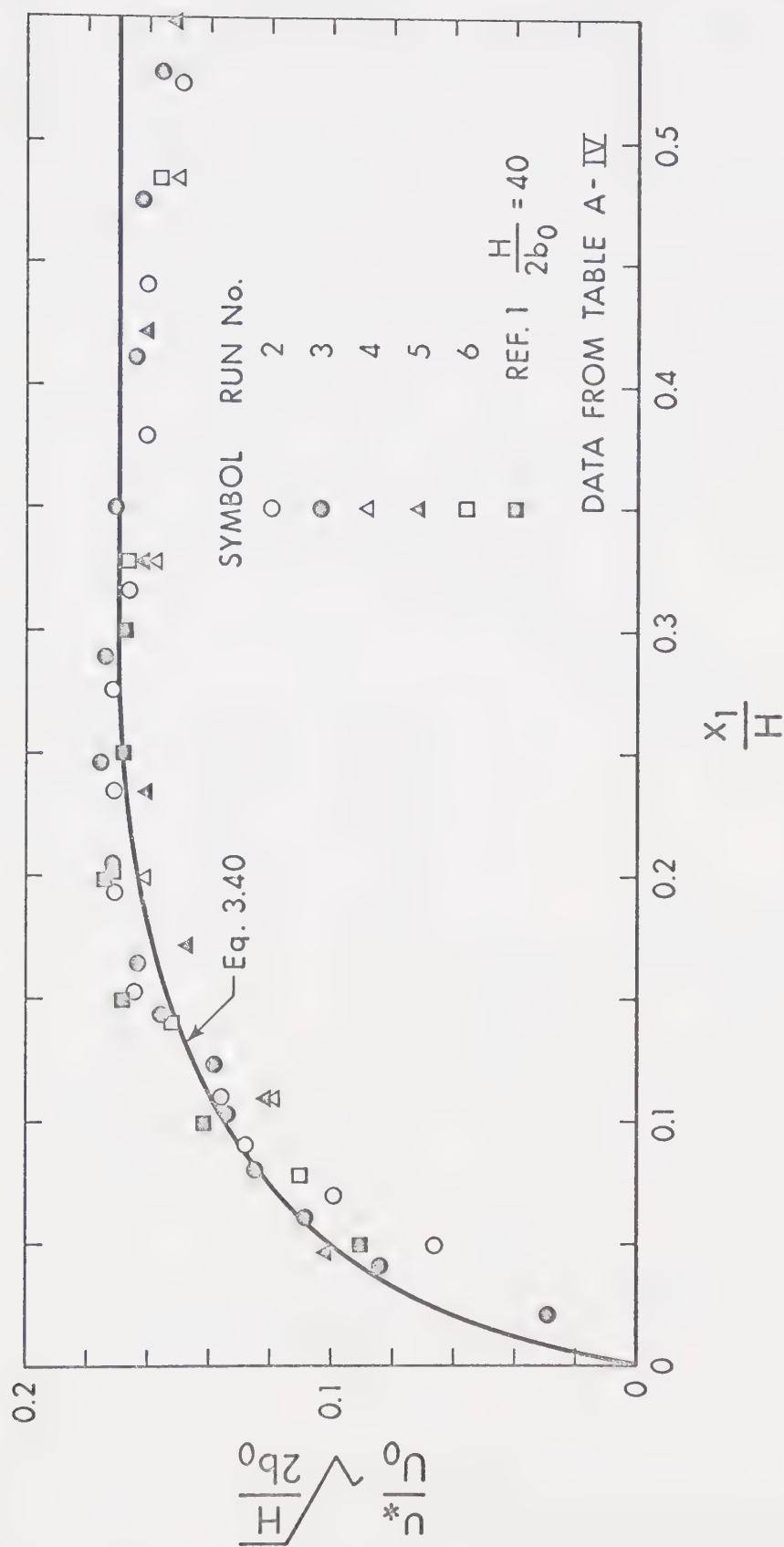


FIG. 3.8 SHEAR VELOCITY IN IMPINGEMENT REGION





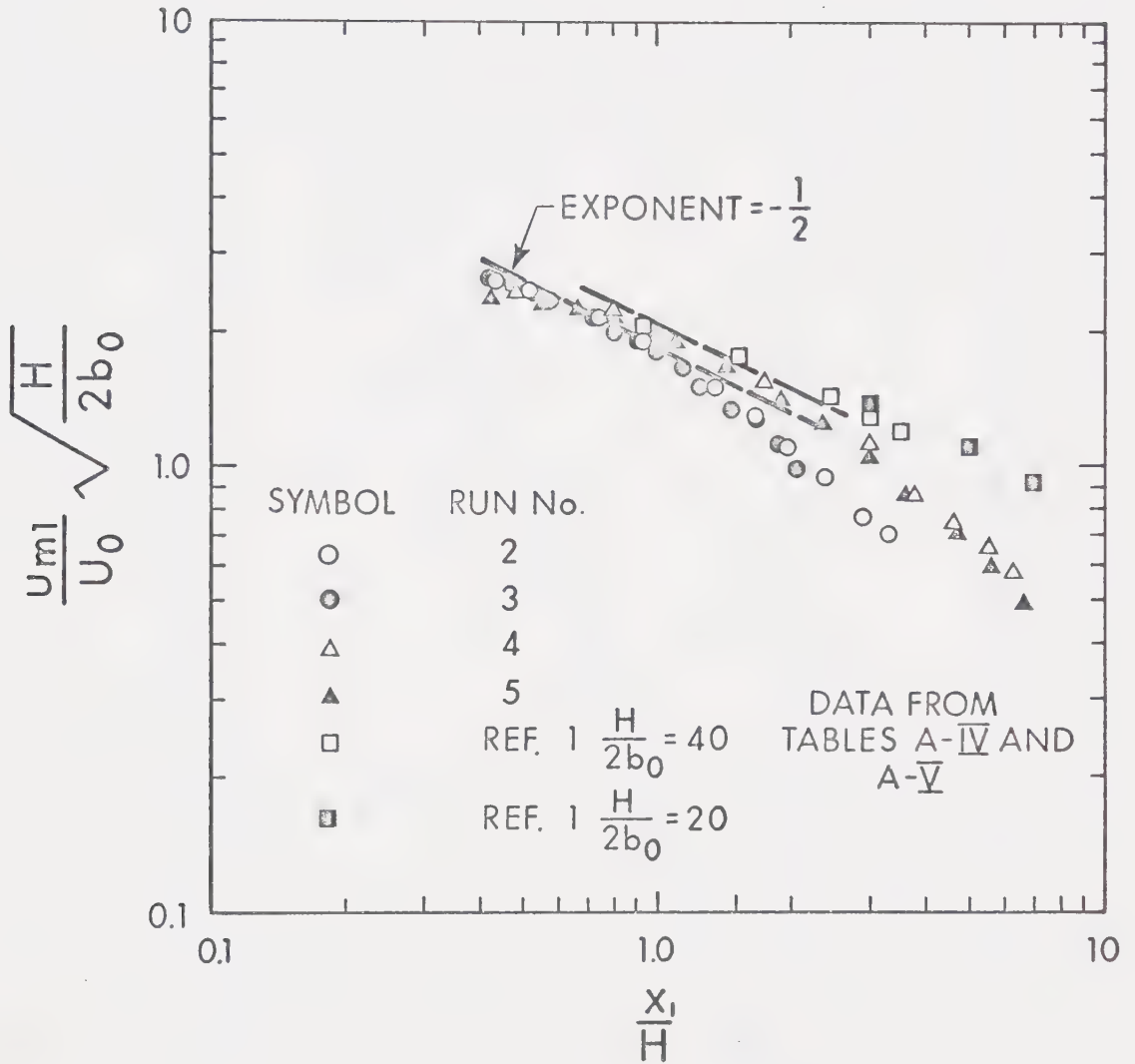


FIG. 3.10 COMPARISON OF EQN 3.21 WITH EXPERIMENTAL RESULTS



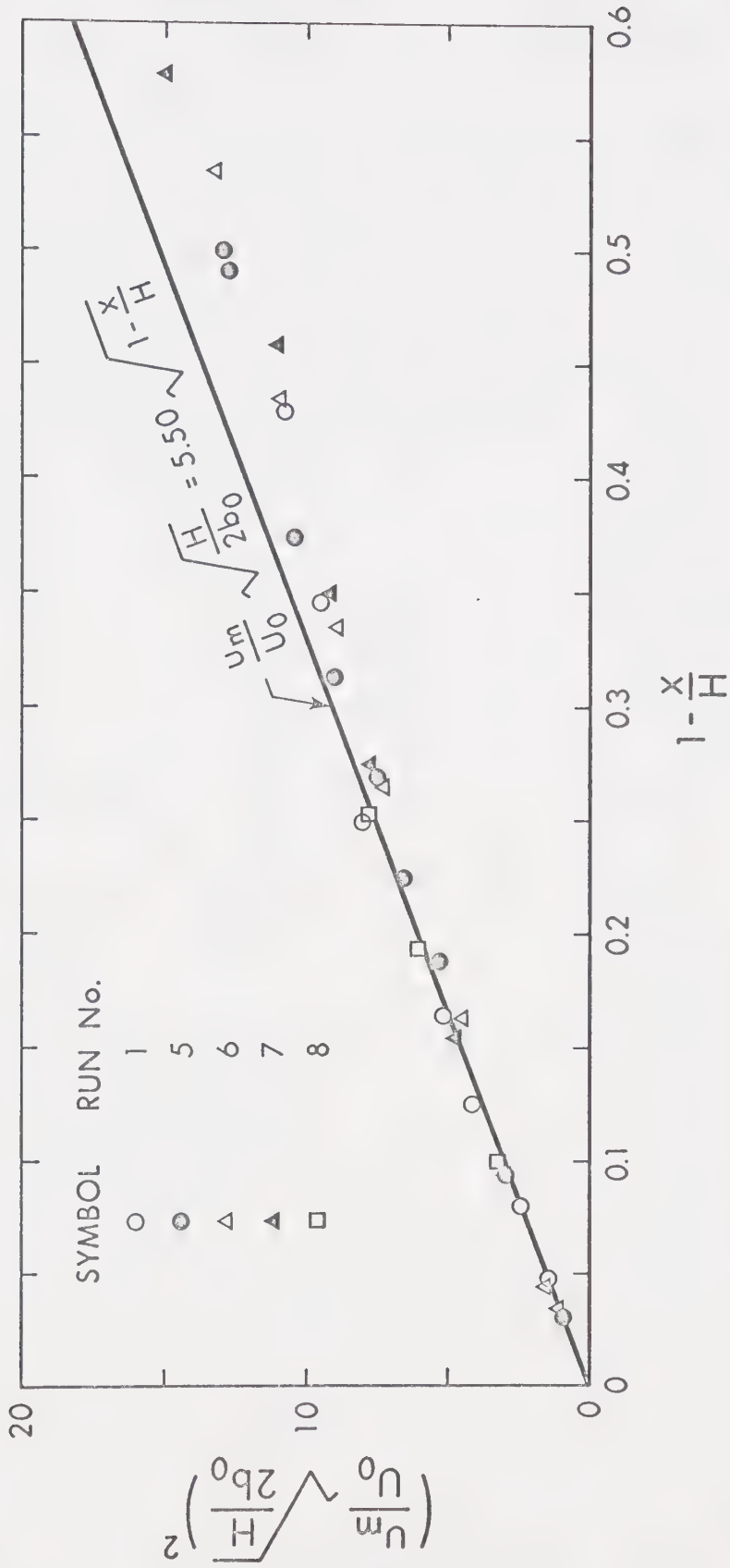


FIG. 3.11 EVALUATION OF CONSTANTS IN EQN 3.26



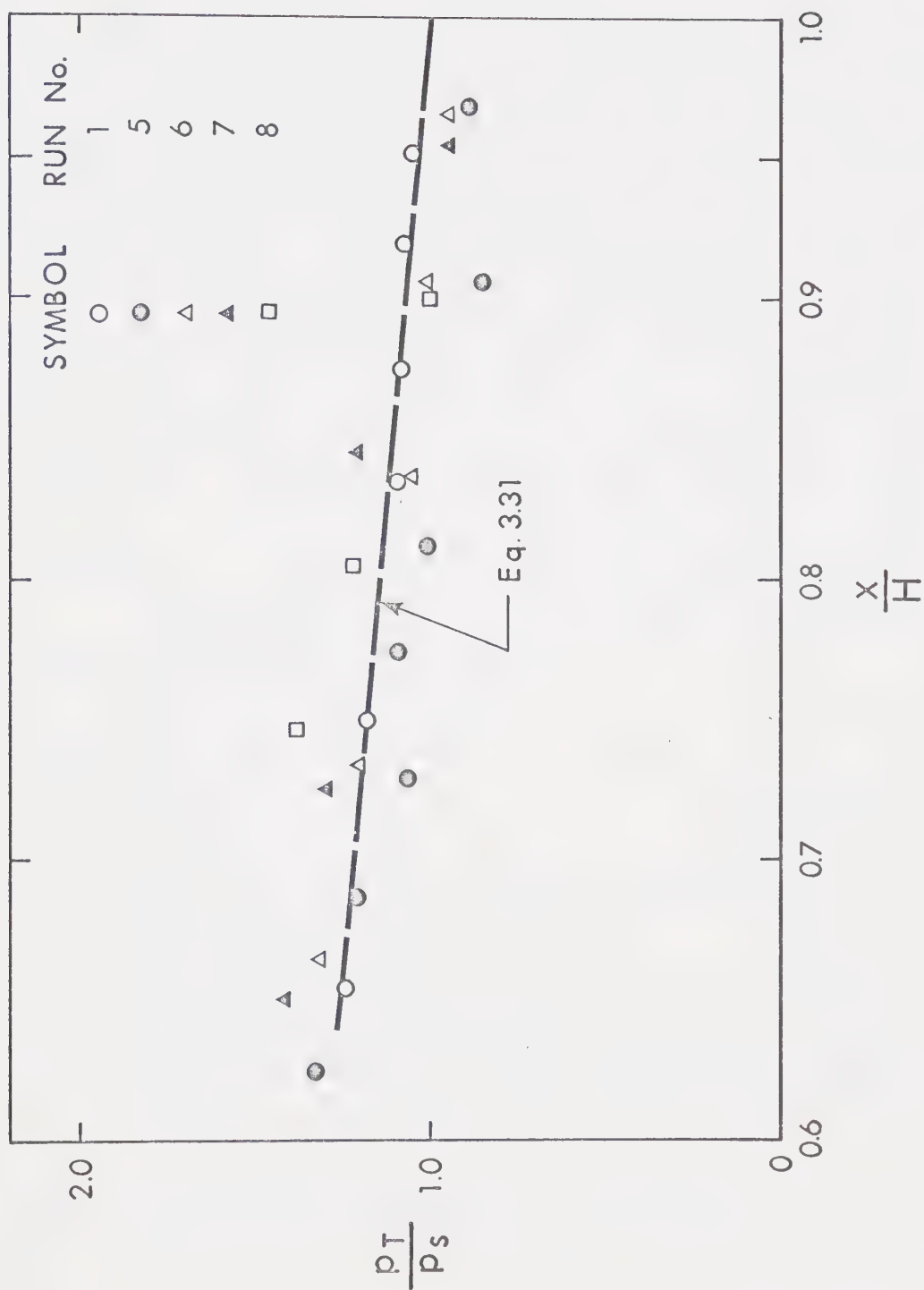


FIG. 3.12 TOTAL AXIAL PRESSURE IN IMPINGEMENT REGION



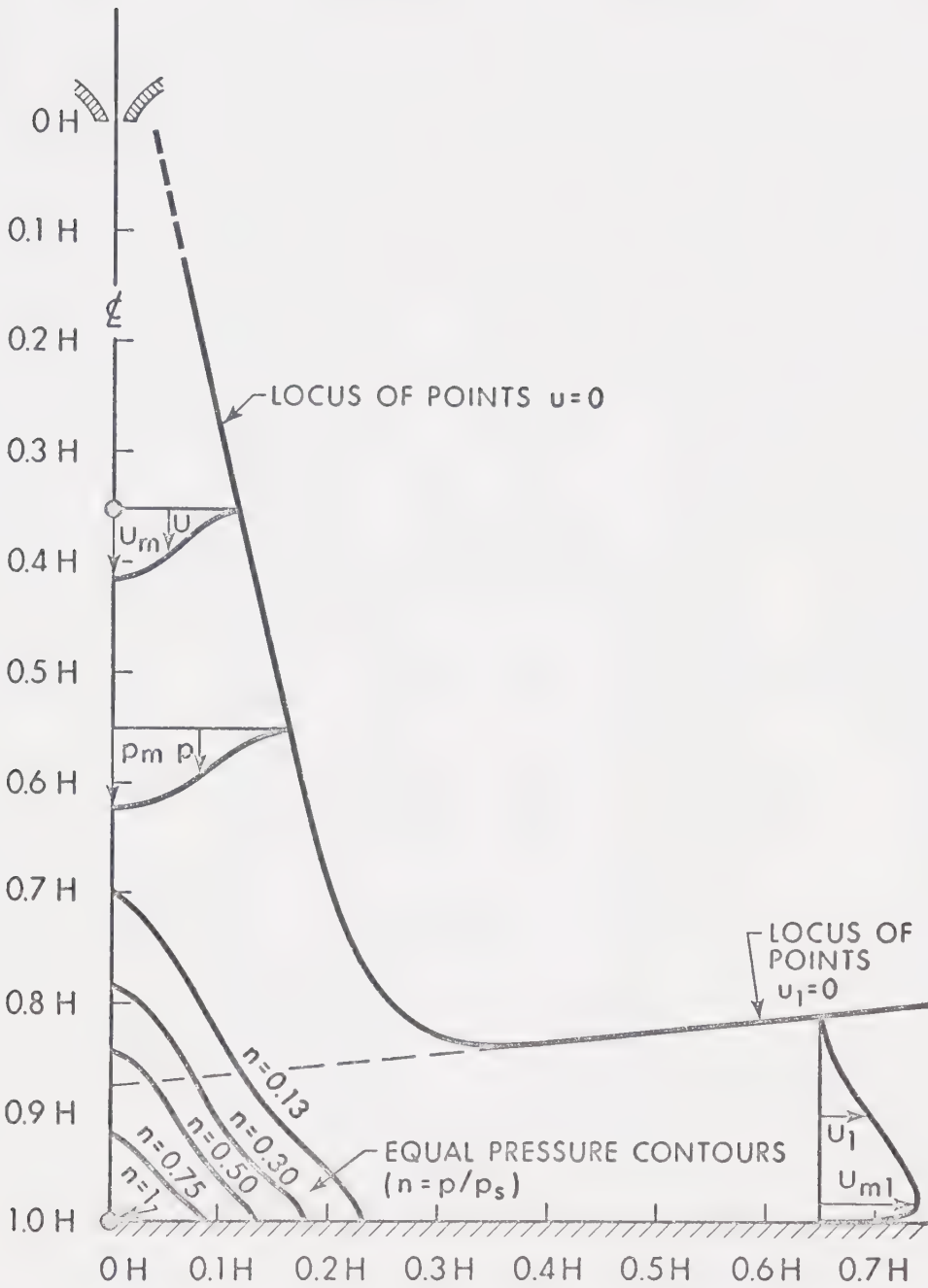


FIG. 3.13 GENERALIZED OUTLINE OF  
IMPINGING JET [RUN NO. 1 AND RUN NO. 2]





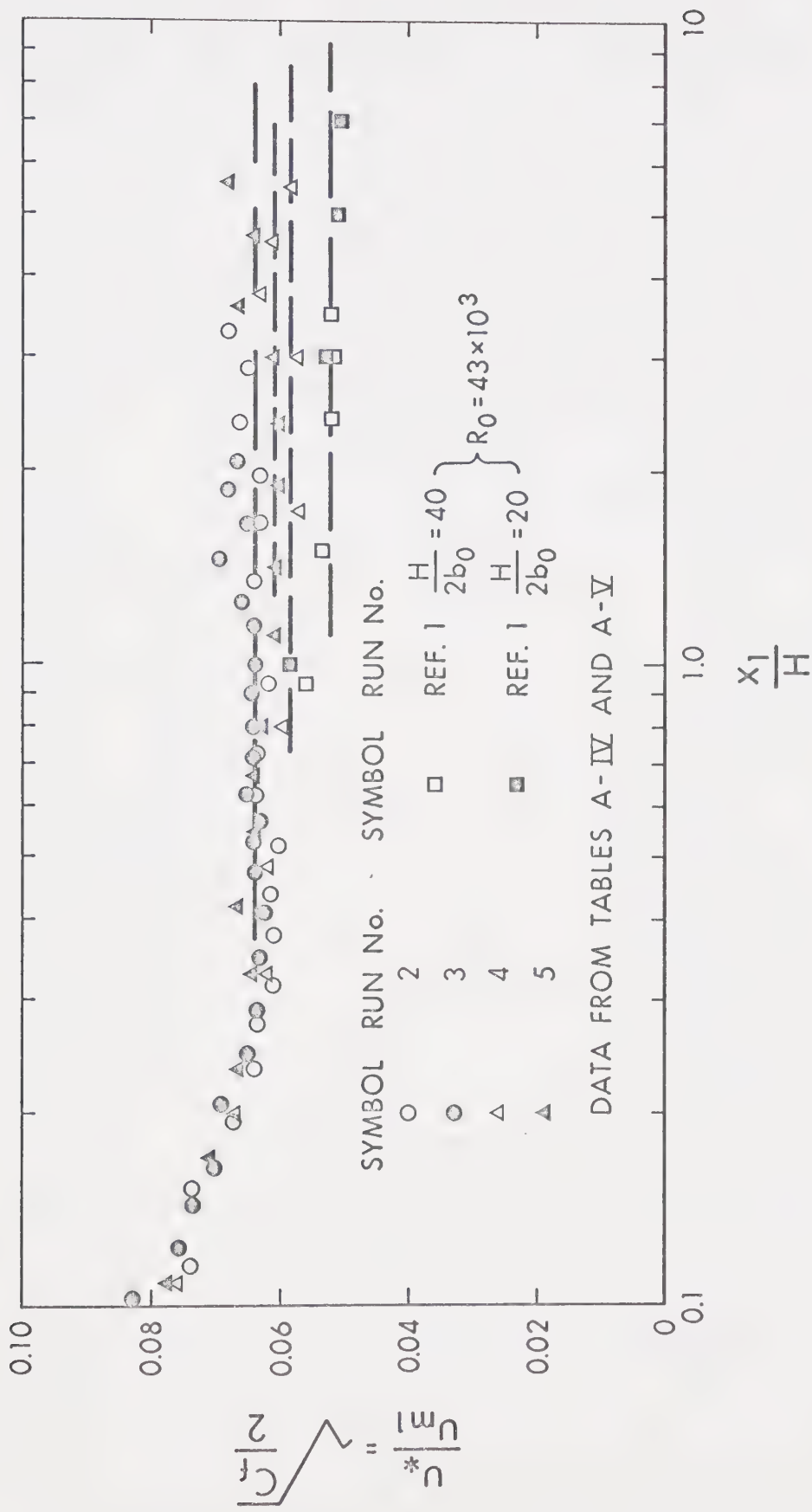


FIG. 3.14 VARIATION OF  $\frac{U^*}{U_{m1}}$  IN WALL JET



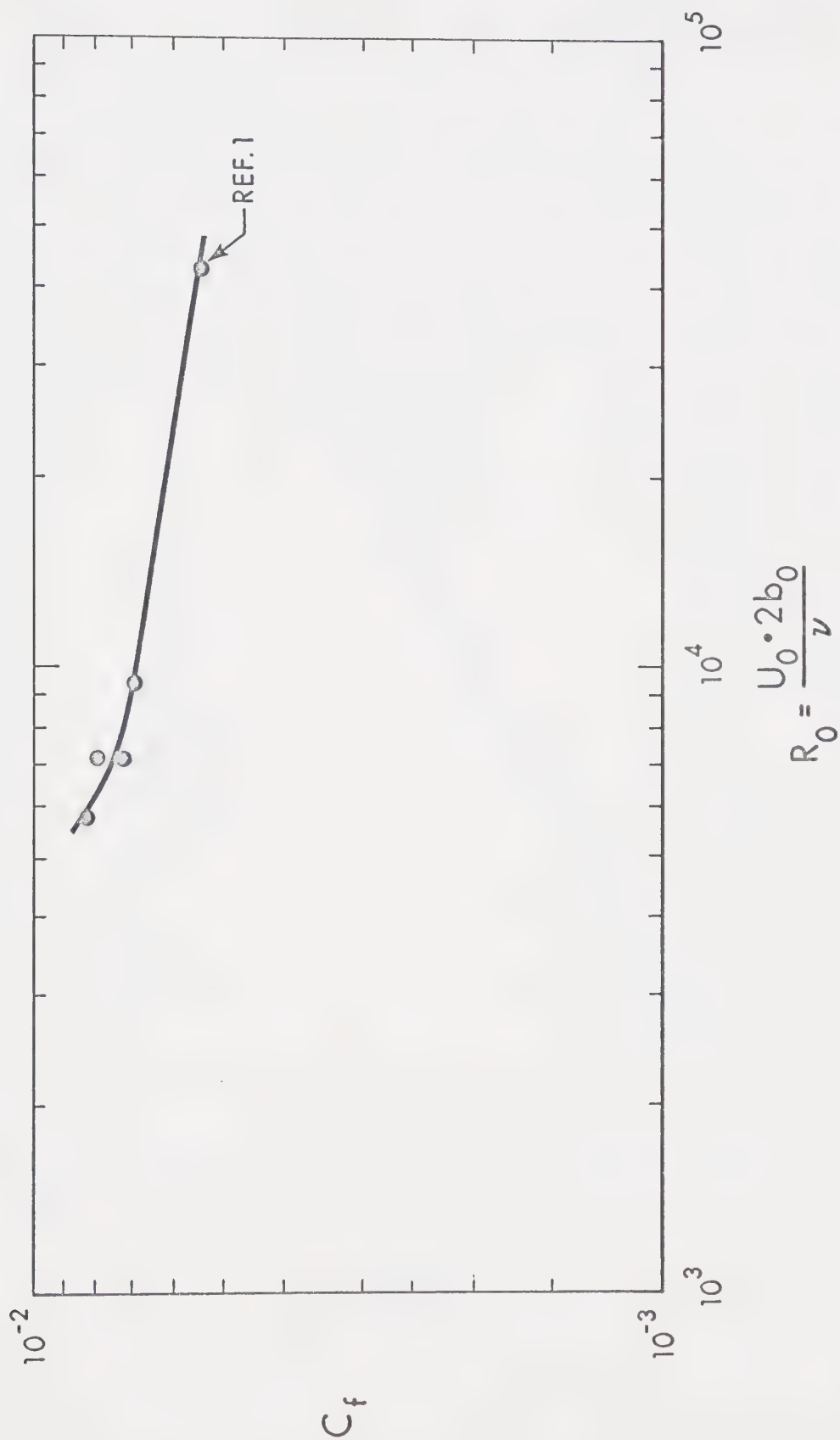
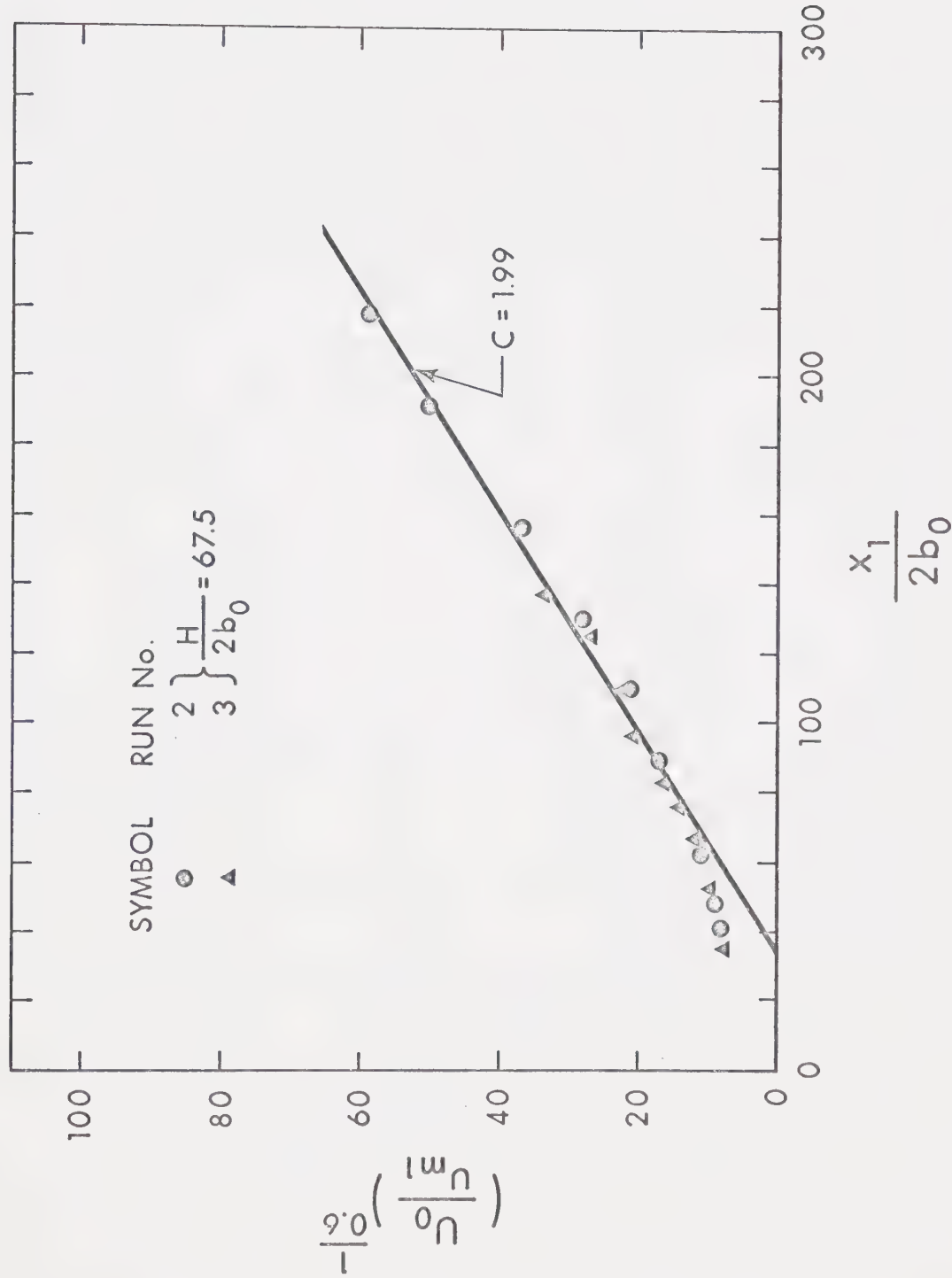


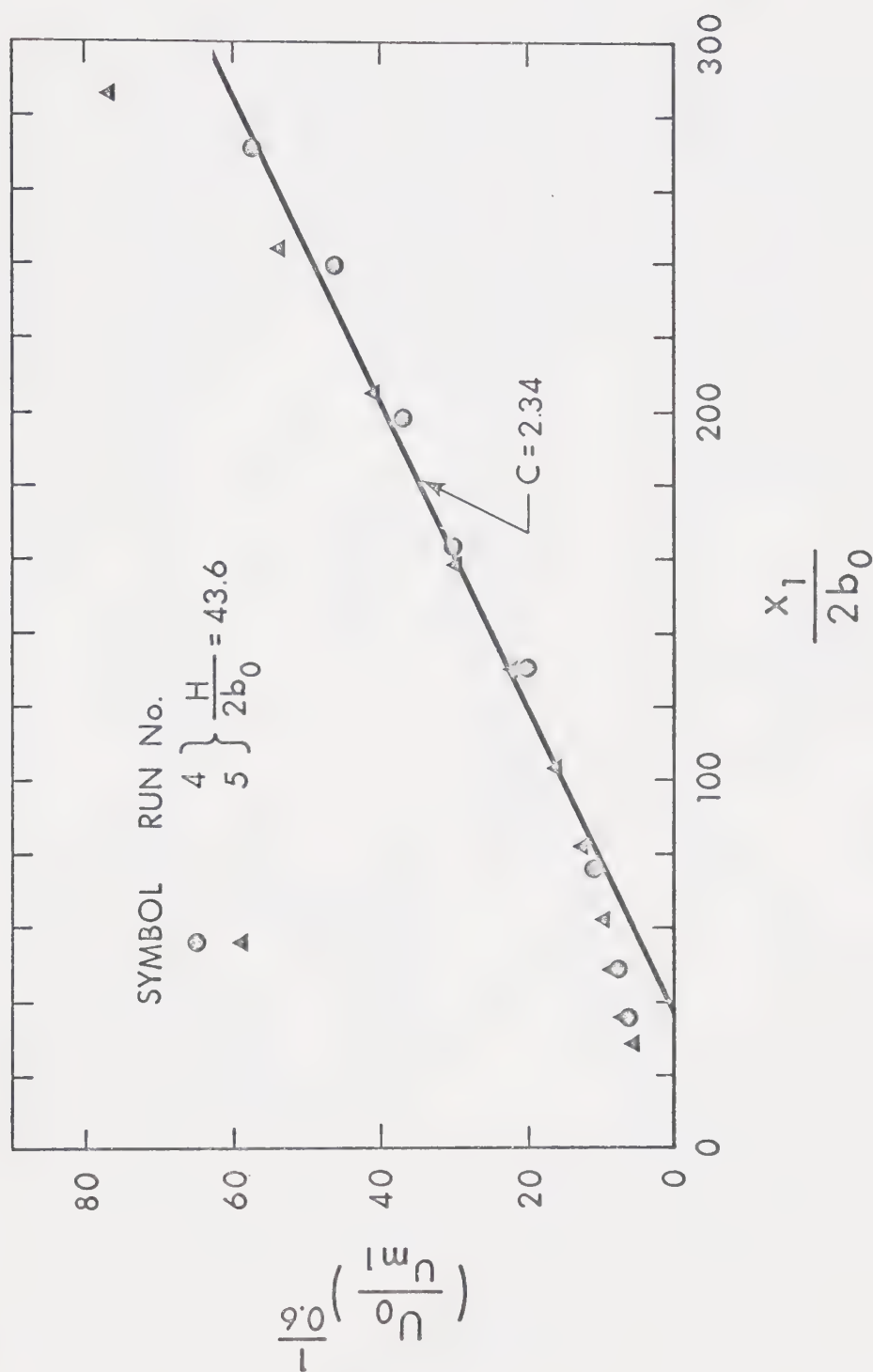
FIG. 3.15 VARIATION OF  $C_f$  WITH  $R_o$



FIG. 3.16 EVALUATION OF C IN EQN 3.53











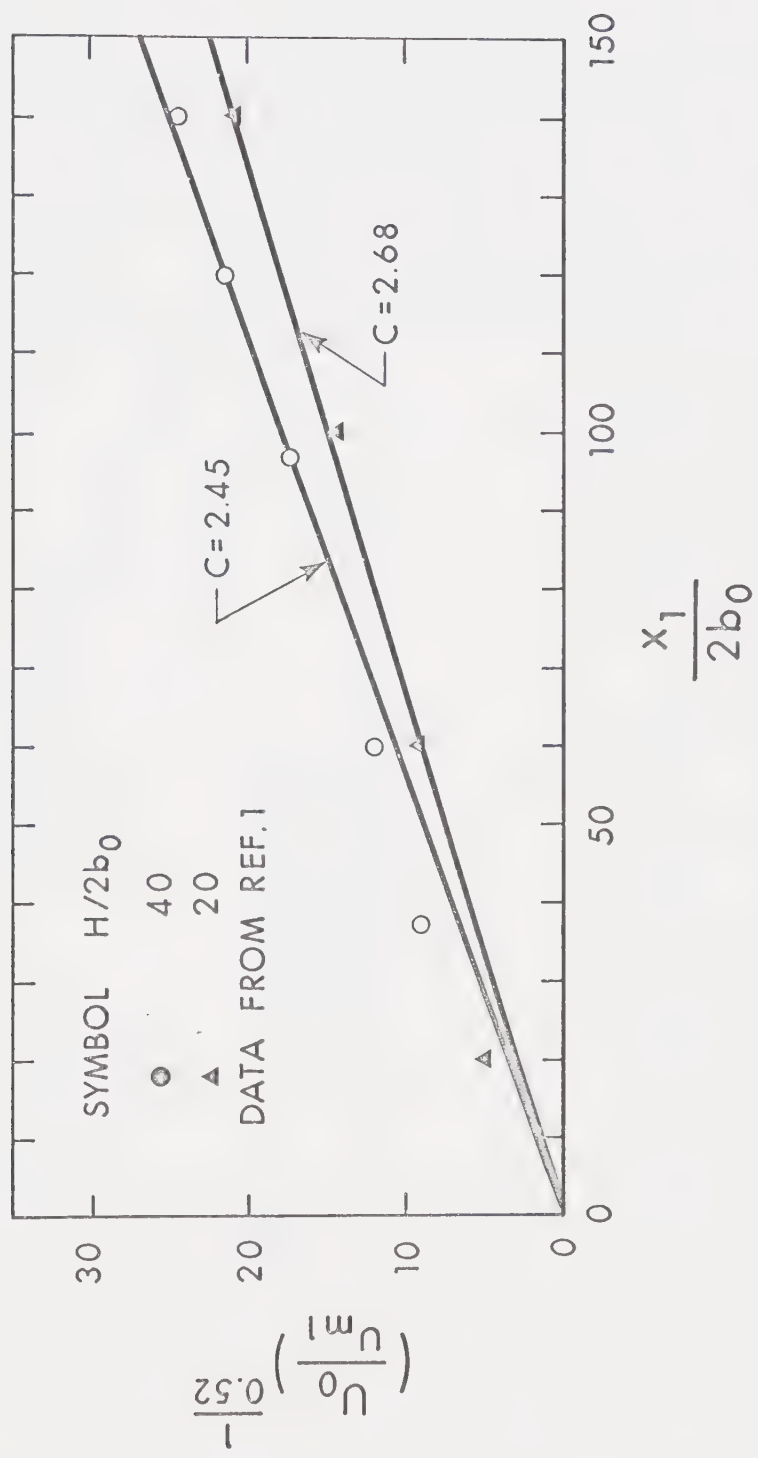
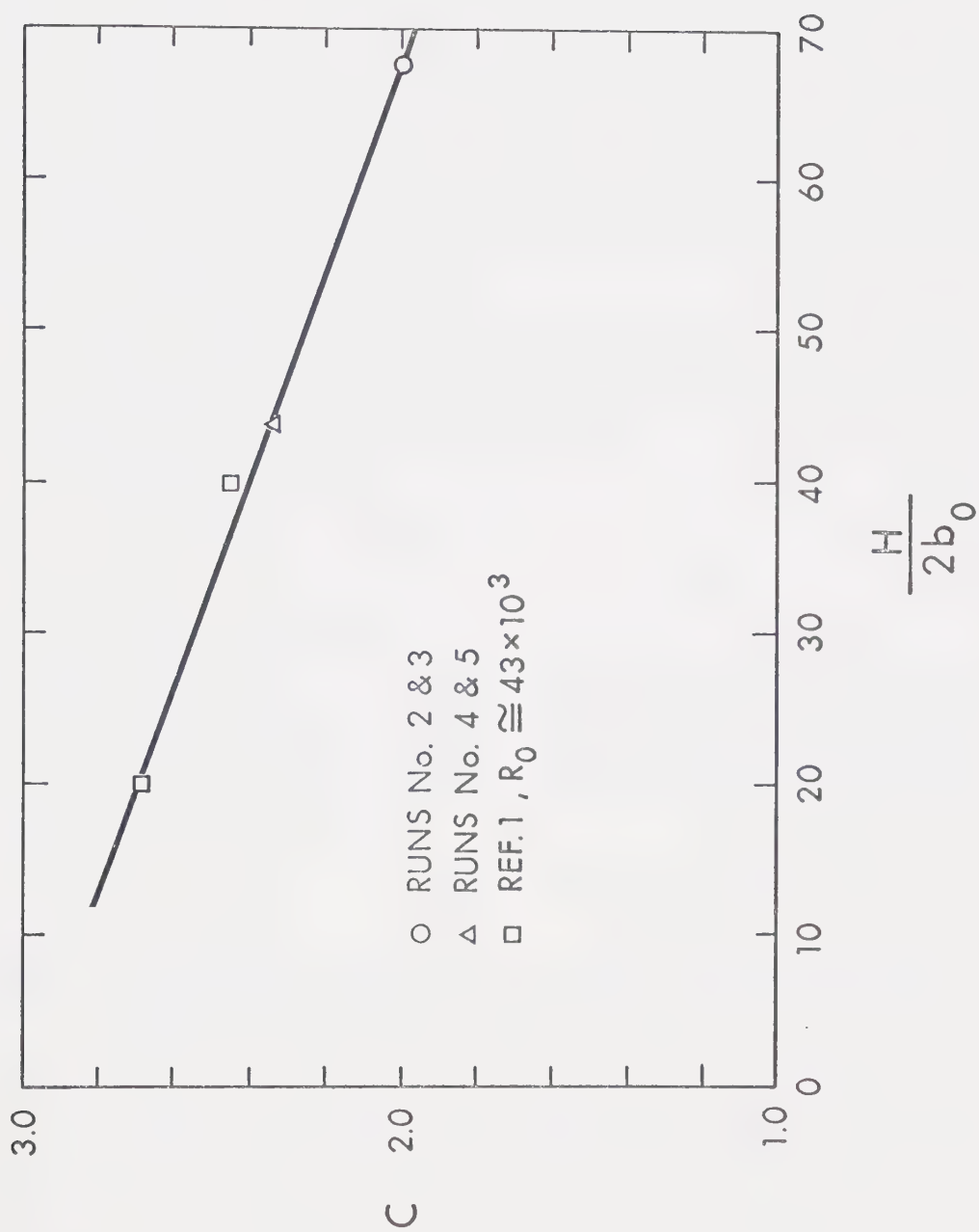


FIG. 3.18 EVALUATION OF C IN EQN 3.53



FIG. 3.19 VARIATION OF  $C$  WITH  $H/2b_0$



## CHAPTER IV

### SUMMARY AND CONCLUSIONS

An experimental and analytical investigation was carried out regarding the mean flow characteristics of plane turbulent jets impinging on smooth walls.

In agreement with previous investigations three distinct flow regions were found to exist. These are:

- (i) The Free Jet region.
- (ii) The Impingement region.
- (iii) The Wall Jet region.

The properties of region (i) were found to be almost identical with the corresponding properties of the free jet. Thus, upstream of a point  $x = x_0$  it was found:

$$\frac{u_m}{U_0} = \frac{2.40}{\sqrt{\frac{x}{2b_0} - 2.5}}, \quad x_0 \approx 0.7H \quad \text{and} \quad \frac{b_u}{H} = 0.10\left(\frac{x}{H} + 0.15\right), \quad x_0 \approx 0.65H$$

The static pressure in excess of the hydrostatic was not zero, but it was found to be generally small. The velocity profiles were found to be similar in the sense that  $\frac{u}{u_m} = f\left(\frac{y}{b_u}\right)$ . The function  $f$  may be approximated by an error distribution. It is also in good agreement



with Tollmien's classical solution.

Flow properties in region (ii) were investigated by means of a Pitot cylinder which was calibrated first. The calibration was based on the assumption that within a range of tube Reynolds numbers the pressure distribution around the cylinder does not change appreciably with Reynolds number. This was verified within the range  $R_T \approx 1400$  to 5500 for values of polar angle  $\phi$  from 0 to 70°. Caution should be exercised if it is desired to use the calibration charts presented here at  $R_T$  values far below or beyond the above range. In view of the fact that the pressure distribution varies appreciably with  $R_T$  in the wake zone, it is suggested that for  $R_T \gg 5500$  or  $R_T \ll 1400$ , the present calibration charts be used with the restriction  $|\phi| \leq 30^\circ$ . A lower limit of  $R_T$  should be in the order of 300.

In the impingement region the vertical velocity distributions were found to remain similar, for  $x \leq 0.85H$ . For  $x \geq 0.85H$  the profiles are not similar although deviation from the similarity curve is not extreme. For crude approximations, the similarity curve could be used. The length scale,  $b_u$ , was studied experimentally. The pressure profiles were found to be similar in this region, so that:

$$\frac{p}{p_m} = f\left(\frac{y}{b_p}\right).$$

The length scale,  $b_p$ , was studied experimentally.





The velocity and pressure scales are given by:

$$\frac{u_m}{U_o} \sqrt{\frac{H}{2b_o}} = 5.50 \sqrt{1 - \frac{x}{H}}, x \geq 0.7H$$

$$\frac{p_m}{p_s} = 3.2 \frac{x}{H} - 2.2, x \geq 0.73H$$

The total pressure,  $p_T$ , on the axis is given by:

$$\frac{p_T}{p_s} = 1.73 - 0.73 \frac{x}{H}, x \geq 0.7H$$

The variation of  $u_m$  was obtained on the basis of the experimental observation that the flux of  $x$ -momentum in the  $y$  direction is almost independent of  $x$  near the axis. This physical concept was applied to the circular jet yielding good agreement with available experimental data. The above equations are likely to be erroneous in a small region very near the stagnation point, because the flow tends to become potential in this region.

The stagnation pressure,  $p_s$ , may be predicted from:

$$\frac{p_s}{\rho U_o^2 / 2} \frac{H}{2b_o} \approx 7.7$$

The wall pressure distribution was found to agree well with the



function:

$$\frac{p_w}{p_s} = e^{-38.5 \left(\frac{x_1}{H}\right)^2}$$

The maximum horizontal velocity is given by:

$$\frac{u_{m1}}{U_o} \sqrt{\frac{H}{2b_o}} = 2.77 \left\{ 1 - \frac{p_w}{p_s} \right\}^{1/2} \quad \text{for } x_1 \leq 0.4H$$

The wall shear stress is given by:

$$\frac{\tau_o}{\rho U_o^2 / 2} \frac{H}{2b_o} = 0.058 I_p \left( 6.2 \frac{x_1}{H} \right) \quad \text{for } x_1 \leq 0.4H,$$

where  $I_p \left( 6.2 \frac{x_1}{H} \right)$  is the probability integral between 0 and  $6.2 \frac{x_1}{H}$ .

According to Patel's criteria for favourable pressure gradient flows, the experimental results for wall shear stresses are likely to involve errors larger than 6% for  $x_1 \leq 0.225 H$ .

In region (iii) the flow is established to self-similarity in the sense:  $\frac{u_1}{u_{m1}} = f(\eta_1)$ ,  $\eta_1 = \frac{y_1}{b_1}$ , after approximately 70 nozzle widths from the stagnation point.

The velocity scale is given by:

$$\frac{u_{m1}}{U_o} = C \left( \frac{x_1}{2b_o} - C_o \right)^a$$



where  $a$  is a function of Reynolds number,  $R_o$ , and is generally smaller than  $-\frac{1}{2}$ . As  $R_o$  increases,  $a$  tends to  $-\frac{1}{2}$ , and it could be taken as  $-\frac{1}{2}$  for  $R_o \geq 50,000$ .

$C$  is a parameter depending generally on  $\frac{H}{2b_o}$  and  $R_o$ , however, the dependence on  $R_o$  was indicated to be weak.

$C_o$  is a virtual origin correction. Generally,  $C_o$  depends on  $\frac{H}{2b_o}$  and  $R_o$ . For the present set of results  $C_o \approx 35$  whereas for the results of [1], where  $R_o \approx 4.3 \times 10^4$ ,  $C_o \approx 0$ . The length scale,  $b_1$ , is given by:

$$b_1 = C_b (x_1 + \bar{x})$$

where  $\bar{x}$  is a virtual origin correction and  $C_b$  was found to depend only on  $R_o$ .

The shear stress was found to be proportional to the square of the velocity scale,  $u_{ml}$ , ie:

$$\frac{\tau_o}{\rho u_{ml}^2 / 2} = C_f \quad \text{for} \quad \frac{x_1}{H} \geq 0.5$$

The local skin friction coefficient,  $C_f$ , is a function of  $R_o$  only and  $\frac{dC_f}{dR_o} < 0$ .

The results reported in this thesis should be applicable for impingement heights not smaller than the length of the potential core of the initial jet.



## REFERENCES

1. Schauer, J. J. and Eustis, R. H. "The Flow Development and Heat Transfer Characteristics of Plane Turbulent Impinging Jets", Technical Report 3, Dept. of Mechanical Engineering, Stanford University, Oct., 1963.
2. Tani, I. and Komatsu, Y. " Impingement of a Round Jet on a Flat Surface", pp. 672-676, ed. by Henry Goertler, Proc. of the Eleventh International Congress of Applied Mechanics, Munich, Germany, 1964.
3. Poreh, M. and Cermak, J. E. "Flow Characteristics of a Circular Submerged Jet Impinging Normally on a Flat Boundary", Proc. Sixth Midwestern Conference on Fluid Mechanics, pp. 198-212, 1959.
4. Bradshaw, P. and Love, E. M. "The Normal Impingement of a Circular Air Jet on a Flat Surface", ARC, R and M No. 3205, 1961.
5. Mathieu, J. "Contribution a l'Etude Aerothermique d'un Jet Plan Evoluant en Presence d'une Paroi", Doctor of Science Thesis, University of Grenoble, Oct., 1959.
6. Ower, E. and Pankhurst, R. C. "The Measurement of Air Flow", Pergamon Press Ltd, New York, Fourth Ed., 1966.
7. Glaser, A. H. "The Pitot Cylinder as a Static Pressure Probe in Turbulent Flow", J. Scient. Instrum. 29, (1952) pp. 219-221.
8. Winternitz, F. A. L. "Cantilevered Pitot Cylinder", Engr. (1955) 729.
9. Rajaratnam, N. and Muralidhar, D. "Yaw and Pitch Probes", Dept. of Civil Engineering, University of Alberta, Edmonton, Canada, Sept.'67.
10. Schlichting, H. "Boundary Layer Theory", McGraw-Hill Book Co., New York, Sixth Ed., 1968.
11. Schiller, L. and Linke, W. "Pressure and Frictional Resistance of a Cylinder at Reynolds Numbers 5,000 to 40,000", National Advisory Committee for Aeronautics, Technical Memorandum No. 715.
12. Preston, J. H. "The Determination of Turbulent Skin Friction by Means of Pitot Tubes", J. of the Royal Aero. Soc., London, England, Vol. 58, Feb. 1954, pp. 109-121.
13. Patel, V. C. "Calibration of the Preston Tube and Limitations on Its Use in Pressure Gradients", J. Fluid Mechanics, Vol. 23, pp. 185-208, 1965.
14. McGrew, J. "The Effect of Probe Geometry in the Determination of Skin Friction by Means of Pitot Tubes", M. Sc. Thesis, Syracuse Univ., New York, 1960.





15. Quarmby, A. and Das, H. K. "Displacement Effects on Pitot Tubes with Rectangular Mouths", The Aeronautical Quarterly, pp. 129-138, May 1969.
16. Rajaratnam, N. "Plane Turbulent Wall Jets on Rough Boundaries", Technical Report, Dept. of Civil Engineering, University of Alberta, Edmonton, Canada, June 1965. (Also published in Water Power, London, England, April, May, June 1967).
17. Rajaratnam, N. "Introduction to Turbulent Jets, Plumes and Wakes", (In Preparation), Dept. of Civil Engineering, University of Alberta, Edmonton, Canada.
18. Schwartz, W. H. and Cosart, W. P. "The Two-Dimensional Turbulent Wall Jet", Journal of Fluid Mechanics, Vol. 10, pp. 481-495, 1961.
19. Sigalla, A. "Measurements of Skin Friction in a Plane Turbulent Wall Jet", J. Royal Aeronautics Society, London, Vol. 62, pp. 873-877.
20. Iwagaki, Y. and Tsuchiya, Y. "Boundary Layer Growth in Wall Jets Issuing from a Submerged Outlet", Proc., Ninth National Congress on Applied Mechanics, pp. 259-264, 1959.
21. Poreh, M. and Tsuei, Y. G. and Cermak, J. E. "Investigation of a Turbulent Radial Wall Jet", J. Applied Mechanics, June 1967, pp. 457-463.
22. Tsuei, Y. G. "Axisymmetric Boundary Layer of a Jet Impinging on a Smooth Plate", Ph. D. Thesis, Colorado State University, Fort Collins, Colo., 1962.
23. Abramovich, G. N. "The Theory of Turbulent Jets", Technical Editing by Leon H. Schindel, the M.I.T. Press, Massachusetts Institute of Technology, Cambridge, Massachusetts, 1963.



APPENDIX A DATA TABLES

TABLE A-I. LENGTH SCALES - RUN NO. 1

$x$ (in)	$\frac{x}{H}$	$b_u$ (in)	$b_p$ (in)	$\frac{b_u}{H}$	$\frac{b_p}{H}$
1.88	.317	.273	-	.046	-
2.38	.401	.333	-	.056	-
3.38	.569	.420	-	.071	-
3.88	.654	.477	-	.080	-
4.45	.750	.570	.400	.096	.067
4.95	.835	.735	.440	.124	.074
5.19	.875	.785	.500	.132	.084
5.45	.919	.760	.550	.128	.093
5.65	.952	.846	.680	.143	.114
5.93	1.000	-	.795	-	.134



TABLE A - II. AXIAL VELOCITY AND PRESSURE

RUN NO.	$\frac{x}{2b_o}$	$\frac{x}{H}$	$\frac{u_m}{U_o}$	$\frac{p_m}{p_s}$	$\frac{u_m}{U_o} \sqrt{\frac{H}{2b_o}}$	$1 - \frac{x}{H}$
1	21.4	.317	.555	-	4.56	.683
	27.1	.401	.474	.019	3.90	.599
	38.5	.570	.397	.038	3.27	.430
	44.1	.654	.374	.076	3.08	.346
	50.6	.750	.344	.191	2.83	.250
	56.4	.835	.277	.452	2.28	.165
	59.1	.875	.248	.575	2.04	.125
	62.0	.919	.190	.771	1.57	.081
	64.3	.952	.146	.876	1.20	.048
	67.5	1.000	-	-	-	.000
5	27.3	.625	.490	.080	3.23	.375
	31.8	.729	.415	.160	2.74	.271
	30.0	.687	.454	.129	3.00	.313
	21.8	.500	.545	.073	3.60	.500
	13.2	.303	.700	.000	4.62	.697
	16.9	.387	.610	.036	4.03	.613
	22.2	.509	.540	.044	3.57	.491
	33.8	.775	.387	.306	2.56	.225
	35.5	.812	.351	.365	2.32	.188
	39.5	.906	.258	.500	1.70	.094
	42.2	.968	.150	.745	.99	.032
	43.6	1.000	-	-	-	.000
6	42.1	.966	.164	.790	1.08	.034
	39.5	.906	.260	.608	1.72	.094
	36.5	.837	.320	.456	2.11	.163
	32.1	.734	.410	.213	2.71	.266
	29.0	.665	.453	.124	2.99	.335
	24.7	.565	.500	.084	3.30	.435
	20.3	.465	.550	.076	3.63	.535
	14.3	.328	.680	.030	4.49	.672
	43.6	1.000	-	-	-	.000
7	29.7	.955	.228	.735	1.27	.045
	26.2	.846	.393	.590	2.19	.154
	22.5	.726	.500	.277	2.79	.274
	20.2	.651	.540	.223	3.01	.349
	16.8	.542	.595	.090	3.32	.458
	13.1	.423	.695	.039	3.88	.577
	31.0	1.000	-	-	-	.000
8	12.6	.899	.483	.518	1.81	.101
	10.5	.747	.745	.255	2.79	.253
	11.3	.805	.660	.327	2.47	.195
	6.4	.456	1.000	.000	3.75	.544
	14.04	1.000	-	-	-	.000



TABLE A - III. WALL PRESSURE DISTRIBUTION

RUN NO.	$\frac{x_1}{H}$	$\frac{P_w}{P_s}$	$\frac{P_s}{\rho U_o^2/2}$ $\frac{H}{2b_o}$	$K_{pw}$
1	.076	.800	8.15	.123
	.034	.936		
	.008	.996		
	.030	.960		
	.051	.921		
	.072	.815		
	.093	.725		
	.114	.626		
	.135	.514		
	.156	.415		
	.177	.332		
	.198	.249		
	.219	.189		
	.240	.151		
	.261	.113		
	.303	.038		
	.346	.045		
	.388	.023		
	.430	.004		
	.472	.000		
3	.094	.670	8.42	.119
	.052	.874		
	.030	.910		
	.009	.986		
	.013	.986		
	.034	.915		
	.056	.880		
	.077	.733		
	.099	.697		
	.120	.521		
	.142	.493		
	.163	.342		
	.185	.296		
	.206	.183		
	.228	.176		
	.249	.109		
	.292	.039		
	.335	.042		
	.378	.021		
	.421	.003		
	.481	.000		





TABLE A - III. WALL PRESSURE DISTRIBUTION (Cont'd)

RUN NO.	$\frac{x_1}{H}$	$\frac{p_w}{p_s}$	$\frac{p_s}{\rho U_o^2/2} \quad \frac{H}{2b_o}$	$K_{pw}$
4	.143	.420	8.64	.116
	.078	.760		
	.013	.990		
	.052	.860		
	.084	.725		
	.117	.540		
	.149	.425		
	.182	.240		
	.214	.175		
	.247	.112		
	.279	.067		
	.312	.033		
	.344	.042		
	.377	.025		
	.506	.017		
	.570	.000		
5	.143	.462	8.34	.120
	.078	.805		
	.013	.996		
	.020	.955		
	.052	.873		
	.084	.784		
	.117	.552		
	.149	.455		
	.182	.268		
	.214	.209		
	.247	.127		
	.279	.082		
	.312	.045		
	.344	.045		
	.377	.030		
	.442	.000		
	.506	.015		
	.570	.000		



TABLE - III. WALL PRESSURE DISTRIBUTION (Cont'd)

RUN NO.	$\frac{x_1}{H}$	$\frac{p_w}{p_s}$	$\frac{p_s}{\rho U_o^2/2}$ $\frac{H}{2b_o}$	$K_{pw}$
6	.143	.494	7.36	.136
	.078	.795		
	.013	.995		
	.020	.970		
	.052	.856		
	.084	.771		
	.117	.567		
	.149	.481		
	.182	.295		
	.214	.217		
	.247	.145		
	.279	.102		
	.312	.048		
	.344	.048		
	.377	.036		
	.442	.000		
7	.340	.042	7.60	.132
	.248	.175		
	.156	.476		
	.110	.590		
	.064	.898		
	.028	.952		
	.073	.770		
	.119	.590		
	.165	.379		
	.211	.235		
	.257	.120		
	.303	.460		
	.349	.048		
	.394	.018		
	.486	.000		
8	.364	.043	6.90	.146
	.162	.446		
	.061	.783		
	.040	.908		
	.142	.533		
	.243	.136		
	.344	.027		
	.445	.000		



TABLE A - IV. SHEAR STRESS AND MAXIMUM VELOCITY IN IMPINGEMENT REGION

RUN NO.	$\frac{x}{2b_o}$	$\frac{x}{H}$	$\frac{u_{m1}}{U_o}$	$\frac{u_{m1}}{U_o} \sqrt{\frac{H}{2b_o}}$	$\frac{u_*}{U_o}$	$\frac{u_*}{U_o} \sqrt{\frac{H}{2b_o}}$	$\frac{u_*}{u_{m1}}$
2	3.27	.049	.098	.80	.0081	.066	.0840
	4.63	.070	.140	1.14	.0121	.099	.0860
	6.00	.091	.175	1.42	.0157	.128	.0900
	7.36	.111	.227	1.85	.0167	.136	.0740
	10.10	.153	.277	2.25	.0203	.165	.0735
	12.8	.194	.313	2.55	.0210	.171	.0673
	15.5	.235	.329	2.68	.0210	.171	.0640
	18.3	.276	.332	2.70	.0211	.172	.0637
	21.0	.317	.335	2.73	.0204	.166	.0610
	25.1	.379	.323	2.63	.0197	.160	.0610
	29.2	.441	.320	2.60	.0197	.160	.0616
	34.6	.523	.304	2.47	.0183	.149	.0605
3	1.36	.021	.045	.37	.0036	.029	.0820
	2.73	.041	.101	.67	.0102	.083	.1010
	4.09	.062	.149	1.21	.0132	.108	.0890
	5.45	.082	.184	1.50	.0154	.125	.0840
	6.82	.103	.198	1.61	.0164	.134	.0836
	8.18	.124	.225	1.83	.0170	.138	.0755
	9.55	.144	.262	2.13	.0192	.156	.0734
	10.9	.165	.288	2.35	.0200	.163	.0700
	13.6	.206	.306	2.49	.0210	.171	.0688
	16.4	.247	.332	2.70	.0215	.175	.0647
	19.1	.289	.336	2.73	.0213	.174	.0634
	23.2	.351	.331	2.69	.0209	.170	.0631
	27.2	.412	.324	2.64	.0201	.164	.0623
	31.4	.475	.313	2.55	.0199	.162	.0637
	34.9	.527	.298	2.43	.0191	.155	.0641
4	4.80	.110	.239	1.58	.0180	.119	.0763
	14.3	.330	.387	2.56	.0238	.157	.0622
	21.1	.484	.369	2.44	.0227	.150	.0617
	8.9	.200	.366	2.42	.0244	.161	.0670
5	23.8	.547	.356	2.36	.0229	.151	.0640
	18.4	.422	.363	2.40	.0242	.160	.0668
	14.3	.328	.384	2.54	.0247	.163	.0644
	10.2	.234	.361	2.39	.0242	.160	.0670
	7.5	.172	.316	2.10	.0223	.147	.0708
	4.8	.109	.237	1.57	.0184	.121	.0774
	2.0	.047	.059	.39	.0155	.102	.2620
6	3.3	.078	.197	1.30	.0166	.110	.0842
	6.1	.141	.299	1.98	.0230	.152	.0772
	8.9	.203	.350	2.31	.0256	.169	.0730
	14.3	.328	.366	2.42	.0251	.166	.0695
	21.1	.484	.346	2.29	.0236	.156	.0680



TABLE A - V  
MAXIMUM VELOCITY, LENGTH SCALE AND SHEAR STRESS IN WALL JET REGION

RUN NO.	x feet	$\frac{u_{m1}}{U_o}$	b feet	$\frac{x}{2b_o}$	$\frac{x}{H}$	$\frac{u_{m1}}{U_o} \sqrt{\frac{H}{2b_o}}$	$\frac{u_*}{u_{m1}}$
2	.304	.283	-	41.5	.626	2.30	.0638
	.354	.265	.0560	48.3	.730	2.16	.0634
	.454	.233	.0665	61.8	.936	1.90	.0617
	.654	.184	.0710	89.1	1.349	1.50	.0640
	.804	.159	.0750	110	1.66	1.29	.0632
	.954	.136	.0766	130	1.97	1.11	.0630
	1.154	.115	.0867	157	2.38	.94	.0665
	1.400	.0945	.0930	191	2.88	.77	.0648
	1.600	.0865	.1160	218	3.30	.70	.0680
3	.276	.289	-	37.8	.569	2.35	.0627
	.306	.273	-	41.7	.630	2.22	.0652
	.346	.265	.0450	47.2	.714	2.16	.0640
	.386	.246	.0496	52.7	.795	2.00	.0640
	.436	.233	.0525	59.5	.900	1.90	.0644
	.486	.222	.0555	66.3	1.001	1.81	.0637
	.556	.205	.0577	75.8	1.150	1.67	.0640
	.606	.186	.0625	82.6	1.25	1.51	.0660
	.706	.163	.0640	96.4	1.46	1.33	.0694
	.806	.156	.0700	110	1.66	1.27	.0648
	.906	.138	.0720	124	1.87	1.12	.0680
	1.006	.121	.0775	137	2.07	.98	.0667
4	.255	.324	.0475	34.8	.797	2.24	.0596
	.555	.234	.0790	75.7	1.735	1.55	.0570
	.955	.167	.0950	130	2.98	1.10	.0572
	1.205	.130	.100	164	3.76	.86	.0632
	1.455	.114	.110	198	4.55	.75	.0610
	1.755	.100	.130	239	5.49	.66	.0580
	1.993	.0875	.137	272	6.23	.58	-
5	.215	.337	-	29.3	.672	2.23	.0639
	.255	.326	.052	34.8	.797	2.15	.0630
	.355	.287	.062	48.5	1.11	1.90	.0611
	.455	.254	.070	62.0	1.42	1.68	.0611
	.605	.217	.078	82.5	1.89	1.43	.0600
	.755	.188	.087	103	2.36	1.24	.0600
	.955	.1565	.095	130	2.98	1.03	.0610
	1.155	.129	.098	158	3.61	.85	.0664
	1.500	.107	.115	205	4.70	.71	.0638
	1.800	.091	.127	245	5.62	.60	.0680
	2.100	.074	.137	286	6.57	.49	-

















**B30010**